

THEORY OF PHASE TRANSITIONS IN DISORDERED CRYSTAL SOLIDS

A Dissertation
Presented to
The Academic Faculty

by

Huaming Li

In Partial Fulfillment
of the Requirements for the Degree
Doctor of Philosophy in the
School of Physics

School of Physics
Georgia Institute of Technology
August 2009

THEORY OF PHASE TRANSITIONS IN DISORDERED CRYSTAL SOLIDS

Approved by:

Dr. Mo Li, Advisor
School of Materials Science and
Engineering
Georgia Institute of Technology

Dr. Phillip First
School of Physics
Georgia Institute of Technology

Dr. Meiyin Chou
School of Physics
Georgia Institute of Technology

Dr. Andrew Zangwill
School of Physics
Georgia Institute of Technology

Dr. Toan Nguyen
School of Physics
Georgia Institute of Technology

Date Approved: June 26, 2009

To My Parents

ACKNOWLEDGEMENTS

I would like to take this opportunity to express my gratitude to many people. First of all, I want to thank my advisor Dr. Mo Li, who introduce me into this field, for his guidance and encouragement over the years. I also want to thank my committee members Dr. Andrew Zangwill, Dr. Phillip First, Dr. Toan Nguyen and Dr. Meiyin Chou for reading my thesis and providing constructive criticism. Special thanks go to current and former members of Dr. Mo Li's research group, Dr. Xianming Bai, Mr. Hao Wang, Mr. Ken Beyerlein, Mr. Yuzheng Guo, Mr. Tao Xu, Mr. Xueqiang Wang and Miss. Jie Feng. I would like to thank my family. My parents have always given their love and moral support whatever I did.

TABLE OF CONTENTS

ACKNOWLEDGEMENTS	iv
LIST OF TABLES	viii
LIST OF FIGURES	ix
SUMMARY	xviii
CHAPTER I INTRODUCTION.....	1
1.1 Background.....	1
1.2 Current Progress on Solid-state Amorphization	1
1.2.1 Experimental Investigation on Amorphization	1
1.2.2 Theoretical Studies on Solid-state Amorphization	2
1.3 Motivations and Contributions	3
1.4 Organization.....	8
CHAPTER II A PHENOMENOLOGICAL THEORY FOR POLYMORPHIC MELTING IN MACROSCOPIC BINARY SOLID SOLUTIONS	12
2.1 Lindemann's Criterion and Phase Transition Theory for Melting.....	12
2.2 Model and Theoretical Predictions for Polymorphic Melting	17
2.2.1 Construction of Model and Rescale	17
2.2.2 Static Equilibrium Condition	21
2.2.3 Landau Free Energy with Two External Variables.....	21
2.2.4 Endothermic Melting	22
2.2.5 Exothermic Melting---Reentrant melting	33
2.3 Summary: Endothermic Melting and Exothermic Melting	42
CHAPTER III FLUCTUATIONS AND NUCLEATION IN INHOMOGENEOUS BINARY SOLID SOLUTIONS	44

3.1 Amorphous Structure and Phase Transitions in One Dimension.....	44
3.2 Homophase Fluctuations and Heterophase Fluctuations.....	50
3.3 Energy Localization in Defective Crystals: Nonlinearity and Disorder.....	52
3.4 Classical and Modern Nucleation Theory.....	60
3.5 Landau-Ginzburg Free Energy: Stationary Solution in One Dimension.....	64
3.5.1 Rescale	65
3.5.2 Uniform Solutions and Linear Stability Analysis.....	66
3.5.3 Non-uniform Solution and Stability Analysis.....	68
3.6 Homogeneous Nucleation in One Dimension: Numerical Results.....	77
3.7 Homogeneous Nucleation in Two Dimension: Numerical Results	87
3.8 Heterogeneous Nucleation: Application to Nanosolids.....	93
3.8.1 Model	97
3.8.2 Numerical Results: Order Parameter Profiles and Phase Diagrams	101
3.8.3 Numerical Results: Comparison with Experiments.....	105
3.8.4 Discussion	110
3.9 Summary	111
CHAPTER IV MULTI-COMPONENT ORDER PARAMETERS AND MODELS IN TWO DIMENSIONS AND THREE DIMENSIONS	115
4.1 Phase Transitions in Solid Solutions.....	115
4.2 Structural Phase Transition: Cubic to Tetragonal phase.....	116
4.3 Orientational Order Broken and Domain Walls	120
4.3.1 Correlation Functions.....	121
4.3.2 Orientational Order and Amorphization in Nanocrystals	122
4.4 Summary	126

CHAPTER V CONCLUSION AND FUTURE WORKS	128
APPENDIX A	130
APPENDIX B	132
REFERENCES	133

LIST OF TABLES

Table 1	Parameter values for endothermic melting	25
Table 2	Parameter values for exothermic melting	35
Table 3	Eigenvalues for $a=0.150$	74

LIST OF FIGURES

Figure 1.1	Phase diagram of spin glass [21] and polymorphic melting phase diagram for a binary solid solution [10].	4
Figure 1.2	Molecular dynamic simulation results for binary Lennard-Jones solid solutions: (a) static mean square displacement, (b) (c) tetragonal and trigonal shear modulus, and (d) Enthalpy as a function of composition [23].	9
Figure 1.3	Schematic views of various types of disorder in binary systems: (a) perfect crystal, (b) composition disorder in random alloy, (c) position disorder, and (d) topological disorder.	10
Figure 1.4	Examples of short-range order in binary solid solutions: (a) 'black' atoms are preferentially surrounded by 'white' atoms; (b) 'black' atoms are preferentially surrounded by other 'black' atoms [26].	11
Figure 2.1	Phase diagram for Landau free energy of Eq.(1) with $E>0$ (Example: $E=4$). Dot line is for $T=T_1$, dashed line for $T=T_m$, and the origin represents the tricritical point $T=T_{cr}$, the line $C<0$ is the second order transition line. The region between T_1 line and positive A axis represents the stable initial state; the region between T_1 line and positive C axis indicates the metastable state; the region between positive C axis and negative A axis represents the stable final state.	14
Figure 2.2	Phase changes indicated by free energy with increasing temperature: $T_2 > T_0 > T_m > T_1$. T_0 is the critical point. ($E=4$, $C=2$, and $A=0.333$ for neutral stability point T_1 (dash dot line), $A=0.250$ for transition point T_m (dot line), $A=0$ for critical point T_0 (solid line) and $A=-0.050$ for T_2 (dash line).	15
Figure 2.3	Susceptibility χ of Eq. (2.5) as a function of temperature with $A = a_0(T_0 - T)$ of Eq. (1) for a first-order phase transition ($E=4$, $C=2$, $a_0=2$, $T_0=1$).	17
Figure 2.4	(a) Coupling function $e(T, x)$ as a function of composition X at temperature $T=1.100$. (b) Coupling function with variation of temperature at fixed composition $X=0.500$. The other parameters are shown in Table 1.	25

Figure 2.5	Melting line for the chose parameters in Table 1. The region below the melting line represents the crystalline state. The arrow shows the triple point at $(\tilde{T}_c, \tilde{X}_c) = (0.900, 0.850)$	28
Figure 2.6	Free energy barrier (a) and chemical potential change (b) along the melting line (Figure 2.5) for the chosen parameters in Table1.	29
Figure 2.7	Entropy change (a) and Enthalpy change (b) along the melting line (Figure 2.5) for the chosen parameters in Table 1.	29
Figure 2.8	Mean square order parameter values change (a) and absolute value of shear strain change (b) along the melting line (Figure 2.5) for the chosen parameters in Table 1.	30
Figure 2.9	$d_s = 1 - \frac{T_m^d}{T_m^0}$ indicating the contribution from static disorder (a) and mean square static atomic displacement change (b) along the melting line (Figure 2.5) for the chosen parameters in Table 1.	30
Figure 2.10	$w = \exp(-\Delta S)$ that probability is defined as $p = (\exp(-\Delta S))^\lambda$ for heterophase fluctuations of liquid-like clusters and λ is some positive constant (parameters in Table 1).	31
Figure 2.11	Shear elastic constant as a function of composition at the triple point temperature $T=1.1$ for the chosen parameters in Table 1.	31
Figure 2.12	Melting line with triple point $(\tilde{T}_c, \tilde{X}_c) = (0.900, 0.850)$ for the chosen parameters in Table 2.	36
Figure 2.13	Free energy barrier (a) and chemical potential change (b) along the melting line(Figure 2.12) for the chosen parameters in Table 2.	36
Figure 2.14	Entropy change (a) and Enthalpy change (b) along the melting line(Figure 2.12) for the chosen parameters in Table 2.	37
Figure 2.15	Mean square order parameter values change (a) and absolute value of shear strain change (b) along the melting line (Figure 2.12) for the chosen parameters in Table 2.	37
Figure 2.16	$d_s = 1 - \frac{T_m^d}{T_m^0}$ indicating the contribution from static disorder (a) and mean square static atomic displacement change (b) along the melting line (Figure 2.12) for the chosen parameters in Table 2.	38

Figure 2.17	$w = \exp(-\Delta S)$ that probability is defined as $p = (\exp(-\Delta S))^\lambda$ for heterophase fluctuations of liquid-like clusters and λ is some positive constant (parameters in Table 2)	38
Figure 2.18	Coupling function (a) and shear elastic constant (b) as a function of composition at the triple point temperature $T=0.509$ for the chosen parameters in Table 2.	39
Figure 3.1	(a) A high-resolution transmission electron microscopy image of a single amorphous boron nanowire [48, 49]; (b) A transmission electron microscopy image of amorphous Co-B chain [50].	45
Figure 3.2	(a) ordered chain model with the atomic position as $y_i=d_0+\varepsilon_i d_0$ and $\langle y_i \rangle = d_0$; (b) disordered chain model with the interatomic distance as $y_i - y_{i-1} = d_0 + \varepsilon_i d_0$ and $\langle y_i - y_{i-1} \rangle = d_0$	46
Figure 3.3	One-dimensional amorphous model by the Baker transformation with $u_{n+1} - u_n = v_n = A + Bx_n$. (a) the orbits of the Baker transformation and the corresponding atomic configurations; (b) amorphous-like pair correlation functions obtained using the Baker transformation; (c) amorphous-like pair correlation functions obtained using a nonlinear potential model.	46
Figure 3.4	First order phase transition in an Ising ferromagnet chain with discontinuous long-range order. Magnetization as a function of temperature is obtained by renormalization group methods (a) and by Monte Carlo calculation (b) [70].	47
Figure 3.5	Phase transitions in one-dimensional hard-core model with intermolecular potential for $\varepsilon_0 < 0$ (a) and the corresponding phase diagram (b) [94, 95].	49
Figure 3.6	Schematic illustrations of Heterogeneous Nucleation at surfaces.	51
Figure 3.7	Schematic illustrations of a nucleus of Homogeneous nucleation: (a) a nucleus with dark area; (b) distribution of order parameter value in real space; (c) distribution of order parameter value for sharp interface model (solid line) and diffuse interface model (dashed line).	51
Figure 3.8	Schematic views of (a) homophase fluctuation and (b) heterophase fluctuation for first order structural phase transitions in binary alloys [101].	51
Figure 3.9	Modulation instability for the quartic FPU model from [117]. For the last two picture (from top to bottom), $t=800$ and $t=8 \cdot 10^4$	55

Figure 3.10	(a) Sketch of two nucleotide chains with two types of base pairs A-T (Adenine-Thymine) and G-C (Guanine-Cytosine) and (b) DNA thermal denaturation [127].	56
Figure 3.11	(a) The distribution of average potential energy of soft host chain with an impurity characterized by stiffness α_i at three different temperatures. (b) The ratio of the average potential energy of an impurity site to that of a host particle as a function of temperature and stiffness [130].	57
Figure 3.12	(a) Fusion of two solitons at an impurity site ($n=0$) in a hard lattice with the nonlinear spring parameter ratio $b/b_0=10$. (b) The maximum potential energy $V_{\max}(r_0)$ as a function of b/b_0 [133].	59
Figure 3.13	Possible pressure-temperature phase diagrams for two-dimensional model described by an attractive potential with a repulsive core. Solid, liquid, gas and hexatic phases are shown, together with double lines of first-order transitions and single lines of second-order transitions [134].	60
Figure 3.14	The surface (long dash line) and bulk (dot line) contributions and the total excess free energy ΔF (solid line) of a spherical nucleus depending on radius r (e.g. $\Delta F_d = -1.500$, $\gamma = 1.200$). The arrow line indicates the critical nuclei position.	62
Figure 3.15	(a) The growth rate of the uniform solution $\bar{\eta}_2$ for $a=0.150$; (b) The cut-off wave vector of the uniform solution $\bar{\eta}_2$	66
Figure 3.16	Evolution of small perturbation around the uniform solution $\bar{\eta}_1$ (a) in time-space coordinates and (b) space distribution of order parameter profiles with $t=0, 5, 7, 50$ for $L=156.232$, $\delta=0.005$, $a=0.150$.	67
Figure 3.17	Phase portrait for (a) $a=0.300$, (b) $a=0.250$ and (c) $a=0.150$, where X represents the order parameter and Y is the ‘velocity’.	70
Figure 3.18	(a) Two non-uniform solutions for $a=0.010$ (solid line) and $a=0.150$ (dot line); (b) free energy dependence on the space coordinate for the non-uniform solution with $a=0.150$.	71
Figure 3.19	(a) Supersaturation as a function of parameter a ; (b) The maximum value of the non-uniform solution of Eq. (3.23) as a function of parameter a ; (c) The domain width of the non-uniform solution of Eq. (3.19) as a function of parameter a .	73

Figure 3.20	Free energy of critical nucleus as a function of (a) the domain width and (b) the normalized quadratic coefficient a ; (c) Ratio F/a over coefficient a	74
Figure 3.21	Eigenfunctions for the eigenvalues (a) $\lambda=-0.584$, (b) $\lambda=0$, and (c) $\lambda=0.299$ with $a=0.150$	75
Figure 3.22	(a) Potential Function for $a=0.050, 0.10, 0.150, 0.175, 0.200$; (b) Spectrum of Eq. (3.26): the shaded area is the corresponding continuous spectrum and the dot line, dash dot line and solid line represent the discrete spectrum.	76
Figure 3.23	Growth of a new phase region with $a=0.150, L=159.234$: (a) evolution of order parameter values with time and space coordinates; (b) spatial distribution of order parameter profiles for different time; (c) free energy density as a function of time.	79
Figure 3.24	Decay of the system with the small perturbation: $L=49.405, \Delta=-0.005$: (a) evolution of order parameter values with time and space coordinates; (b) spatial distribution of order parameter for different time; (c) free energy density as a function of time; (d) maximum order parameter values as a function of time.	81
Figure 3.25	Small perturbation from the Goldstone mode with $L=89.443, \Delta=0.005, a=0.150$: (a) evolution of order parameter values with time and space coordinates; (b) spatial distribution of order parameter profiles for different time.	82
Figure 3.26	Growth of the system with the small perturbation: $L=49.405, \Delta=-0.005$: (a) order parameter profiles as a function time and space coordinates; (b) spatial distribution of order parameter for different time $t=0, 5, 6, 8, 12$; (c) order parameter values for $t=0, 7, 12, 27, 42, 100$; (d) overlapping solutions (propagation front) for $t=12$ (red square solid line) and $t=27$ (black circle line) which is shifted to the space at $t=12$	83
Figure 3.27	(a) Maximum order parameter value and (b) free energy density as a function of time ($a=0.150, L=49.405, \Delta=-0.005$).	84
Figure 3.28	Domain width (a) and linear dimension (b) as a function of time. Red lines are fitting curves ($a=0.150, L=49.405, \Delta=-0.005$).	85

Figure 3.29	Collision of two identical nuclei with separation distance $L_s=40$, $a=0.150$, $\Delta=-0.005$, and $L=565.690$: (a) space-time evolution of order parameter values; (b) space distribution of order parameter profiles at different time values; (c) free energy density and (c) linear dimension as a function of time.	86
Figure 3.30	Spatial dependence of order parameter profiles for different time values (a) $t=0$, (b) $t=20$, (c) $t=27$, (d) $t=30$, (e) $t=50$ and (f) $t=160$ with $a=0.010$, $\delta=0.009$, $\chi=1$, $L=50$ in Eq. (3.40).....	89
Figure 3.31	(a) Contour plot for initial state at $t=0$ and (b) cross section along $x=24.610$ line for $t=30$ (black solid line) and $t=80$ (red dash line) with $a=0.010$, $\delta=0.009$, $\chi=1$, $L=50$ in Eq. (3.40).....	90
Figure 3.32	Spatial dependence of order parameter profiles for different time values (a) $t=0$, (b) $t=17$, (c) $t=19$ and (d) $t=50$ with $a=0.010$, $\delta=0.005$, $L=20$ in Eq. (3.41).....	91
Figure 3.33	(a) Contour plots for initial state at $t=0$ and (b) cross section along $x=9.840$ line for $t=30$ (solid line) and $t=100$ (dash line) with $a=0.010$, $\delta=0.005$, $L=20$ in Eq. (3.41).....	92
Figure 3.34	(a) front propagation showed by the moving location of $\eta(y)=\bar{\eta}/2$ for thermal fluctuations with $a=0.010$, $\delta=0.009$, $\chi=1$ in Eq. (3.40), along grid lines $x=24.610$ for $L=50$, $x=49.120$ (dot line) for $L=100$ (dash line) and $x=98.240$ for $L=200$ (solid line); (b) front propagation showed by the location of $\eta(y_s)=\eta(y-y_f)=\bar{\eta}/2$ where y_f is the final stable location for soliton-like fluctuations with $a=0.010$, $\delta=0.005$ in Eq. (3.41), along grid lines $x=9.840$ for $L=20$ (dash line), $x=19.680$ for $L=40$ (dot line) and $x=39.360$ for $L=80$ (solid line).....	92
Figure 3.35	Schematic representations of formation of disordered layers at grain boundaries (prewetting or premelting) ((a), (b))and a subsequent destabilization of grains that have two different models as shown in Figure 3.36 after reaching a critical grain size d (c).	96
Figure 3.36	Schematic view of two basic processes for melting and amorphization of nanosolids: (a) two-step model with surface-induced transition and first order transition and (b) homogeneous transition.....	96
Figure 3.37	Renormalized coefficients of quadratic term of free energy of Eq. (3.2) with parameters in Table 2 (a) At fixed temperature ($T=0.509$); (b) At fixed composition ($X=0.750$).	99

Figure 3.38	The coefficient to rescale the order parameter $q = \left(\frac{E}{ C(X) } \right)^{1/2}$ as a function of composition at fixed temperature $T=0.509$ with parameters in Table 2.	99
Figure 3.39	The coefficient to rescale the free energy $F_0 = \frac{ C(X) ^3}{E^2}$ as a function of X: (a) $X < 0.750$, (b) $X > 0.750$ at fixed temperature $T=0.509$ with parameters in Table 2.	100
Figure 3.40	Renormalized correlation function $\xi = \left(\frac{1}{a} \right)^{1/2}$: (a) at fixed temperature ($T=0.509$); (b) at fixed composition ($X=0.750$) at fixed temperature $T=0.509$ with parameters in Table 2.	100
Figure 3.41	Renormalized correlation function $\xi = \left(\frac{1}{a} \right)^{1/2}$: (a) at fixed temperature ($T=1.100$); (b) at fixed composition ($X=0.772$) with parameters in Table 1.	101
Figure 3.42	The transition points with the reciprocal rescaled thickness for several different δ values.	102
Figure 3.43	The renormalized nonzero order parameter solutions for different rescaled thickness at $\delta/\xi=-5$ (a) and $\delta/\xi=5$ (b).	103
Figure 3.44	The mean order parameter as a function of transition parameters for $L=20$ (dash line) and $L=10$ (solid line) with $\delta/\xi=-1$	103
Figure 3.45	(a) The average order parameters as a function of transition parameter for $L=15$ with $\delta/\xi=-0.100$. (b) The order parameter profiles as a function of space coordinates at the surface transition point for $L=15$ with $\delta/\xi=-0.100$	104
Figure 3.46	(a) The transition points with the reciprocal rescaled thickness for $\delta=-0.100$ (solid line) and $\delta=-0.200$ (dash line). Two arrow lines show the cut-off reciprocal thickness: $L=10$ for $\delta=-0.100$ (solid line) and $L=9.750$ for $\delta=-0.200$ (dash line). (b) The average order parameters as a function of transition parameter for $L=10$ (solid line) and $L=8$ (dot line) with $\delta/\xi=-0.100$. The arrow line shows the second transition point $a \approx 0.390$	104

Figure 3.47	The size-dependence of the melting temperature enhancement of In nanosolids in the Al matrix (triangles from [170]) and depression of In nanosolids supported by the amorphous C substrate (squares from [171] and circles from [172]). The red solid lines are the corresponding linear fitting lines that across the limit bulk melting point.....	107
Figure 3.48	(a) The size-dependence of the melting temperature as a function the reciprocal rescaled thickness for different δ/ξ values. (b) The size-dependence of the average order parameters as a function the reciprocal rescaled thickness for different δ/ξ values.	107
Figure 3.49	The size-dependence of the melting temperature as a function the reciprocal rescaled thickness for $\delta/\xi=-0.100$	108
Figure 3.50	(a) $T=1.100$, $X_b=0.772$. The melting points as a function of the reciprocal rescaled thickness for a binary alloy nanosolids with different δ/ξ values (parameters in Table 1). (b) $T=0.509$, $X_b=0.750$. The amorphization points as a function of the reciprocal rescaled thickness for a binary alloy nanosolid with different δ/ξ values (parameters in Table 2).....	108
Figure 3.51	(a) Simulated phase diagrams for bulk Pd-Cu alloys and Pd-Cu alloy nanoclusters with the diameter 2.260nm [192]. (b) The experimental binary phase diagram for Bi-Pb nanoparticles with the diameter $D=10\text{nm}$. The dashed lines are from the bulk phase diagram. The triangles are the experimental data for the surface transition lines and the circles for the second transition lines [185].	112
Figure 3.52	(a) Phase diagram for a binary alloy nanosolid with $L=1$ for $\delta/\xi=-1$ (dash dot line), -5 (dot line), -10 (dash line). The blue solid line is the bulk melting line. (b) Phase diagram for low temperature melting for a binary alloy nanosolid with $L=1$ for $\delta/\xi=-1$ (dash dot line), -5 (dot line), -10 (dash line). The temperature is renormalized by the temperature value at the triple point $T_{bt}=0.900$ (see parameters in Table 1).....	112
Figure 3.53	(a) Phase diagram for a binary alloy nanosolid with $L=3$ for $\delta/\xi=-1$ (dash dot line), -5 (dot line), -10 (dash line). The blue solid line is the bulk melting line. (b) Phase diagram for low temperature melting for a binary alloy nanosolid with $L=3$ for $\delta/\xi=-1$ (dash dot line), -5 (dot line), -10 (dash line). The temperature is renormalized by the temperature value at the triple point $T_{bt}=0.900$ (see parameters in Table 1).....	113

Figure 3.54	(a) Phase diagram for a binary alloy nanosolid with $L=4$ for $\delta/\xi=0.500$ (dash dot line), 1 (dot line), 5 (dash line). The blue solid line is the bulk melting line. (b) Phase diagram for low temperature melting for a binary alloy nanosolid with $L=4$ for $\delta/\xi=0.500$ (dash dot line), 1 (dot line), 5 (dash line). The temperature is renormalized by the temperature value at the triple point $T_{bt}=0.900$ (see parameters in Table 1).	113
Figure 3.55	Phase diagram for a binary alloy nanosolid with $L=10$ for $\delta/\xi=0.500$ (dash dot line), 1 (dot line), 5 (dash line). The blue solid line is the bulk melting line (see parameters in Table 1).	114
Figure 3.56	(a) Phase diagram for a binary alloy nanosolid with $L=10$ for $\delta/\xi=-0.100$: surface transition line (dash dot line), and second transition line (dash line). The blue line is the bulk melting line. (b) Phase diagram at low temperature melting for a binary alloy nanosolid with $L=10$ for $\delta/\xi=-0.100$: surface transition line (dash dot line), and second transition line (dash line). The temperature is renormalized by the temperature value at the triple point $T_{bt}=0.900$ (see parameters in Table 1).	114
Figure 4.1	Configuration with different randomness in 2D from [195].	117
Figure 4.2	The atomic configurations of defects in the binary arrays [23].	118
Figure 4.3	Phase (i)----phase (ii) is the transformation from square to rectangle. Phase (i)---- phase (iii) is the transformation from square to parallelogram.	120
Figure 4.4	Correlation functions in Fourier space with (a) $a_1=0.050$, $d_1=0.050$, $d_2=0.070$, $e_1=0.020$, $e_2=0.010$, $O_2=0.010$, (b) $a_1=0.200$, $d_1=0.050$, $d_2=0.070$, $e_1=0.020$, $e_2=0.010$, $O_2=0.010$ and (c) $a_1=0.200$, $d_1=0.050$, $d_2=0.070$, $e_1=0.020$, $e_2=0.010$, $O_2=0.500$. The solid line is $\langle \Theta(\vec{k}) \Theta(-\vec{k}) \rangle$, the long dash line $\langle u_x(\vec{k}) u_x(-\vec{k}) \rangle$, and the space dot line is $\langle u_y(\vec{k}) u_y(-\vec{k}) \rangle$	123
Figure 4.5	Representation of orientation field at one location.	124
Figure 4.6	Disorder parameter correlation function (solid line) and orientation field correlation function (dot line) at (a) $\gamma=1$, $A=2$ and $\alpha=2$; (b) $\gamma=1$, $A=1$ and $\alpha=2$; (c) $\gamma=1$, $A=0.500$ and $\alpha=2$	127

SUMMARY

Solid-state amorphization of a crystalline solid to an amorphous phase is extensively studied as a first order phase transition at low temperature for almost thirty years. Many similarities between heat-induced melting and solid-state amorphization have been recognized and a generalized Lindemann melting criterion has been built by focusing on the total mean-square atomic displacement as a generic measure of crystalline disorder in metastable solid solutions. In this dissertation, we report the recent progress on phenomenological models employed for thermodynamic description of macroscopic systems and fluctuations and nucleation of mesoscopic inhomogeneous systems in binary solid solutions under polymorphic constraints with no long-range diffusion involved.

Based on our understanding on atomic picture of solid-state amorphization in binary solid solutions, we propose a Landau free energy to describe amorphization as the first order phase transition. The order parameter is defined which represents the loss of long-range translational order. The elastic strain field induced by composition disorder plays the important role through the bilinear coupling with the order parameter. Elastic softening and amorphization happen simultaneously. From the similarity between the melting and amorphization, we use the temperature and composition as two external variables and treat solid-state amorphization as low temperature melting under polymorphic constraints. For homogeneous system, the phase diagrams for endothermic melting and exothermic melting are built separately and the corresponding thermodynamic quantities are presented.

A microscopic homogeneous nucleation mechanism is proposed conceptually in binary solid solutions under polymorphic constraints. The formation of an amorphous

embryo is initiated from the composition modulation in the crystal state and a subsequent polymorphous nucleation within the as-formed heterophase fluctuation. This homogeneous nucleation path is thought to be associated with the nonlinear energy localization mechanism connected with the localized large-amplitude excitations of atoms, which are induced by nonlinear and disorder. A Landau-Ginzburg free energy is constructed to describe the critical nucleus and the growth of the new phase in one-dimensional systems. Analytical and numerical methods contribute to the understanding the fluctuations and nucleation processes.

Size-dependent melting and amorphization in nanosolids are investigated. Two models are proposed for nanocrystalline solid solutions to glass transformations. Based on the thin film model with finite thickness, we build one-dimensional Landau-Ginzburg approach, which includes surface contribution and size dependence, and numerical results do show similarity with experiments' results qualitatively.

CHAPTER I

INTRODUCTION

1.1 Background

Melting has been recognized as heating induced phenomena from solids to liquids for hundreds of years. The conventional crystal-to-liquid transition at high temperature has been extensively investigated. Amorphization is another transformation that produces a disordered final solid state from an initially crystalline state. As a solid material, amorphous phase with no structural long-range order and has liquid-like short-range ordered configurations of its atomic arrangements with vibrational motions about their average positions within certain observation period. In the literature, people recorded the formation of amorphous phases as the natural phenomena driven by irradiation since 1893 [1]. For over 60 years, vapor quenching and liquid quenching [2, 3] techniques have been used and investigated to produce amorphous metallic materials. The first noted solid-state-amorphization experiment was done on intermetallic compounds in 1962 [4]. For recent years, solid-state-amorphization has been an active research area because of the potential use in industry. Experimentally, solid-state-amorphization could be induced in an alloy system under mechanical, chemical, or irradiation condition.

1.2 Current Progress on Solid-state Amorphization

1.2.1 Experimental Investigation on Amorphization

In binary solid solution systems, it may cause the amorphous phase formation by tuning the concentration under polymorphous constraints. The negative enthalpy of mixing would provide the chemical driving force for the transformation. Once beyond a certain concentration, the crystal is driven to the amorphous state with the increasing static disorder [5, 6, 8]. Below that limit, ‘pretransformation’ effects were investigated, such as elastic softening and increasing average atomic root-mean-square displacement [7]. A reentrant melting behavior was observed in Zr-Al solid solutions under mechanical alloying. Mean square total atomic displacement could be the indication of amorphization with the increasing composition in binary systems [7]. For a binary system with positive heat of formation, the stored elastic energy and interface energy is proposed to induce the driving force necessary for the amorphization [9].

1.2.2 Theoretical Studies on Solid-state Amorphization

Both melting and amorphization are the topological order-to-disorder transition in two and three dimensions. The parallel between them has been recognized: nucleation-and-growth as first order phase transition or homogeneously due to a catastrophic instability [5, 11-14]. Heterogeneous nucleation occurs at extrinsic defects such as grain boundaries, free surfaces, voids or dislocations. Homogenous transformation could be induced by electron irradiation, hydrogenation, and compression. The evidence comes from the softening of shear elastic constants in the absence of nucleation centers. One of the mechanical instability is Born’s criterion: loss of shear rigidity. The lattice stability condition for cubic crystals is

$$C_{11} + 2C_{12} > 0, \quad C_{11} - C_{12} > 0, \quad C_{44} > 0,$$

where C_{11} , C_{12} and C_{44} are Voigt's notation for elastic constants. Beside the mechanical catastrophe, several other lattice instability criteria are proposed: vibrational, entropical, or defect-induced catastrophe. Recent simulation results show that local instability could be induced simultaneously by Lindemann's criterion and Born's model [15]. However, as one-phase theory, both models couldn't predict the discontinuous change of first order transition [16]. Local inhomogeneity of defects at some surface could initiate a disordered nucleus. Based on the simulation results and experiments, defect-mediated melting successfully account for the discontinuous character. Egami and Easeda [17] proposed a topological criterion for amorphization that the critical elastic strain could be caused by the atomic-size mismatch in binary metallic systems.

Okamoto et al. [18] developed a unified thermodynamic approach on melting and amorphization. They generalized the Lindemann's criterion in disordered crystals and characterized the disordered processes by the static and the dynamic mean-square atomic displacements from the equilibrium lattice positions, which are the generic measures of topological and thermal disorder, respectively.

1.3 Motivations and Contributions

Based on the space distribution of particles in solids, there are three types of matter: periodic, quasi-periodic, and amorphous or glassy states, which are metastable with finite lifetimes. In real materials, disorder induced by defects will bring up complex structures, but the crystal lattice may still exist. The influence of disorder on the phase transition from the ordered state to the glassy state has received lots of attention [19]. The elastic degree of freedom plays an important role at phase transitions in solids [20]. Both the

spin glass state and the orientational glass state, which depend on the concentrations, have been observed in experiments and predicted in theory from solid solutions [21]. The strain field related to the frozen-in defects plays a role by coupling to the spin degree of freedom or orientational degree of freedom [21, 22]. As one type of structural glasses, metallic glass state from solid solutions has also been extensively studied recently under polymorphous constraints, i.e. no composition change related by long-range diffusion at low temperature (Figure 1.1).

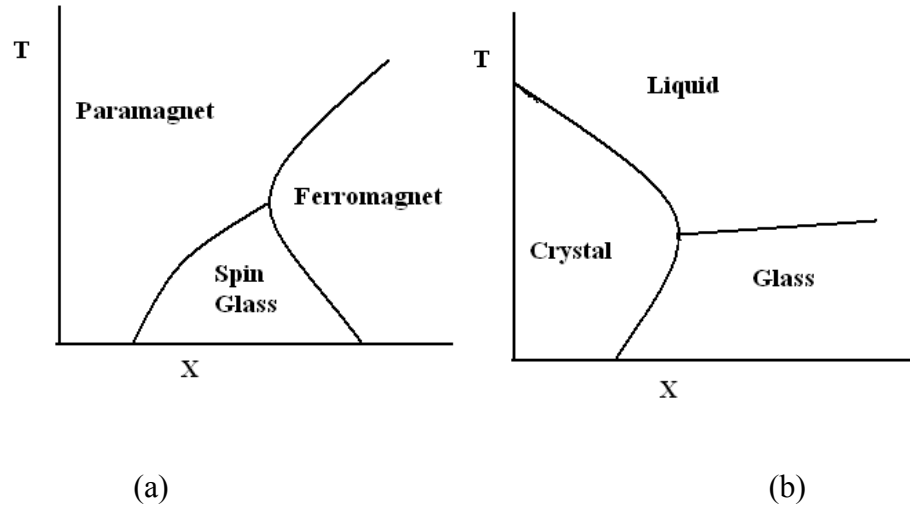


Figure 1.1 Phase diagram of spin glass [21] and polymorphic melting phase diagram for a binary solid solution [10].

There are many types of disorder in binary solid solutions that contribute to the destabilization of the initial crystalline state by increasing the free energy in one way or another [7, 11]. Molecular dynamics simulation has been used to explore the microscopic mechanisms of solid-state amorphization for a binary solid solution with varying concentration of solute atoms or crystal lattice defects under polymorphous constraints [23] (Figure 1.2). The level of disorder could be tuned by the concentration of solute atoms. At a given low temperature, the increasing static disorder, accompanied by Lattice

softening and increased anharmonicity of lattice vibrations, will raise the free energy of the parent crystal state. Lattice softening and increased anharmonicity will give rise to additional dynamic disorder. Elastic instability of the metastable crystalline phases is related to the internal strain fields induced by the mismatch of atomic sizes and the frozen defects provided by the rearrangement of the atoms in the lattice primarily through local shear displacement. Because of the low temperature, homogeneous impurity distributions are possible and the rearrangement only happens locally. The elastic shear instability and amorphous phase are simultaneously reached at some critical composition. For binary solid solutions, we will focus on the system with polymorphous constraints and topological disorder is induced by the interaction between position disorder and composition disorder with atomic size difference. For a thermodynamic description of the amorphous phase as a metastable state, the internal relaxation time is supposed to be shorter than the observation time, but still long enough for an ergodic sampling [24] in the binary systems. The time scale for amorphization from the initial crystal state is shorter than the evolution time for the stable crystal state, which is competing with the amorphous phase [11].

The Landau theory has been used to study melting as first order phase transition [25], and the multi-component order parameters are related to the Fourier components of the atomic density with nonzero reciprocal lattice vectors, which vanish in the liquid state. In our work, the disordering processes for amorphization by composition-induced destabilization are described in terms of a disorder parameter and internal strain fields besides temperature and composition, which means topological disorder is induced by the position disorder and chemical disorder with atomic size mismatch subject to

polymorphous constraints (Figure 1.3, Figure 1.4). Below the thermodynamic melting temperature of the initial perfect crystal, a solid solution could undergo a disorder-induced melting process at any temperature with sufficient alloy elements for endothermic processes. In the phenomenological approach, we apply continuum thermodynamic quantities to describe the transition for macroscopic systems. For the binary system at constant pressure, a phase diagram for melting transitions under polymorphous constraints could be determined by the temperature and composition. Exothermic melting phase diagram at low temperature are also obtained and the physical origin is discussed.

For macroscopic objects, Landau theory could be used to study the bulk properties for the first order phase transition processes. But, the order parameter usually shows smooth behavior from initial equilibrium state value to final equilibrium value for real materials, which is explained by the fluctuations of order parameter. In real systems with first order phase transition phenomena, there are two types of fluctuations, i.e. homophase fluctuations with small amplitude and heterophase fluctuations with large amplitude. Homophase fluctuations are associated with linear elementary excitations such as phonons in crystals. The microscopic mechanism for heterophase fluctuations is still unclear. For polymorphic melting in binary solid solutions, which is dominated by nonlinearity and disorder, we generalize the nonlinear energy localization mechanism as the microscopic origin of heterophase fluctuations. Two-step processes are involved, composition modulation and structure fluctuations. Large amplitude localized excitations could be initiated around several atoms through modulation instability, and the subsequent mesoscopic structural fluctuations may involve tens or hundreds of atoms

with superposition and fusion of localized excitations. For transient type of heterophase fluctuations, critical nuclei play the key role of nucleation and growth theory. The growth rate and dissolution of critical nuclei are studied in one dimension and several nuclei are obtained in a two-dimensional system by numerical methods through Landau-Ginzburg approach with our diffuse-interface model.

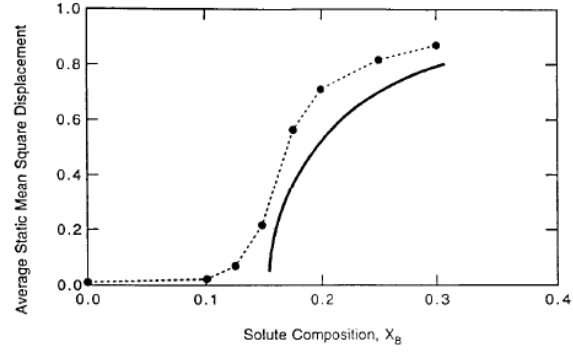
Besides the investigation on amorphization of bulk solid solutions, the understanding of nanocrystalline solid solutions to glass transitions driven by the grain boundary energy contributions is also of great importance to the application and synthesis of nanocrystalline materials. Experiments and theories show the existence of critical grain size that indicates the beginning of partial or complete amorphization. The question still remains that what happen for a grain after reaching the critical grain size. Surface effect and size dependence of melting phenomena have been extensively investigated in pure element nanosolids, and the alloys samples are also draw some attention. Amorphization on nanoscale has been studied for a while. Two possible transition paths are proposed to describe the amorphization processes in nanocrystalline solid solutions. Based on the thin film model, we include the surface contribution to the Landau free energy of the finite systems. Our numerical results show depression and superheating of melting points based on the different nature of surface influence. Melting points do have linear dependence on the size of the systems. Two types of melting processes are obtained, i.e. homogeneous melting and two-step melting which includes the initial surface transitions and the subsequent first-order transition. The numerical simulation does explain the experiments' results qualitatively.

1.4 Organization

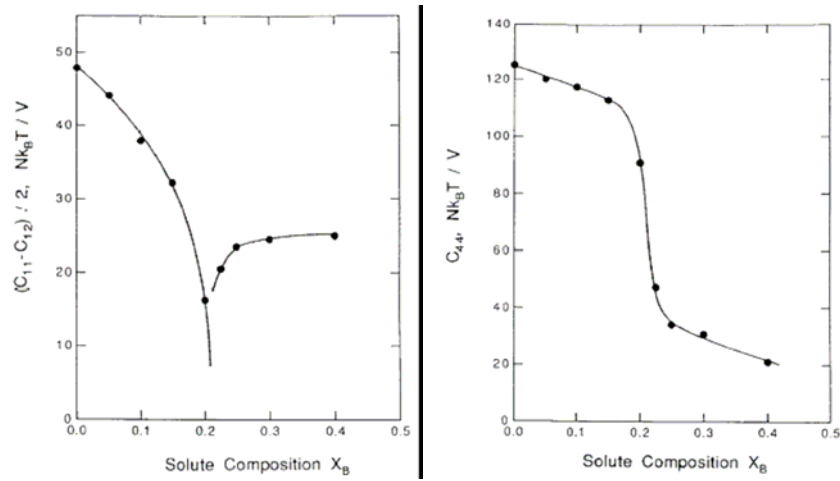
Some thermodynamic properties and the phase diagram of the model system of binary solid solutions are discussed in bulk systems in Chapter II. Based on the generalized Lindemann's criterion, we propose a general Landau free energy with a disorder parameter for melting in Section 2.1 and develop the Landau theory to describe the first order polymorphic melting in macroscopic binary alloy systems in Section 2.2.1. The mathematical form of our Landau free energy is presented in Section 2.2.3. Thermodynamic quantities and polymorphic phase diagrams are presented separately in Section 2.2.4 for endothermic melting and Section 2.2.5 for exothermic melting.

One-dimensional model is investigated in Chapter III. Several reviews are made on amorphous models and phase transitions in one dimension in Section 3.1, Nucleation and growth theory in Section 3.2, homophase fluctuations and heterophase fluctuations in Section 3.3, and energy localization in Section 3.4. Conceptually, we generalize the nonlinear energy localization mechanism as the microscopic origin of heterophase fluctuations for polymorphic melting in binary solid solutions in Section 3.4. Our analytical results on critical nuclei in one dimension are presented and the stability analysis is made in Section 3.5. Then we present our numerical results on homogeneous nucleation in one dimension in Section 3.6 and the nuclei in two dimensions are simply discussed in Section 3.7. In Section 3.8, we present numerical results from our thin film model and the prediction is discussed comparing to the experiments' results.

We simply mentioned the multi-component order parameters model in high dimension in Chapter IV. And the conclusion and future works are presented in Chapter V.

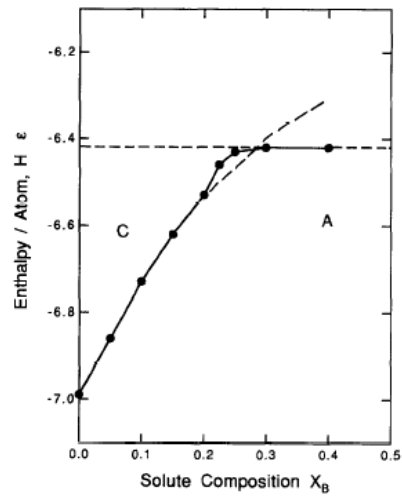


(a)



(b)

(c)



(d)

Figure 1.2 Molecular dynamic simulation results for binary Lennard-Jones solid solutions: (a) static mean square displacement, (b) (c) tetragonal and trigonal shear modulus, and (d) Enthalpy as a function of composition [23].

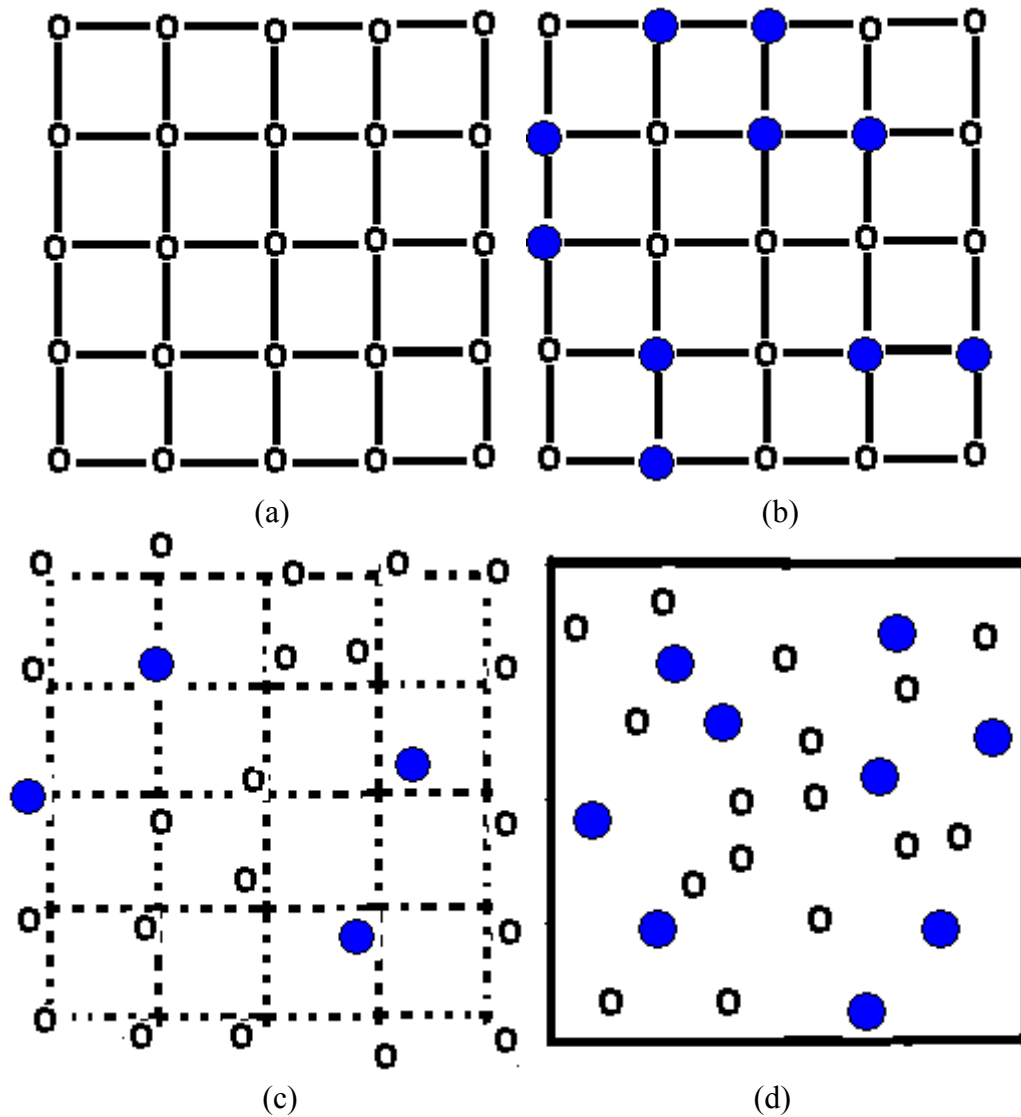
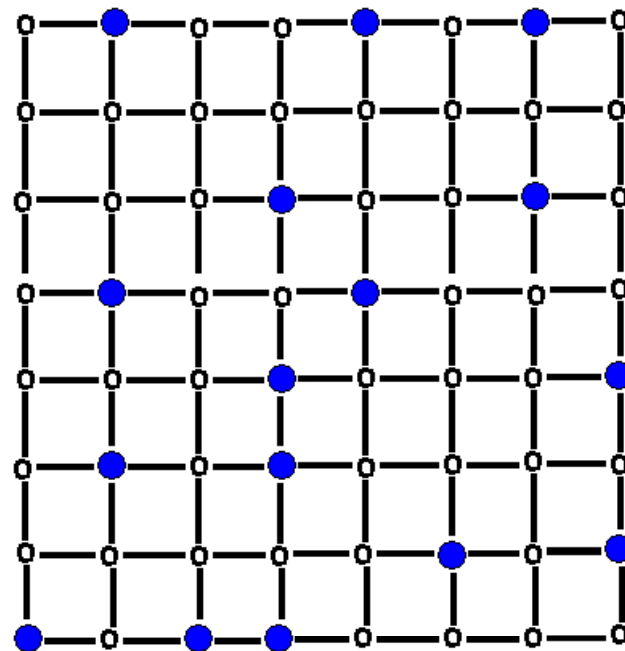
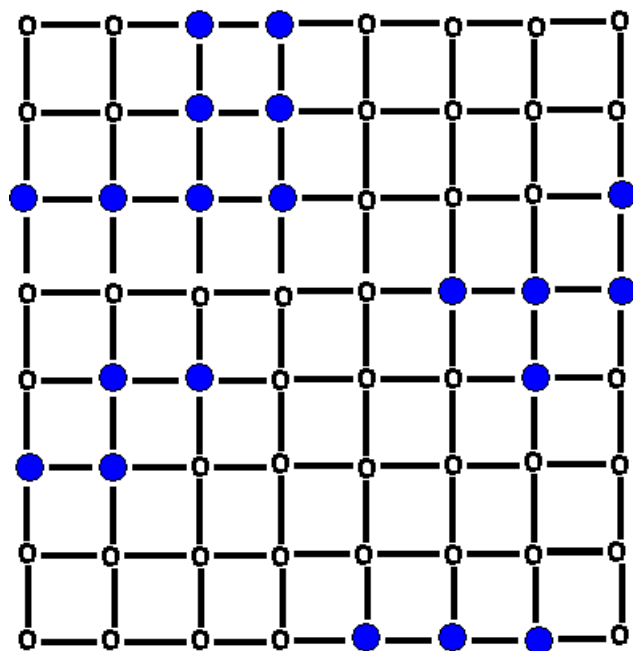


Figure 1.3 Schematic views of various types of disorder in binary systems: (a) perfect crystal, (b) composition disorder in random alloy, (c) position disorder, and (d) topological disorder.



(a)



(b)

Figure 1.4 Examples of short-range order in binary solid solutions: (a) ‘black’ atoms are preferentially surrounded by ‘white’ atoms; (b) ‘black’ atoms are preferentially surrounded by other ‘black’ atoms [26].

CHAPTER II

A PHENOMENOLOGICAL THEORY FOR POLYMORPHIC MELTING IN MACROSCOPIC BINARY SOLID SOLUTIONS

2.1 Lindemann's Criterion and Phase Transition Theory for Melting

Melting in crystals is an old topic for material scientist and physicist. To understand that phenomena, people proposed two different mechanisms: thermodynamic instability and mechanical instability such as Born's criterion [14]. In 1910, Lindemann proposed his thermodynamic criterion: melting happens when the vibration of atoms reaches some certain value with the increasing temperature. Mean square thermal displacement amplitude is used to characterize the thermal disorder: $\langle u^2 \rangle = c_0 a^2$. a is the nearest neighbor's distance, and c_0 is the Lindemann constant, which is around 10%. Generalized Lindemann's criterion is proposed to study heat-induced melting and disorder-induced amorphization in disordered crystals. The condition is $\langle u_{dyn}^2 \rangle + \langle u_{sta}^2 \rangle = \langle u_{cri}^2 \rangle$. $\langle u_{dyn}^2 \rangle$ is the mean square dynamic atomic displacement, and directly related to the temperature. $\langle u_{sta}^2 \rangle$ is the static component, and measure the static disorder induced by the defects. For a Debye crystal, we have:

$$\langle u_{dyn}^2 \rangle = \frac{9\hbar T}{mk\theta_0^2}.$$

(\hbar , Plank's constant; m , average atomic mass; k , Boltzmann constant; θ_0 , Debye temperature). As one phase theory, the above discussion is not related to the coexistence of the crystal and liquid state observed from experiments.

To study the transition from crystal to liquid phase as a first order phase transition, we will use a Landau free energy with a one-dimensional order parameter M , which characterize buildup of disorder and the loss of long-range order in melting process. A surface melting case for pure element crystals is studied by Lipowsky [25] and the disorder parameter could be defined as $M = 1 - \eta$, where η is the original normalized order parameter by bulk values and $\eta=0$ represents the order phase. For polymorphic melting in binary solid solutions, the primary order parameter M could be chosen as root mean square of total local atomic displacements. The Landau free energy is

$$F(M, T) = F_0(T) + AM^2 - CM^4 + EM^6, \quad (2.1)$$

which describes the discontinuous change of thermodynamic quantities of melting transition in pure crystal solids. We choose $A = a_0(T_0 - T)$ and $a_0 > 0$. The fundamental properties of Eq. (2.1) are discussed in the section (Figure 2.1, Figure 2.2) [10].

(1) Local equilibrium states

Condition for the minimum solutions of $F(M, T)$ is

$$\frac{\partial F}{\partial M} = 2AM - 4CM^3 + 6EM^5 = 0 \quad (2.2)$$

which have three set of solutions: (i) $M_1 = 0$; (ii) $M_2 = \pm \left(\frac{C - \sqrt{C^2 - 3EA}}{3E} \right)^{1/2}$; (iii)

$$M_3 = \pm \left(\frac{C + \sqrt{C^2 - 3EA}}{3E} \right)^{1/2}.$$

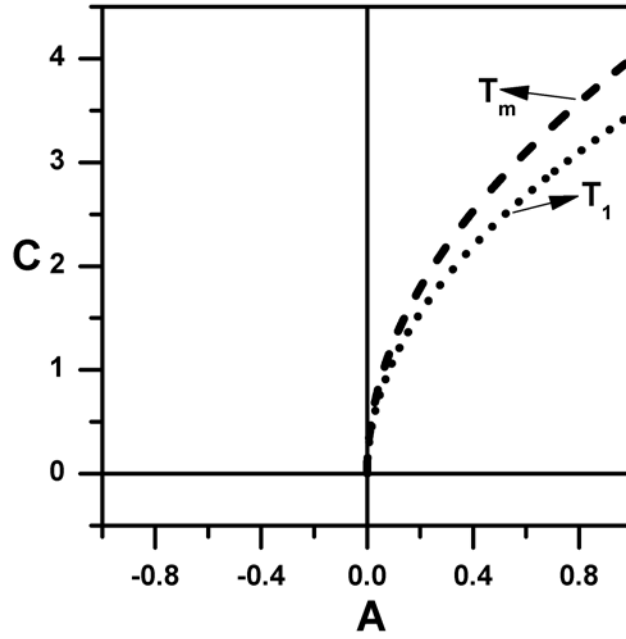


Figure 2.1 Phase diagram for Landau free energy of Eq.(1) with $E > 0$ (Example: $E=4$). Dot line is for $T=T_1$, dashed line for $T=T_m$, and the origin represents the tricritical point $T=T_{cr}$, the line $C < 0$ is the second order transition line. The region between T_1 line and positive A axis represents the stable initial state; the region between T_1 line and positive C axis indicates the metastable state; the region between positive C axis and negative A axis represents the stable final state.

(2) Stability condition of the equilibrium states

The stability of equilibrium states depends on the second derivative of Eq. (1):

$$\frac{\partial^2 F}{\partial M^2} = 2A - 12CM^2 + 30EM^4. \quad (2.3)$$

Solution (i) is stable for $A > 0$. Solution (ii) is stable for $C \cdot A < 0$ with $E > 0$. Solution (iii) is stable for $C \cdot A > 0$ with $E > 0$.

When $M_2 = M_3$, we have $A = \frac{C^2}{3E}$, which means the equilibrium state has neutral

$$\text{stability } \frac{\partial^2 F}{\partial M^2} = 0 \text{ at } T = T_1 = T_0 - \frac{C^2}{3a_0 E}.$$

(3) Melting temperature T_m

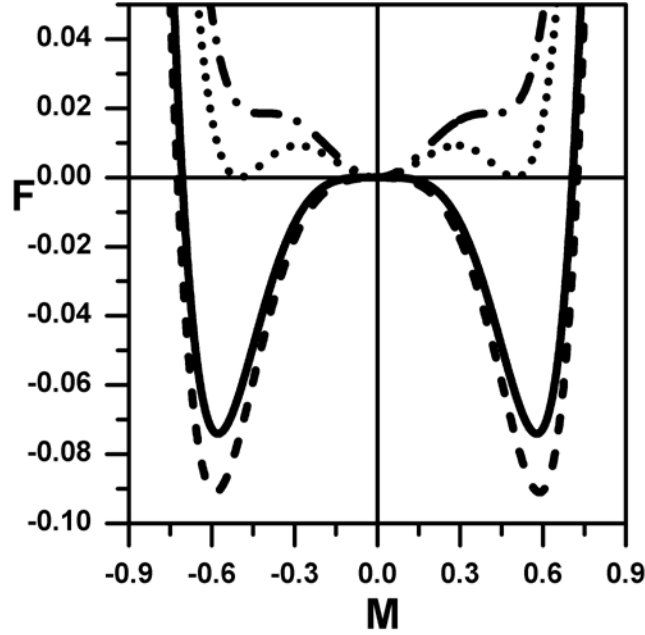


Figure 2.2 Phase changes indicated by free energy with increasing temperature: $T_2 > T_0 > T_m > T_1$. T_0 is the critical point. ($E=4$, $C=2$, and $A=0.333$ for neutral stability point T_1 (dash dot line), $A=0.250$ for transition point T_m (dot line), $A=0$ for critical point T_0 (solid line) and $A=-0.050$ for T_2 (dash line).

At the transition point, we have $F = 0$. Three solutions for $F = 0$ are: (i) $\tilde{M}_1 = 0$;

$$(ii) \tilde{M}_2 = \pm \left(\frac{C - \sqrt{C^2 - 4EA}}{2E} \right)^{1/2} ; (iii) \tilde{M}_3 = \pm \left(\frac{C + \sqrt{C^2 - 4EA}}{2E} \right)^{1/2} \text{ with } A = a_0(T_0 - T).$$

When the temperature reaches at $T = T_m$, we see $\tilde{M}_2 = \tilde{M}_3$. So the condition for the

melting is $A = \frac{C^2}{4E}$ and $T_m = T_0 - \frac{C^2}{4a_0E}$. The energy barrier for the phase jump is

$$\Delta F = \frac{8}{27} \frac{A^2}{C} = \frac{1}{54} \frac{C^3}{E^2}, \text{ which is fixed for constants } C \text{ and } E.$$

(4) Critical point T_0

The crystal phase will lose the stability when $A = 0$ at $T = T_0$.

(5) Tricritical point T_c

Supposing the coefficients A and C depending on two external variables: the temperature T and the composition X . The phase diagram, the tricritical point $T = T_{tc}$ at $A = C = 0$ connects the first order transition line $T = T_m$ and the second order transition line $T = T_{cs}$.

(6) Thermodynamic quantities

Entropy is defined as $S = -\left(\frac{\partial F}{\partial T}\right)_p$. At equilibrium state, we have

$$S = -\left(\frac{\partial F}{\partial T}\right)_p = -\frac{\partial F_0}{\partial T} - \frac{\partial A}{\partial T} M^2 \quad (2.4)$$

Specific heat capacity is $c_p = T\left(\frac{\partial S}{\partial T}\right)_p$ and:

$$T < T_0, \quad c_p = -T \frac{\partial^2 F_0}{\partial T^2},$$

$$T > T_0, \quad c_p = -T \frac{\partial^2 F_0}{\partial T^2} - T \left(\frac{\partial^2 A}{\partial T^2} M^2 + \frac{\partial A}{\partial T} \frac{\partial (M^2)}{\partial T} \right),$$

$$c_p = c_p^0 + \frac{a_0^2}{\sqrt{C^2 - 3EA}} \quad \text{for } A = a_0(T_0 - T).$$

Susceptibility associated to the order parameter is defined as

$$\chi = \lim_{\zeta \rightarrow 0} \left(\frac{\partial M}{\partial \zeta} \right)_{\bar{M}}$$

with ζ referring to the conjugated field. We have (Figure 2.3)

$$\chi = \begin{cases} \frac{1}{3} \frac{2A}{E} & T < T_0 \\ \frac{E}{8 \sqrt{C^2 - 3EA} (C + \sqrt{C^2 - 3EA})} & T > T_0 \end{cases} \quad (2.5)$$

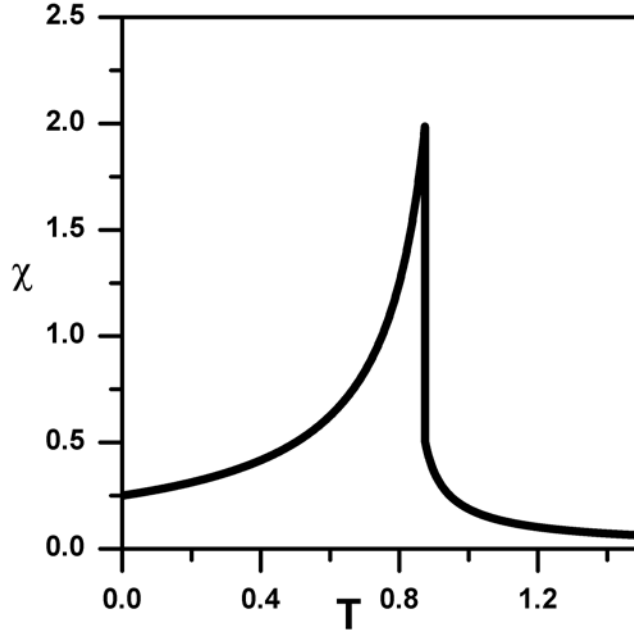


Figure 2.3 Susceptibility χ of Eq. (2.5) as a function of temperature with $A = a_0(T_0 - T)$ of Eq. (1) for a first-order phase transition ($E=4$, $C=2$, $a_0=2$, $T_0=1$).

2.2 Model and Theoretical Predictions for Polymorphic Melting

2.2.1 Construction of Model and Rescale

Similarities between melting and solid-state amorphization have been recognized [11-14]: Heterogeneous and homogeneous nucleation processes, loss of long-range order, elastic behavior, and volume change. We treat them as the unified topological disordering processes, melting at high temperature and amorphization at low temperature, respectively. Since the dynamics of glass and liquid are quite different, the amorphous phase could be considered as an undercooled liquid state that is a configuration-frozen in

state thermodynamically. In a two-component system, an equilibrium phase can be characterized by temperature, pressure and composition. The numbers of independent variables are chosen according to the Gibbs phase rule. At constant pressure, one degree of freedom can define the equilibrium state, and all other parameters are chosen to minimize the Gibbs free energy. Under the condition of ergodic sampling, thermodynamic functions can be discussed for metastable states, liquid and amorphous phase, which is a local stability of the system at a local minimum of Gibbs free energy with respect to atomic rearrangements. To apply equilibrium thermodynamics to discuss polymorphic melting, several kinetic constraints are needed. The time scale τ_2 for validity of polymorphous constraints is long enough to make the metastable crystalline phase accessible in laboratory characterized by the time scale τ_{obs} . The corresponding time window is

$$\tau_1 < \tau_{\text{obs}} < \tau_2,$$

where τ_1 is the internal time scale for the relaxation, and τ_2 could be around 10-100ps with the time scale for atomic motion about 0.100ps[11]. For liquids, τ_1 is short for all the relaxations, but the slow relaxation modes in amorphous phase could be specified by $\tau_{\text{slo}} > \tau_2$. Those slow modes could be blocked by the imposed auxiliary constraints with $\tau_{\text{fas}} \rightarrow \infty$ [27]. Also, the time scale $\tau_{1 \rightarrow a}$ for crystal-to-glass transformation is short compared with the time scale $\tau_{a \rightarrow 2}$ for possible competing glass-to-crystal transition [11]. After imposing appropriate constraints, both the liquid and amorphous phase behave ergodically whereas the amorphous phase is only allowed to access parts of phase spaces associated with a particular frozen-in state.

Based on the Lindemann's criterion on melting, the instability occurs once the local atomic dynamic displacement amplitude is large enough and exceeds some threshold value. Later on, the generalized criterion, which includes the static and dynamic atomic displacement amplitude, is used to describe the amorphization [7, 8, 18, 23, 28]. The atomic mean square displacement could be a measure of the stability of the crystal structure from elastic neutron diffraction scan and molecular dynamics simulation under polymorphous constraint. The static mean square displacement plays an equivalent role to the dynamic mean square displacement to measure the melting transition in solid solutions and the probability distribution of static displacements is not Gaussian [29]. For cubic materials, all the atoms have the same isotropic mean square displacement: $\langle u_x^2 \rangle = \langle u_y^2 \rangle = \langle u_z^2 \rangle$. As a part of configuration free energy, elastic energy depends on the atomic configuration of two atom species and individual atomic position in binary solid solutions.

We use one component order parameter and elastic degree of freedom to construct Landau free energy as following:

$$\tilde{f} = \tilde{f}_0 + \tilde{f}(\tilde{M}) + \tilde{f}(\tilde{\varepsilon}) + \tilde{f}_c(\tilde{M}, \tilde{\varepsilon}), \quad (2.6)$$

where \tilde{M} is the order parameter contributed by position disorder and represents the root mean square of the local atomic displacement field over the corresponding crystal state.

$\tilde{\varepsilon}$ is the shear strain induced by the composition disorder.

$\tilde{f}(\tilde{M}) = \tilde{A} \cdot \tilde{M}^2 - \tilde{C} \cdot \tilde{M}^4 + \tilde{E} \cdot \tilde{M}^6$ is the bulk free energy to describe the phase transition,

and $\tilde{f}(\tilde{\varepsilon}) = \frac{\tilde{\mu}_0}{2} \tilde{\varepsilon}^2$ is the part of the elastic energy contributed by shear strain. The choice

of $\tilde{f}(\tilde{M})$ by including only the even terms stems from the fact that only $\langle u^2 \rangle$ is

physically meaningful. $\tilde{\mu}_0$ is the bare shear elastic constant. $\tilde{f}_c(\tilde{M}, \tilde{\varepsilon}) = \tilde{e} \cdot \tilde{M} \cdot \tilde{\varepsilon}$ is the coupling term between the position disorder and shear strain and f_0 is independent of \tilde{M} and $\tilde{\varepsilon}$.

For solid solutions, the atomic size difference and composition disorder produce the strain field and the static displacement field. The stored elastic energy will raises the free energy of the crystal state, and also the long-range field interacts with the local atomic displacement field. Elastic stability's criterion on melting needs to soften the shear modulus. From the interaction, the transition happens when the shear modulus reaches the minimum.

For later convenient, we rescale the variables as $M = \frac{\tilde{F}_0^{1/6}}{\tilde{E}^{1/6}} \tilde{M}$, $\varepsilon = \frac{\tilde{F}_0^{1/2}}{\tilde{\mu}_0^{1/2}} \tilde{\varepsilon}$.

$$f(M) = A \cdot M^2 - C \cdot M^4 + E \cdot M^6 \quad (2.7a)$$

$$f(\varepsilon) = \frac{\mu_0}{2} \varepsilon^2 \quad (2.7b)$$

$$f_c(M, \varepsilon) = e \cdot M \cdot \varepsilon \quad (2.7c)$$

$$\text{with } A = \frac{\tilde{A}}{\tilde{F}_0^{2/3} \tilde{E}^{1/3}}, C = \frac{\tilde{C}}{\tilde{F}_0^{1/3} \tilde{E}^{2/3}}, E = 1, \mu_0 = 1, e = \frac{\tilde{e}}{\tilde{F}_0^{1/3} \tilde{E}^{1/6} \cdot \tilde{\mu}_0^{1/2}}.$$

Also, we could obtain the dimensionless form of the equation. Let $\tilde{M} = \left(\frac{\tilde{C}}{\tilde{E}} \right)^{1/2} \eta$,

$\tilde{F}_0 = \frac{\tilde{C}^3}{\tilde{E}^2}$. $\tilde{f}(\tilde{M})$ is transformed into the following form:

$$f(\eta) = \frac{\tilde{f}}{\tilde{F}_0} = a \cdot \eta^2 - \eta^4 + \eta^6 \quad (2.8)$$

2.2.2 Static Equilibrium Condition

Under static equilibrium condition (stress free), we have:

$$\frac{\partial f}{\partial \varepsilon} = e \cdot M + \mu_0 \cdot \varepsilon = 0, \quad (2.9)$$

and

$$\varepsilon = -\frac{e}{\mu_0} M. \quad (2.10)$$

Substituting Eq. (2.10) into Eq. (2.6), we obtain the effective free energy:

$$f_{\text{eff}} = \tilde{A} \cdot M^2 - C \cdot M^4 + E \cdot M^6 \quad (2.11)$$

$$\text{with } \tilde{A} = A - \frac{e^2}{2\mu_0}.$$

Expression for the effective elastic constant is:

$$\begin{aligned} \mu &= \frac{\partial^2 f}{\partial \varepsilon^2} - \frac{\partial^2 f}{\partial \varepsilon \partial M} \cdot \left(\frac{\partial^2 f}{\partial M^2} \right)^{-1} \cdot \frac{\partial^2 f}{\partial \varepsilon \partial M} \\ &= \mu_0 - e^2 \cdot \chi \end{aligned} \quad (2.12)$$

$$\text{with the order parameter susceptibility } \chi = \left(\frac{\partial^2 f}{\partial M^2} \right)^{-1}.$$

2.2.3 Landau Free Energy with Two External Variables

The First polymorphous melting phase diagram [5] was obtained by Fecht et al. (1989) by the generalized Clapeyron equation for a binary system. The equilibrium condition among crystal, liquid and amorphous phase is the same molar Gibbs free

energies, which depend on the temperature, pressure and composition. At constant pressure, a calculated example of Ni-Zr alloys is given and discussed. Also the metastable phase diagram could be derived by the CALPHAD method [30, 31] with temperature and composition, which is very popular for experimentalists. In the following sections, we will use Landau theory to obtain phase diagrams.

From Landau free energy of Eq. (2.11), we consider the coefficients have the following general forms:

$$\tilde{A} = \tilde{A}(T, X), \quad C = C(X) \quad E = \text{cons.} \quad (2.13)$$

with two external variables: T and X . We will determine the possible choice for function \tilde{A} . At fixed composition X , the free energy will have the same behavior with the increasing temperature as in Figure 2.2. At high temperature, we will focus on the endothermic behavior for melting. Based on the low temperature behavior (below the triple point), we will discuss two cases for solid-state amorphization: endothermic melting and exothermic melting. In the following discussions, low temperature melting is referred to the solid-state amorphization and high temperature melting corresponding to the traditional normal melting. They are separated by the triple point, which is indicated as zero entropy change and defined as the coexistence state of crystal phase, liquid phase and amorphous phase.

2.2.4 Endothermic Melting

For normal melting with absorbing heat, a solid solution can only has one melting point and melt polymorphically to either liquid at high temperature or undercooled liquid

state at low temperature. The expansion form for function $\tilde{A}(T, X)$ at some reference point $(\tilde{T}_0, \tilde{X}_0)$ is [32]:

$$\tilde{A}(T, X) = \tilde{A}_0(X) + \tilde{A}_1(X) \cdot (T - \tilde{T}_0) + \dots \quad (2.14)$$

Substituting Eq. (2.13) and Eq. (2.14) into Eq. (2.11), we find the solutions for neutral stability point T_1 , transition point T_m , and critical point T_0 :

$$T_1 = \tilde{T}_0 + \frac{C^2(X)}{3\tilde{A}_1(X)} - \frac{\tilde{A}_0(X)}{\tilde{A}_1(X)} \quad (2.15)$$

$$T_m = \tilde{T}_0 + \frac{C^2(X)}{4\tilde{A}_1(X)} - \frac{\tilde{A}_0(X)}{\tilde{A}_1(X)} \quad (2.16)$$

$$T_0 = \tilde{T}_0 - \frac{\tilde{A}_0(X)}{\tilde{A}_1(X)} \quad (2.17)$$

For endothermic melting transition, we need $T_1 < T_m$ which means that the transition could be caused by the increasing temperature at fixed composition. So we have $\tilde{A}_1(X) < 0$.

And $\tilde{A}_0(X) > 0$ if $T_0 > \tilde{T}_0$. Assuming the following function form:

$$\tilde{A}_0(X) = \tilde{A}_0 \cdot (\tilde{X}_0 - X) \quad \tilde{A}_0 = \text{const.} > 0 \quad (2.18)$$

$$\tilde{A}_1(X) < 0$$

Since the melting transition is first order, we could have the function form for $C(X)$:

$$C(X) = (C_0 + C_1(X - X_0))^2, \quad (2.19)$$

with $C_1 > 0$, $C_0 > 0$ to keep $C(X) > 0$.

For the coupling function $e = e(T, X)$ that indicates the interaction between the position disorder and composition disorder with atomic size effect, we choose the following simple form at low temperature

$$e(T, X) = \begin{cases} ((\alpha_0 - \alpha_1(T - T_0 + \Delta))X)^{1/2} & X \leq X_m \\ ((\beta_0 - \beta_1(T - T_0 + \Delta))(\tilde{X} - X))^{1/2} & X \geq X_m \end{cases}, \quad (2.20)$$

based on understanding of the measurement of Debye-Waller factor from the experiments' results [7, 8] with isotropic approximation, where X_m is the threshold value, \tilde{X} the corresponding value of pure solute crystal, and $\alpha_0, \alpha_1, \beta_0, \beta_1, \Delta$ are parameters. An example is shown in Figure 2.4(a) and the maximum point is the transition point at fixed low temperature. For high temperature melting, the coupling will disappear after reaching the threshold value. The total atomic mean square displacement clearly depends on the temperature and the composition in binary solid solution. The mean square total atomic displacement increases with increasing temperature at low composition values and decreases at high composition values [7, 8]. The mean square static displacement is increasing with increasing composition at constant temperature, varying with temperature at high constant composition and almost no change for low constant composition [7, 8], and linearly related to the mean-square chemical disorder [18, 28].

Assuming function A in Eq. (2.11) also has the form of Eq. (2.13):

$$A(T, X) = A_0(X_0 - X) + A_1(T - T_0). \quad (2.21)$$

Substituting Eq. (2.19)—(2.21) back into Eq. (2.11), we have the following equation

$$\begin{aligned} \tilde{A}(T, X) = & \left(A_0 + \frac{\alpha_0}{2\mu_0} \right) (\tilde{X}_c - X) + \left(A_1 + \frac{\alpha_1 X}{2\mu_0} \right) (T - \tilde{T}_c) \\ & + \left(A_0 \cdot \delta - \frac{\alpha_0}{2\mu_0} (X_0 - \delta) - A_1 \cdot \Delta \right) \end{aligned} \quad (2.22)$$

with $\tilde{X}_c = X_0 - \delta$, $\tilde{T}_c = T_0 - \Delta$, $\delta = \frac{C_0}{C_1}$. Comparing Eq. (2.22) with Eq. (2.17) and Eq.

(2.18), we could choose the parameter values to set up the following relations:

$$\tilde{X}_c = \tilde{X}_0, \tilde{T}_c = \tilde{T}_0, \tilde{A}_0 = A_0 + \frac{\alpha_0}{2\mu_0}, \tilde{A}_1(X) = A_1 + \frac{\alpha_1 X}{2\mu_0}, \quad (2.23)$$

$$A_0 \cdot \delta - \frac{\alpha_0}{2\mu_0}(X_0 - \delta) - A_1 \cdot \Delta = 0 \quad (2.24)$$

We can rewrite Eq. (2.19) and Eq. (2.22):

Table 1 Parameter values for endothermic melting

T_0	X_0	E	μ_0	Δ	A_0	A_1	C_0	C_1	α_0	α_1	β_0	β_1
1	1	1	1	0.100	2	-1	0.150	1	0.941	0.100	0.599	0.100

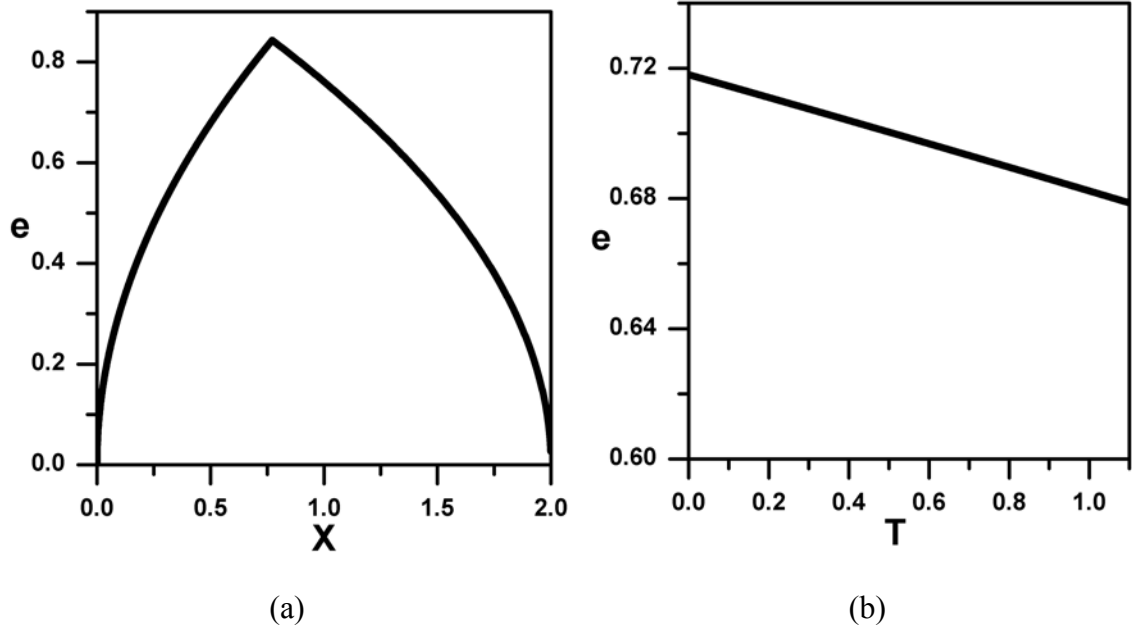


Figure 2.4 (a) Coupling function $e(T, x)$ as a function of composition X at temperature $T=1.100$. (b) Coupling function with variation of temperature at fixed composition $X=0.500$. The other parameters are shown in Table 1.

$$C(X) = (C_1(X - \tilde{X}_c))^2 \quad (2.25)$$

$$\tilde{A}(T, X) = \tilde{A}_0 \cdot (\tilde{X}_c - X) + \tilde{A}_1(X) \cdot (T - \tilde{T}_c) \quad (2.26)$$

where $(\tilde{T}_c, \tilde{X}_c)$ is the triple point.

For the pure crystal solids (solvent or solute), there will be no internal strain field induced by impurity atoms. For solid solutions at constant temperature (Figure 2.4), the coupling will increase with the composition and reach the maximum at the melting transition point. Comparing with the experiments [7, 8], the more solute atoms added in, the more disordered solids you could make for certain composition range. Beyond the critical composition value, it will decrease until the full solute crystal is reached. In a solid solution with certain components (Figure 2.4(b)), the static displacements could make more contribution to the disorder at low temperature. At high temperature, the thermal disorder from heating is the main cause to induce the melting transition from crystal phase to liquid phase.

The crystalline phase need climb a potential barrier into the disordered phase. The barrier is defined as

$$\Delta F = \frac{1}{54} \frac{C(X)^3}{E^2} \quad (2.27)$$

for the first order phase transition. And the critical order parameter square value is

$$M_c^2 = \frac{1}{2} \frac{C(X)}{E} \quad (2.28)$$

at the transition points. One reason for the choice of $C(X)$ without temperature dependence is trying to use simple calculus to obtain the phase diagram and takes into account of composition disorder by composition dependence. In Figure 2.6(a), for high

temperature melting, the free energy barrier decreases with the increasing composition from zero value and reach the zero at the triple point. When adding more solute atoms into the solid solvents, the crystal structure will become weaken with enhanced static disorder and the atoms could be deviated from their crystal lattice position and displaced from each other more easily. So the corresponding critical order parameter square values will decrease along the melting line (Figure 2.8(a)). And the transition temperature will decrease with the increasing composition (Figure 2.5). Once the system reaches the triple point, the energy barrier disappears, and the crystal phase, liquid phase and amorphous phase meet together. In Figure 2.8(b), the amplitude of shear strain change along the melting line has a peak with the composition variance. It indicates that the contribution of the static disorder for the melting increases before saturation. Because of the weakening of the crystal structure, the energy barrier decreases deep, and the critical order parameter value could be reached easily. Relatively, the less static disorder will make the crystal structure broken.

For low temperature melting, the disorder induced by composition and atomic size mismatch will dominate the process and dynamic disorder always is helpful to destabilize the system. Along the melting line, the slightly increasing energy barrier (Figure. 2.5(a)) and critical order parameter square value (Figure 2.8(a)) indicates the competition between disorder and nonlinearity by increasing impurity atoms, which could stabilize the crystal structure somehow. During the endothermic melting process, the crystal solids will absorb the heat and the entropy change will be positive (Figure 2.7(a)). The entropy contribution from the increasing disorder by alloy elements is responsible for the positive entropy change along the melting line even with typical short- range chemical disorder in

amorphous phase (Figure 2.7(a)). The triple point is the isentropic transition point: $\Delta S = \Delta F = 0$. Kinetics of first-order phase transitions, nucleation and growth mechanism, occurs as the result of heterophase fluctuations in a homogeneous system and describes the process from a metastable to a stable state. Around the melting point, the heterophase fluctuations are enhanced with the increasing composition [5, 32]. The probability, which is defined as $p = (\exp(-\Delta S))^\lambda$, for the evolution of small liquid-like clusters could reach one at the triple point (Figure 2.10). λ is some positive constant. The contribution for melting from static disorder is described in the generalized Lindemann's criterion, and the melting temperature is

$$T_m = \frac{mk\theta_d^2}{9\hbar^2} \langle u_{cri}^2 \rangle, \quad (2.29)$$

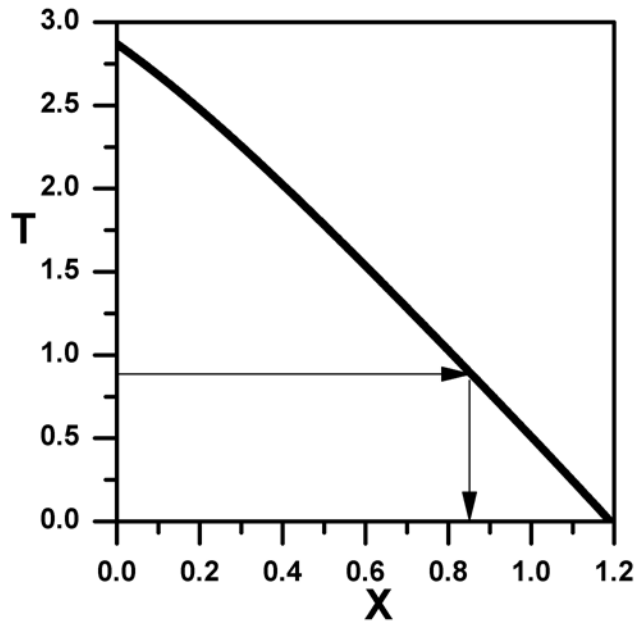
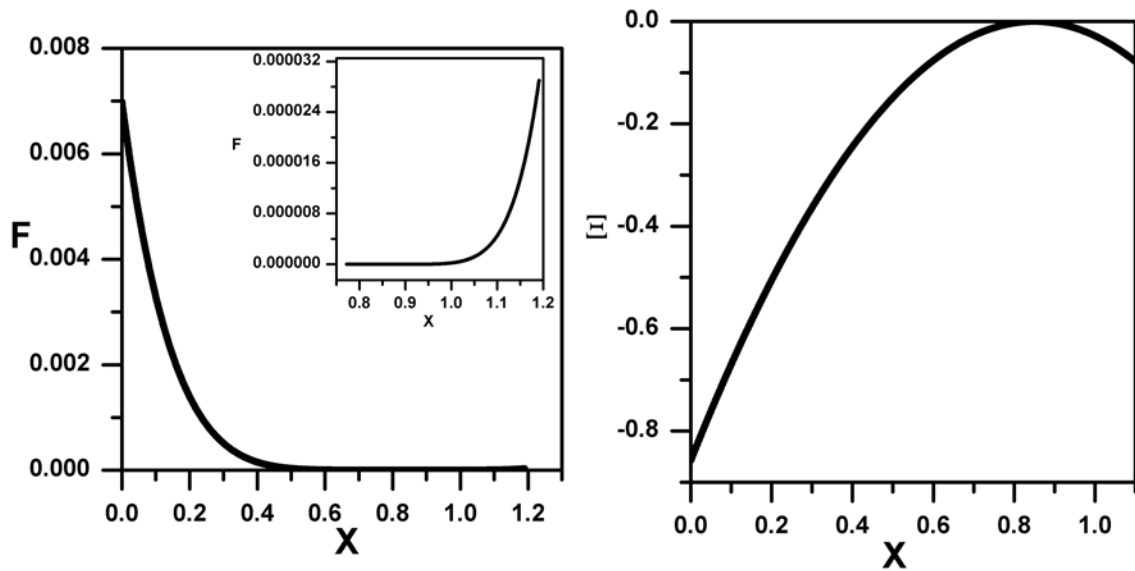


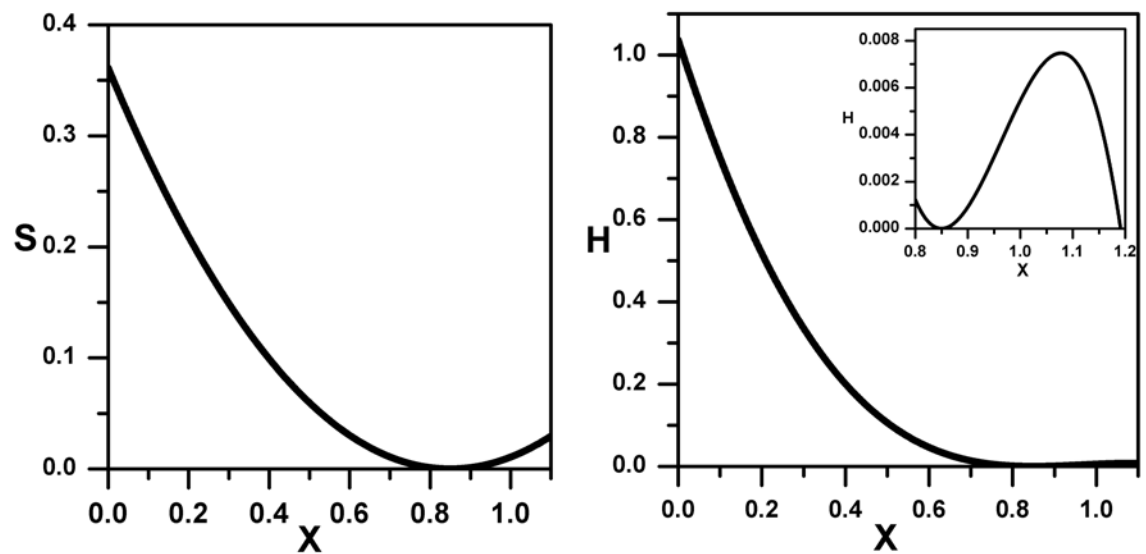
Figure 2.5 Melting line for the chose parameters in Table 1. The region below the melting line represents the crystalline state. The arrow shows the triple point at $(\tilde{T}_c, \tilde{X}_c) = (0.900, 0.850)$.



(a)

(b)

Figure 2.6 Free energy barrier (a) and chemical potential change (b) along the melting line (Figure 2.5) for the chosen parameters in Table 1.



(a)

(b)

Figure 2.7 Entropy change (a) and Enthalpy change (b) along the melting line (Figure 2.5) for the chosen parameters in Table 1.

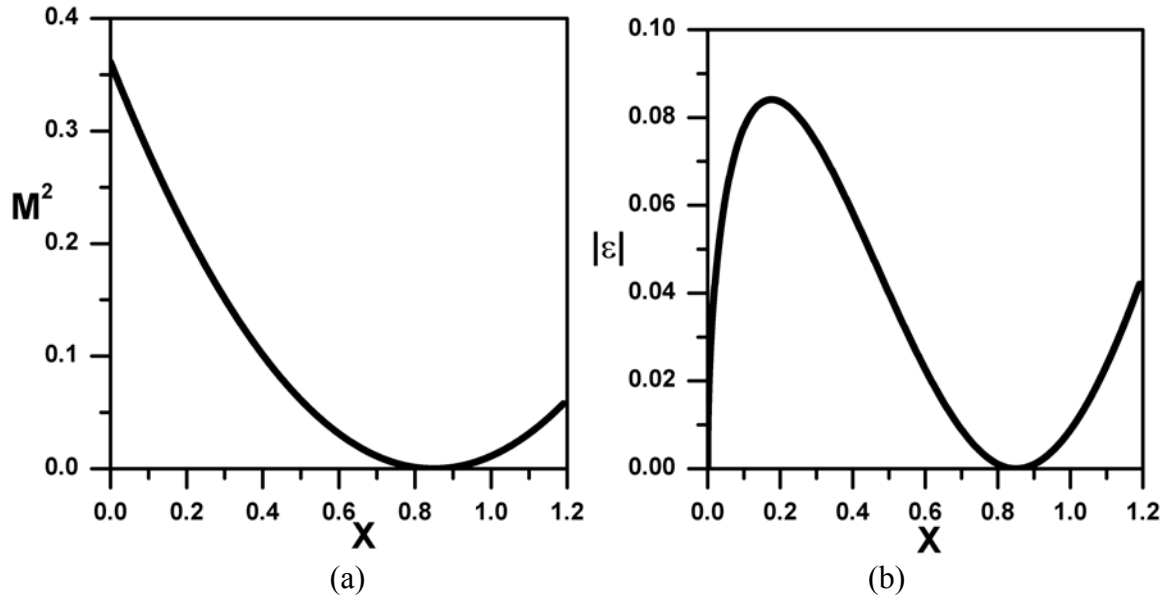


Figure 2.8 Mean square order parameter values change (a) and absolute value of shear strain change (b) along the melting line (Figure 2.5) for the chosen parameters in Table 1.

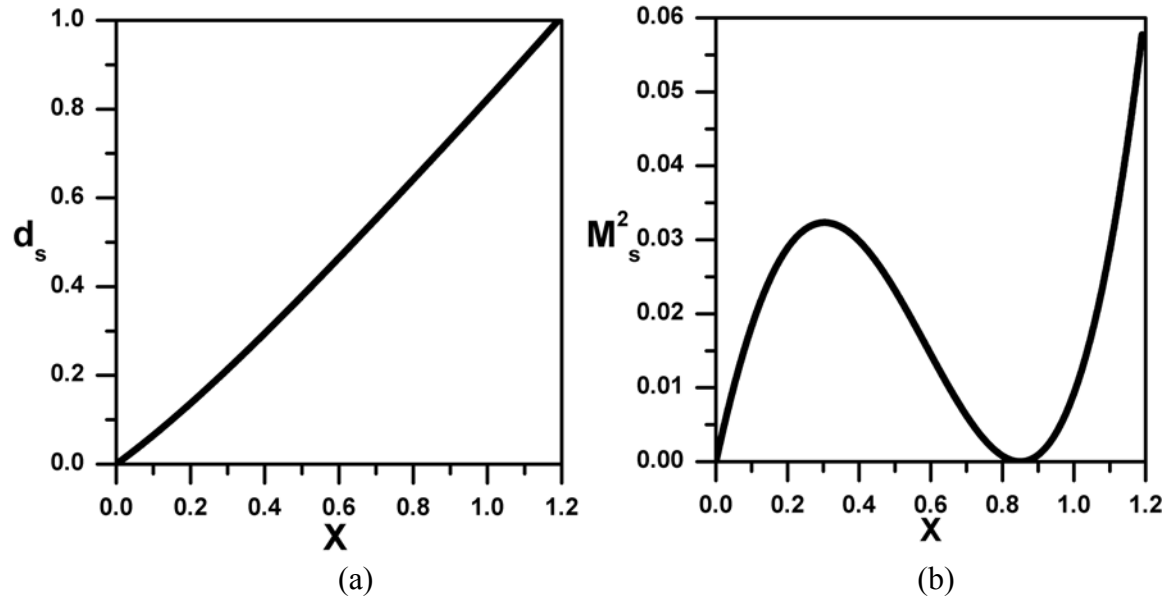


Figure 2.9 $d_s = 1 - \frac{T_m^d}{T_m^0}$ indicating the contribution from static disorder (a) and mean square static atomic displacement change (b) along the melting line (Figure 2.5) for the chosen parameters in Table 1.

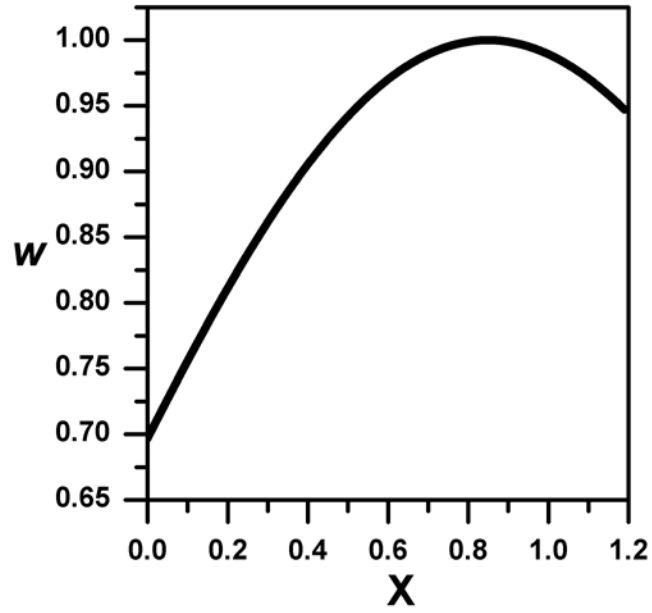


Figure 2.10 $w = \exp(-\Delta S)$ that probability is defined as $p = (\exp(-\Delta S))^\lambda$ for heterophase fluctuations of liquid-like clusters and λ is some positive constant (parameters in Table 1).

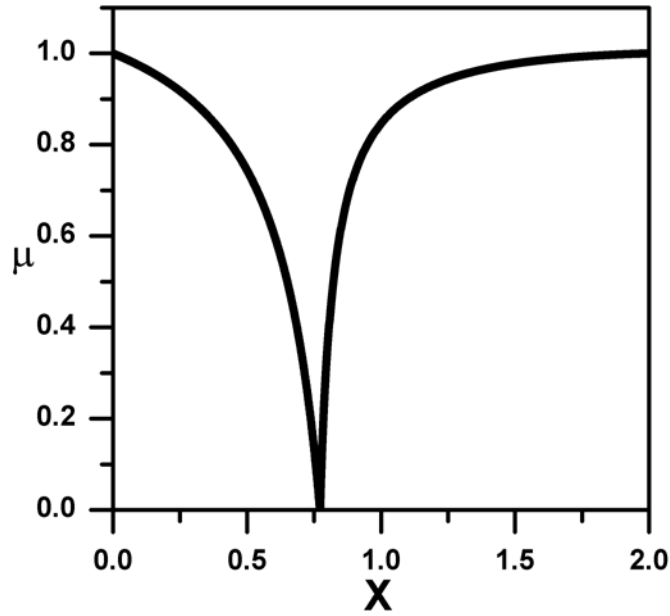


Figure 2.11 Shear elastic constant as a function of composition at the triple point temperature $T=1.1$ for the chosen parameters in Table 1.

The effective Debye temperature θ_d for the disordered crystal is

$$\theta_d^2 = \theta_0^2 \left(1 - \frac{\langle u_{sta}^2 \rangle}{\langle u_{dyn}^2 \rangle} \right), \quad (2.30)$$

and also the average shear modulus is defined as

$$\mu = \left(\frac{1}{const} \frac{k_B}{h} \right)^2 \left(\frac{4\pi V_a}{3} \right)^{2/3} \rho \theta_d^2$$

(V_a , atomic volume, ρ , density). Thus, we have

$$\frac{T_m}{T_m^0} = \frac{\theta_d^2}{\theta_0^2} = \frac{\mu}{\mu_0} = \left(1 - \frac{\langle u_{sta}^2 \rangle}{\langle u_{cri}^2 \rangle} \right). \quad (2.31)$$

From Figure 2.9(a), we can clear see the increasing contribution from static displacement for the melting, which induced by the impurities, with the approximation $M^2 \approx M_{dyn}^2 + M_s^2$ and the static disorder does dominant during the amorphization process at low temperature. And chemical disorder also play more important role for low temperature melting [18, 28] (Figure 2.9(b)). At fixed temperature, the softening effect of the static disorder on the average shear modulus is shown in Figure 2.11. At the transition point, shear modulus reaches zero. The lattice instability induced by the softening of long--wave acoustic modes indicates the onset of the low temperature melting---amorphization [6, 28] (Figure 2.11).

In Figure 2.6(b), chemical potential difference indicates $\Delta\mu \leq 0$. At the three-phase coexisting point, $\Delta\mu = 0$. Since the positive enthalpy of fusion shows that the positive heat of mixing couldn't provide the driving force for phase transition, the stored elastic

energy could be the origin to lower the free energy of the crystal phase. The chemical potential will drive the crystal solids into the stable amorphous phase.

2.2.5 Exothermic Melting----Reentrant melting

Beside the normal melting point at high temperature, a solid solution could have the other melting scenario at low temperature, for which the entropy change is negative and the amorphous phase becomes more stable than the metastable crystal state. This situation has been called inverse melting and characterized by reentrant behavior that the melting line is bent over and entering into low temperature range in a binary phase diagram [30, 31, 33]. For the reentrant behavior, we need to consider a polynomial of degree two in T , which is determined by the parabolic nature of the T-X line near the triple point [32].

$$\tilde{A}(T, X) = \tilde{A}_0(X) + \tilde{A}_1(X) \cdot (T - \tilde{T}_0) + \tilde{A}_2(X) \cdot (T - \tilde{T}_0)^2 \dots \quad (2.32)$$

The corresponding formulas for the neutral stability point T_1 , transition point T_m , and critical point T_0 are:

$$\begin{aligned} \tilde{A}_2(X) \cdot (T_1 - \tilde{T}_0)^2 + \tilde{A}_1(X) \cdot (T_1 - \tilde{T}_0) + \tilde{A}_0(X) &= \frac{C^2(X)}{3E}, \\ \tilde{A}_2(X) \cdot (T_m - \tilde{T}_0)^2 + \tilde{A}_1(X) \cdot (T_m - \tilde{T}_0) + \tilde{A}_0(X) &= \frac{C^2(X)}{4E}, \end{aligned} \quad (2.33)$$

$$\tilde{A}_2(X) \cdot (T_0 - \tilde{T}_0)^2 + \tilde{A}_1(X) \cdot (T_0 - \tilde{T}_0) + \tilde{A}_0(X) = 0,$$

and more details is in Appendix A. The coupling function has the following form at low temperature:

$$e(T, X) = \begin{cases} \left(\left(\alpha_0 - \alpha_1(T - T_0 + \Delta) - \alpha_2(T - T_0 + \Delta)^2 \right) X \right)^{1/2} & X \leq X_m \\ \left(\left(\beta_0 - \beta_1(T - T_0 + \Delta) - \beta_2(T - T_0 + \Delta)^2 \right) (\tilde{X} - X) \right)^{1/2} & X \geq X_m \end{cases} \quad (2.34)$$

The function A in Eq. (4) has the following form:

$$A(T, X) = A_0(X_0 - X) + A_1(T - T_0) + A_2(T - T_0)^2 \quad (2.35)$$

After the renormalization, we have:

$$\begin{aligned} \tilde{A}(T, X) = & \left(A_0 + \frac{\alpha_0}{2\mu_0} \right) (\tilde{X}_c - X) + \left(A_1 + \frac{\alpha_1 X}{2\mu_0} - 2A_2\Delta \right) (T - \tilde{T}_c) + \left(A_2 + \frac{\alpha_2 X}{2\mu_0} \right) (T - \tilde{T}_c)^2 \\ & + \left(A_0 \cdot \delta - \frac{\alpha_0}{2\mu_0} (X_0 - \delta) - A_1 \cdot \Delta + A_2\Delta^2 \right) \end{aligned} \quad (2.36)$$

We choose the parameters with the following relations:

$$\begin{aligned} \tilde{X}_c &= \tilde{X}_0, \quad \tilde{T}_c = \tilde{T}_0, \quad \tilde{A}_0 = A_0 + \frac{\alpha_0}{2\mu_0}, \quad \tilde{A}_1(X) = A_1 + \frac{\alpha_1 X}{2\mu_0} - 2A_2\Delta, \quad \tilde{A}_2(X) = A_2 + \frac{\alpha_2 X}{2\mu_0} \\ A_0 \cdot \delta - \frac{\alpha_0}{2\mu_0} (X_0 - \delta) - A_1 \cdot \Delta + A_2\Delta^2 &= 0 \end{aligned} \quad (2.37)$$

Finally, we get the normalized coefficient:

$$\tilde{A}(T, X) = \tilde{A}_0 \cdot (\tilde{X}_c - X) + \tilde{A}_1(X) \cdot (T - \tilde{T}_c) + \tilde{A}_2(X) \cdot (T - \tilde{T}_c)^2 \quad (2.38)$$

We still use the same form for $C(X)$ as Eq. (2.19). The functions of temperature in Eq. (2.38) have the quadratic forms and could give two solutions with the appropriate parameters. The extreme point is chosen at $(\tilde{T}_c, \tilde{X}_c)$. Based on the physics of polymorphic melting, for the high temperature melting (larger than \tilde{T}_c), the necessary condition is $T_1 < T_m < T_0$. For the reentrant melting (smaller than \tilde{T}_c), we have $T_1 > T_m > T_0$ with the right choice of parameters.

From the numerical solution, we obtain the melting line (T_m line) with $\Delta f = 0$ in Figure 2.12. Along the melting line, both the energy barrier in Figure 2.13(a) and the mean square order parameter Figure 2.15(a) are decreasing with the increasing composition for high temperature melting and reach zero at the triple point $(\tilde{T}_c, \tilde{X}_c)$. Since $C(X)$ does not depend on the temperature, the energy barrier and the mean square order parameter value are no difference for high temperature melting and low temperature melting. But the amplitude of shear strain at low temperature is increasing with the decreasing composition after it reaches zero at the triple point. At the beginning, the amplitude of shear strain at high temperature melting is increasing and will decreasing with the increasing composition once beyond certain point (Figure 2.15(b)). That bump shows the original crystal solid is weaken by the addition of the solute atoms. That weakening process is induced by the static disorder caused by the solute atoms (Figure 2.16). Because of the weakening, the melting temperature is decreasing (Figure 2.12), the less energy is needed for phase transition and the jump for the order parameter

Table 2 Parameter values for exothermic melting

T_0	X_0	E	μ_0	Δ	A_0	A_1	A_2	C_0	C_1	α_0	α_1
1	1	1	1	0.100	2	-1	-1.500	0.150	1	0.906	1.647

Table 2 Parameter values for exothermic melting (continued)

A_2	β_0	β_1	β_2
-0.850	0.953	0.100	-0.100

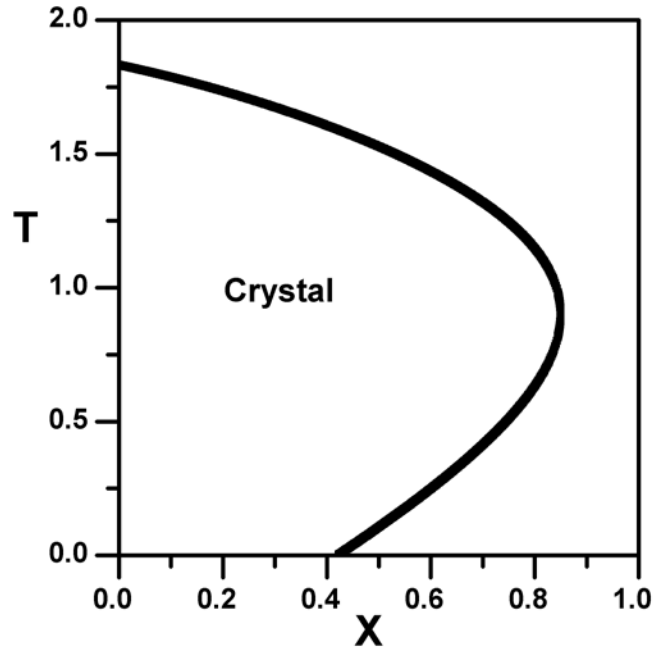


Figure 2.12 Melting line with triple point $(\tilde{T}_c, \tilde{X}_c) = (0.900, 0.850)$ for the chosen parameters in Table 2.

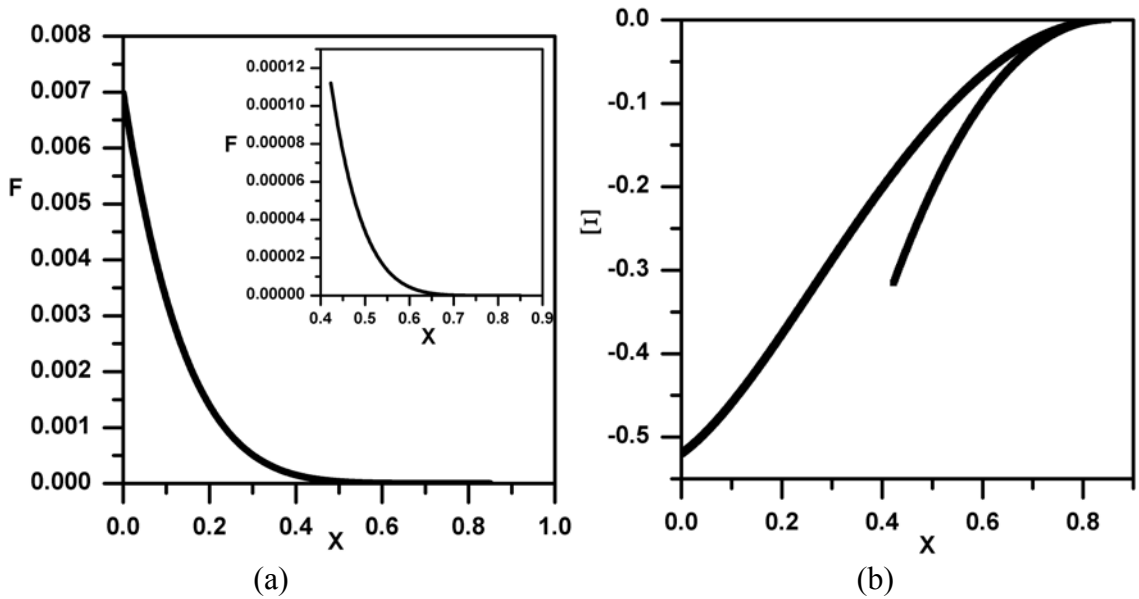
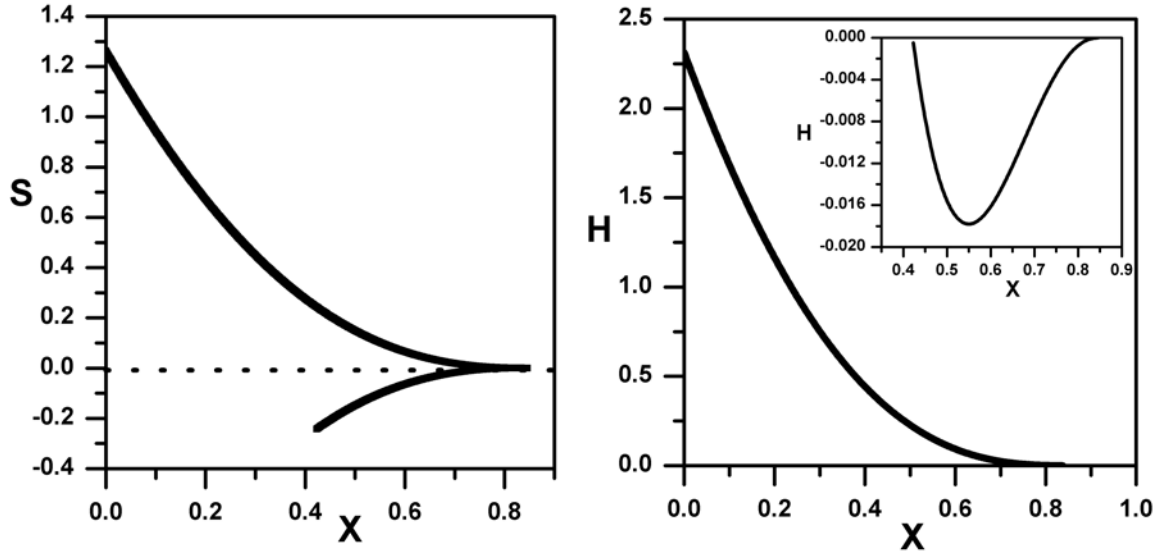


Figure 2.13 Free energy barrier (a) and chemical potential change (b) along the melting line (Figure 2.12) for the chosen parameters in Table 2.



(a) (b)
Figure 2.14 Entropy change (a) and Enthalpy change (b) along the melting line(Figure 2.12) for the chosen parameters in Table 2.

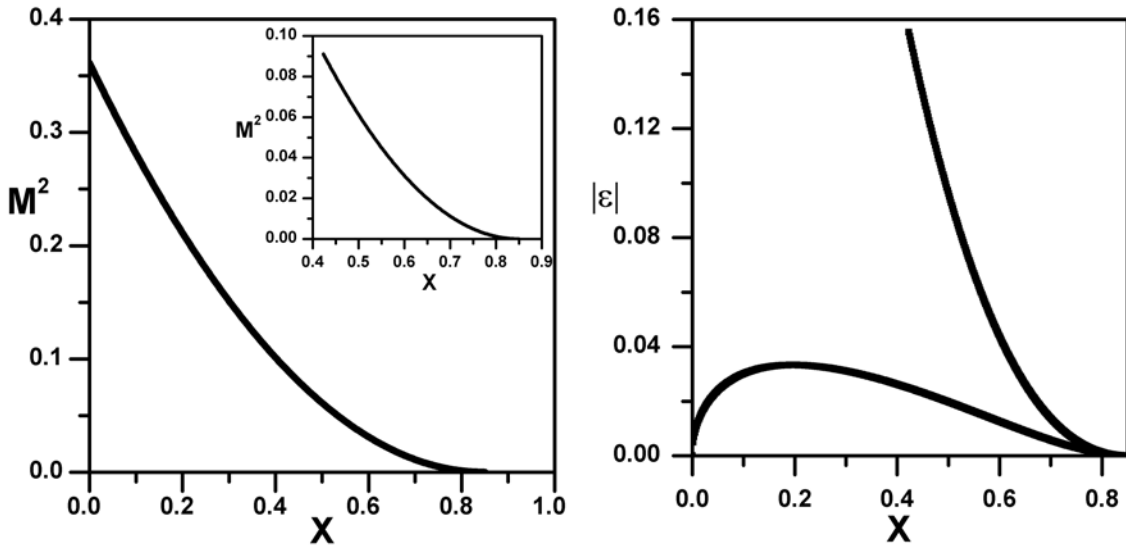


Figure 2.15 Mean square order parameter values change (a) and absolute value of shear strain change (b) along the melting line (Figure 2.12) for the chosen parameters in Table 2.

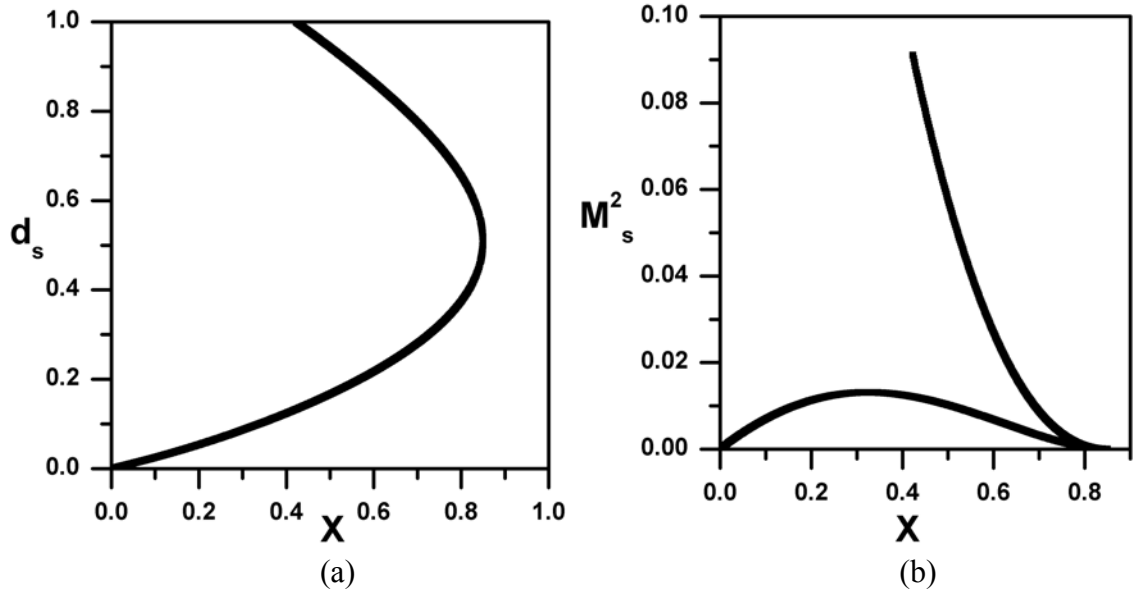


Figure 2.16 $d_s = 1 - \frac{T_m^d}{T_m^0}$ indicating the contribution from static disorder (a) and mean square static atomic displacement change (b) along the melting line (Figure 2.12) for the chosen parameters in Table 2.

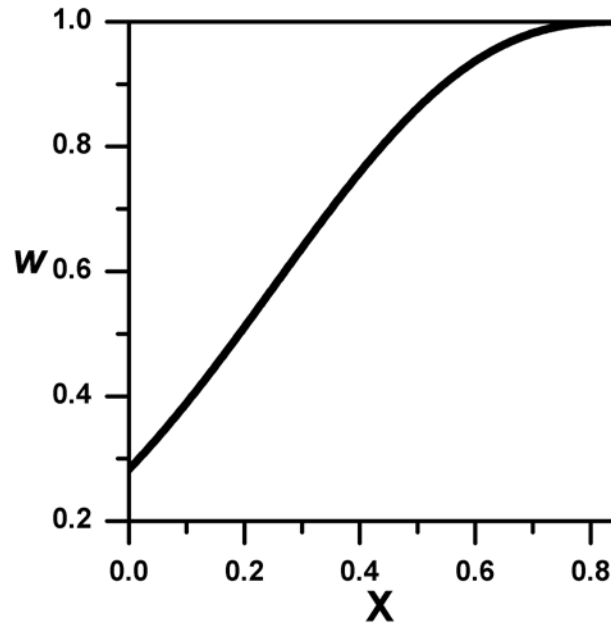


Figure 2.17 $w = \exp(-\Delta S)$ that probability is defined as $p = (\exp(-\Delta S))^\lambda$ for heterophase fluctuations of liquid-like clusters and λ is some positive constant (parameters in Table 2)

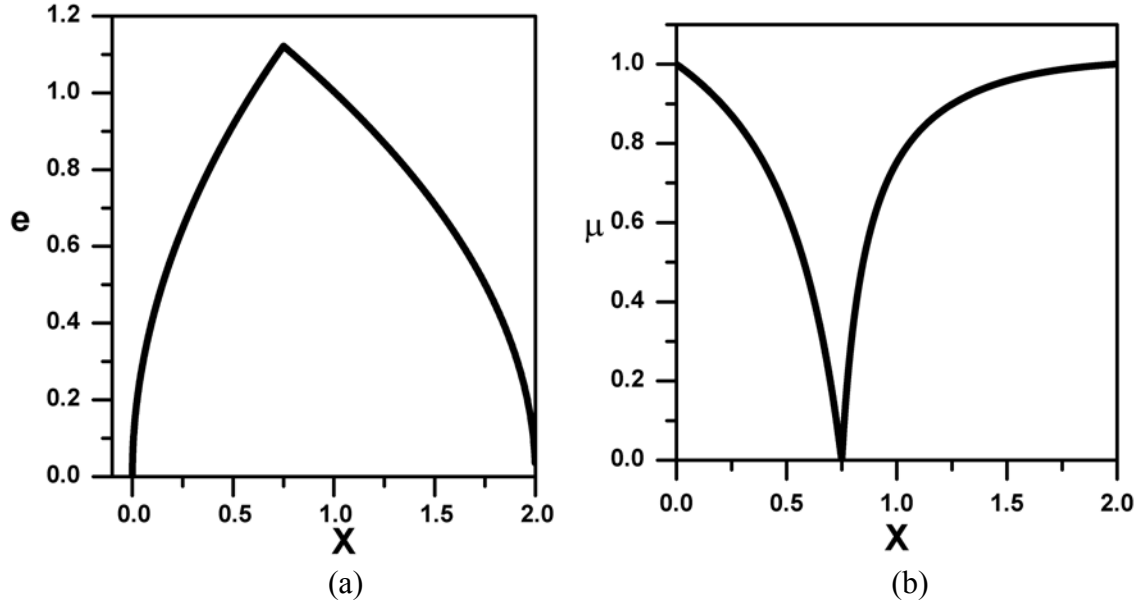


Figure 2.18 Coupling function (a) and shear elastic constant (b) as a function of composition at the triple point temperature $T=0.509$ for the chosen parameters in Table 2.

value is smaller (Figure 2.13(a) and Figure 2.15(a)). Also for the reentrant melting, the static disorder will play dominant role for phase transformation since the dynamic disorder is decreasing at low temperature (Figure 2.16(a)). And it also suggests the atomic scale distortion by atomic size mismatch and the amplitude of the accompanying strains increase with decreasing temperature (Figure 2.16(b)). The entropy change along the melting line is decreasing (Figure 2.14(a)) with the increasing composition and keeps positive until it becomes zero at the triple point. Then it turns into negative and continue to decrease along the melting line. That shows the exothermic case proposed by Fecht and Johnson [5]. The negative enthalpy of fusion indicates that the negative heat of mixing is necessary condition for reentrant melting, which providing the driving force for the formation of amorphous phase (Figure 2.14(b)). The small bump shows the competition process between the static disorder and the dynamic disorder. The elastic

softening of the crystal lattice is caused by the impurities and reaches zero at the transition point.

The origin of re-entrant behavior for amorphization is explained by the existing chemical short-range order in amorphous phase, which is responsible for the negative excess entropy value along the melting line [30, 31, 33]. For the entropy of a binary solid solution system, there are three major parts: (i) a contribution from vibrations, caused by the variation in force constants and frequency; (ii) a contribution from the anharmonicity; (iii) a contribution from the configurations. For the amorphous phase from low temperature melting, an excess of low frequency vibrations over the corresponding crystal state is one of the anomalies of glass properties, indicated by the boson peak observed in inelastic light (Raman) and Neutron scattering densities. Anharmonicity and disorder are used to develop various models to try to understand the physical origin of the boson peak. One of the interesting explanations is taking into account the interplay between anharmonicity due to temperature and compositional fluctuations, which is responsible to stabilize the harmonic vibrational modes, and disorder [34,35]. At low temperature, the first two contributions could be small and the decreasing configurational contribution induced by the short-range order could make the excess entropy be negative.

From Eq. (2.34), the excess entropy is defined as $S = -[\tilde{A}_1(X) + 2\tilde{A}_2(X)(T - \tilde{T}_c)]M^2$ and the sign of S is depending on the competition between $\tilde{A}_1(X)$ and $2\tilde{A}_2(X)(T - \tilde{T}_c)$.

Along the low temperature melting line, we have $S < 0$ with $\tilde{A}_1(X) < 0$, $\tilde{A}_2(X) < 0$ and

$T_m < \tilde{T}_c - \frac{\tilde{A}_1(X)}{2\tilde{A}_2(X)}$. The linear dependence on temperature is from the coefficient of the

quadratic term of order parameter and the coupling coefficient between the strain and

order parameter. Experimentally, chemical short-range order does depend on the alloy composition and temperature in disordered solids, and it could induce large changes in the vibration for one-dimensional model [36, 37, 38]. And its influence on glass-forming ability is also discussed that chemical ordering is important although the atomic size plays the main role for normal melting [39, 40]. Based on the microscopic theory of configuration free energy in solid solutions, the chemical part comes from the atomic configuration and elastic energy depends on the configurational and positional degree of freedoms. For binary cases, short-range order could bring the extra ordering energy in comparing the random distributions of solute atoms [41, 42]. In our Landau free energy, the enhanced short-range order effect could rely on temperature, composition and elastic degree of freedom from the coupling coefficient for the reentrant melting. Since the random mixture is the reference state, the elastic contribution could make a limited contribution to decrease the enthalpy and the pronounced short-range order could induce the relatively lower entropy. For endothermic melting, the amount of increasing entropy contribution from vibration and anharmonicity may exceed the decreasing part from configurations by increasing temperature or composition and the excess entropy could be positive. For that situation, the atomic mismatch will provide the thermodynamic driving force for the phase transformation even with the developed short-range order in the amorphous phase.

From our model, the melting line could be further extrapolating to zero temperature and still show negative excess entropy, caused by the decreasing number of available zero-temperature configurations for amorphous phase over the metastable crystal state. However, it is unreasonable for another argument that the entropy should be zero for the

frozen in disordered state at zero temperature [19, 43]. This behavior is clearly a violation of the third law of thermodynamics for the metastable crystal phase, ‘Kauzmann paradox’.

2.3 Summary: Endothermic Melting and Exothermic Melting

With our simplified model, equilibrium thermodynamics are used to study melting and solid-state amorphization. Based on the proposed Landau theory of polymorphic melting for binary solid solutions, the addition of impurities (alloy elements) weaken the original crystal lattice, lower the melting temperature and cause the elastic softening with phase transition. Shear elastic instability happens right at the transition point, which means the connection between thermodynamic instability and mechanical instability based on vibrational instability [14]. Position disorder and chemical disorder are used to describe the topologic disorder, and their coupling effect is stressed for the topological order-disorder transition in disordered crystals. At high temperature melting, the system needs to absorb the heat and the induced static disorder plays important role during the process. Vibration of atoms induced by thermal effects governs the event. Energy barrier, entropy change and enthalpy change are decreasing with the increasing composition along the melting line. Finally, they reach zero value at the triple point. At low temperature melting, the static disorder plays the dominant role for solid-state amorphization. For endothermic melting, the elastic energy induced by the atomic size mismatch provides the driving force since the enthalpy of fusion is positive. Experiments show that the binary systems with the positive heat of mixing allow the formation of amorphous phase driven by mechanical condition. For reentrant behavior, the negative enthalpy of fusion is

the necessary condition for solid-state amorphization. The crystal phase is unstable at any temperature once beyond the composition value at the triple point.

CHAPTER III

FLUCTUATIONS AND NUCLEATION IN INHOMOGENEOUS BINARY SOLID SOLUTIONS

3.1 Amorphous Structure and Phase Transitions in One Dimension

A real one-dimensional glass does not exist. However, there is a well-defined base lattice in one dimension and a one-dimensional glass model may show some significant results to be helpful to understand the real two and three-dimensional amorphous solids. For disordered alloys, the imposed disorder may be well considered in one dimension rather than the dimensionality. In two and three dimension, topological defects are considered to play a crucial role for melting [44--47]. Quasi-one dimensional systems do exist, e.g., amorphous Boron nanowires and Co-B amorphous alloy nanochains [48--50] (Figure 3.1). Also one-dimensional model may be applied to layered structures with randomness in atomic positions and compositions along one direction [51]. One-dimensional models of disordered solids have been studied extensively, which include liquids, ordered alloys and random alloys, based on different information on short-range and long-range order. For the liquid models, the interatomic spacing is characterized by a definite continuous probability distribution with short-range order, which is originally proposed by Gubanov [52--60] (Figure 3.2). The atomic positions are randomly arranged for disordered-alloy models and atomic species are related to discrete probabilities. One-dimensional chaotic maps are also proposed to model quasi-crystals and amorphous materials [61--64]. In a temporal chaotic nonlinear dynamical system [65], the evolution

of the system is only predictable for short time scale in the corresponding phase space. Amorphous solids have a similar spatial behavior, which show short-range correlations at the atomic length scale without long-range order. To examine the analogy between spatial chaos and amorphicity, Reichert and Schilling [62] used the baker transformation to build a mathematical model that has one-dimensional chaotic configuration. Later on, they developed a physical model by an infinite chain of identical classical particles with anharmonic and competing interactions [63] (Figure 3.3).

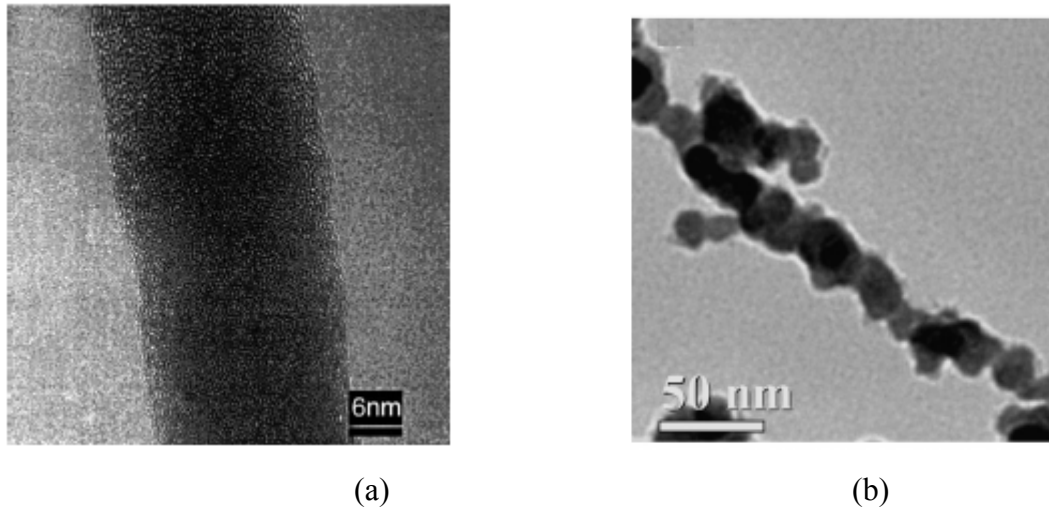


Figure 3.1 (a) A high-resolution transmission electron microscopy image of a single amorphous boron nanowire [48, 49]; (b) A transmission electron microscopy image of amorphous Co-B chain [50].

In 1950, van Hove showed that thermodynamics phase transition, which is defined as singularities of the free energy, does not occur in particle systems with pair interactions of sufficiently short range [66]. That mathematical result is called von Hove's theorem, which is applied to homogeneous system for pairwise potentials with a hard core and a cut-off under no external fields. It has been extended to one-dimensional continuous

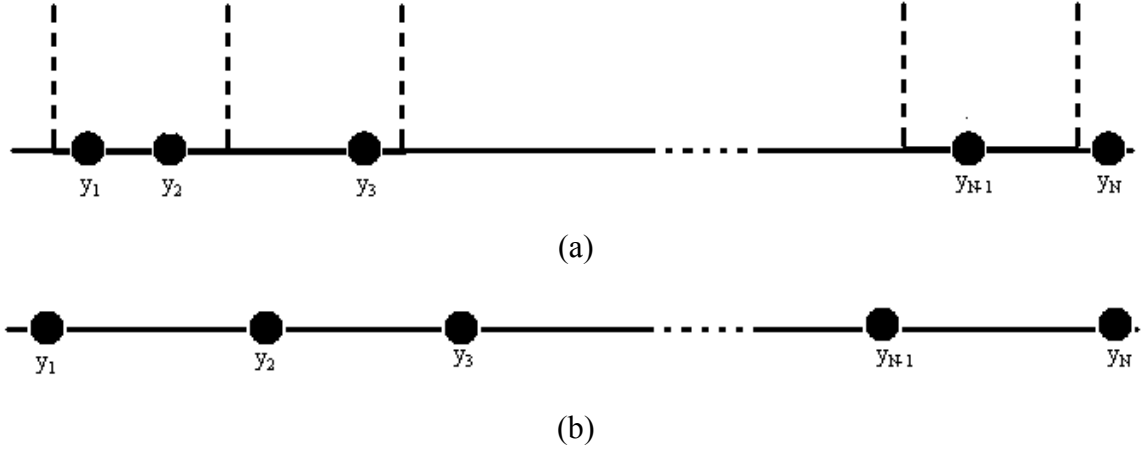
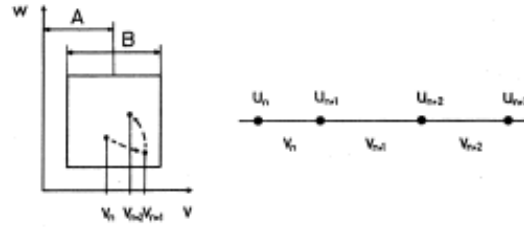
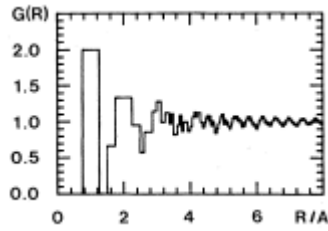


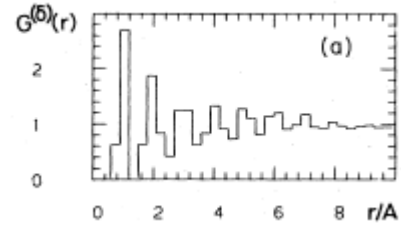
Figure 3.2 (a) ordered chain model with the atomic position as $y_i = d_0 + \varepsilon_i d_0$ and $\langle y_i \rangle = d_0$; (b) disordered chain model with the interatomic distance as $y_i - y_{i-1} = d_0 + \varepsilon_i d_0$ and $\langle y_i - y_{i-1} \rangle = d_0$.



(a)



(b)



(c)

Figure 3.3 One-dimensional amorphous model by the Baker transformation with $u_{n+1} - u_n = v_n = A + Bx_n$. (a) the orbits of the Baker transformation and the corresponding atomic configurations; (b) amorphous-like pair correlation functions obtained using the Baker transformation; (c) amorphous-like pair correlation functions obtained using a nonlinear potential model.

(gases) and discrete system (Ising model, lattice gas) with short-range interaction [67].

Landau's argument reinforces this point of view, which shows that domain walls will make contribution of entropy and make macroscopic phase coexistence impossible at any positive temperature [68]. His argument does apply to a large class of one-dimensional systems (short range $S=1/2$ Ising model, the ϕ^4 model, etc) though it is not a rigorous result and only physically intuitive. However, it is established that phase transitions could occur in the one-dimensional discrete (lattice gas [69], Ising model [70] and helix-coil transition [71]) and continuous (fluid model [72]) systems with long-range interactions. For example, one-dimensional Ising models with $1/r^{1+\sigma}$ ferromagnetic interactions are known rigorously to exhibit a phase transition if $\sigma \leq 1$ but no long range order if $\sigma > 1$ [70] (Figure 3.4).

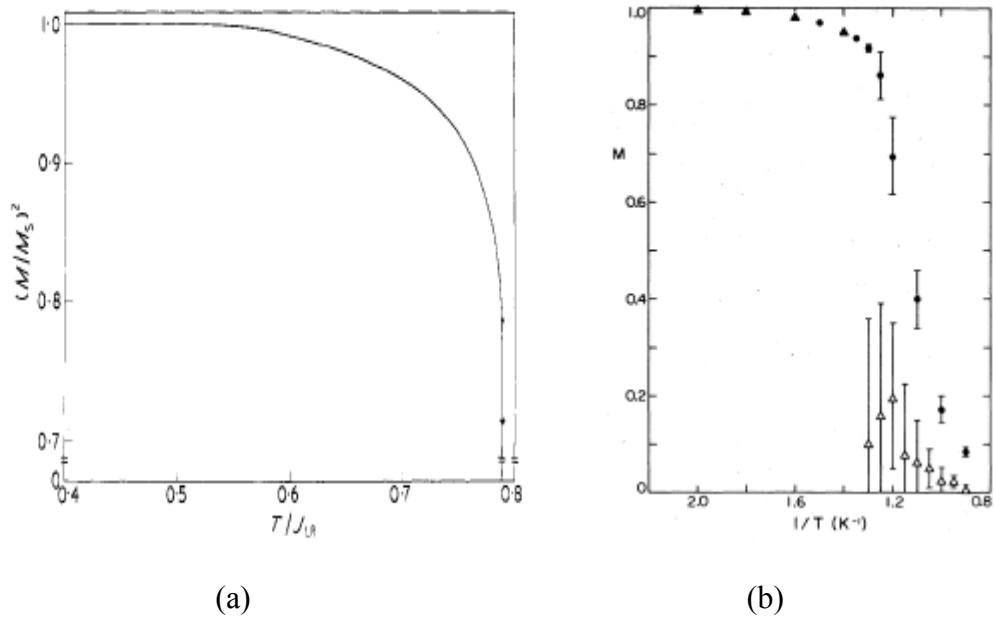


Figure 3.4 First order phase transition in an Ising ferromagnet chain with discontinuous long-range order. Magnetization as a function of temperature is obtained by renormalization group methods (a) and by Monte Carlo calculation (b) [70].

In one-dimensional inhomogeneous systems, there are no rigorous mathematical results to predict nonexistence of phase transitions. There are examples that show the existence of phase transitions in one-dimensional systems with quenched disorder. Heterogeneous DNA melting is an example of the influence of structural disorder by hydrogen bonds onto order-disorder transitions in one-dimensional systems [73]. One type of “2D wetting” transitions near a random one-dimensional wall is in fact one-dimensional problem in the mathematical sense [74, 75].

Fisher discussed the solid-liquid transition in a one-dimensional continuous system and a lattice gas model with long-range interaction [76, 77]. Based on the long-range behavior of the pair distribution function, which is defined as the ratio of the local number density at a distance r to the average number density, around a central particle, phase diagram on the temperature-density is discussed and the existence of a triple point of gas-like, liquid-like and crystal-like states is mentioned. Recently, the pair distribution function is also calculated in homogeneous mixtures and inhomogeneous mixtures in one-dimensional systems [78, 79].

Melting behavior in metallic nanowires, which show clear characteristic first order phase transition for thick nanowires, has drawn people’s attention in recent years experimentally and theoretically. Computer simulations provide an opportunity to investigate the thermodynamic instability and melting processes at the atomic scale. In general, the melting of a crystalline solid will initiate at the surface layer and propagate into the interior. Melting also could proceed by simultaneous disordering of all shells, or start from inner core shell atoms in metallic nanowires [80, 81, 82]. Dimensionality and size effect along the transverse direction do play important roles on the thermal and

mechanical properties of nanowires, e.g. no clear indication of first-order transition in ultrathin titanium sample [83]. At low temperature, structural phase transitions (solid-solid transitions) do exist and compete with melting process with increasing temperature in nanowires and nanoclusters. In alloy nanomaterials, the composition dependence of thermodynamic states is clearly indicated by the temperature and composition phase diagram, e.g. FCC to HCP transitions and melting transition in Pd nanowires [84, 85, 86]. The liquid-glass transition phenomenon is also observed in simulated nanowires with cooling by molecular dynamics, which shows the size dependence [87, 88]. In nanowires under mechanical condition, the initial crystal phase could continuously transform into the amorphous phase at high strain rate and exhibit a dramatic change in atomic short-range order accompanying a near vanishing of tetragonal shear elastic constant perpendicular to the tensile direction [89, 90]. Size mismatch effect does favor the strain-

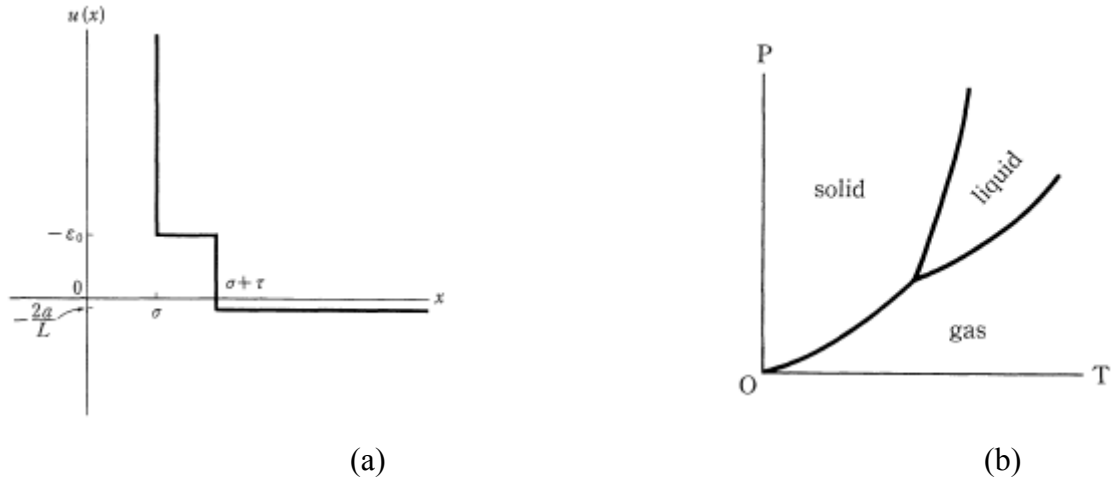


Figure 3.5 Phase transitions in one-dimensional hard-core model with intermolecular potential for $\epsilon_0 < 0$ (a) and the corresponding phase diagram (b) [94, 95].

-rate amorphization in alloy nanowires. A new mode of amorphization is observed which occurs directly from the homogeneous, elastically deformed system with no chemical or structural disorder [89, 90]. A comprehensive understanding of the solid-state

amorphization mechanism is still lacking. For a one-dimensional lattice and continuous fluid model, a triple point could exist for certain parameter ranges when the hard-core potential has both a short-range repulsion and a long-range attraction [91--98] (Figure 3.5). From above discussions, we are confident to talk about the existence of long-range order and the possibility of phase transitions in one-dimensional systems in the following sections.

3.2 Homophase Fluctuations and Heterophase Fluctuations

There are two kinds of fluctuations in metastable solid solutions with first order phase transitions: homophase fluctuations and heterophase fluctuations. Nucleation and growth theory focuses on the distribution of heterophase fluctuations and the growth of them, which is started by Gibbs [99] and Volmer and Webber [100]. For first order phase transition, nucleation is the initial stage that small regions reminiscent to new phase form through heterophase fluctuation. Some fluctuations with smaller than a critical size will shrink and called ‘clusters’ or ‘embryos’. Those fluctuations with greater size than the critical value will grow with a high probability and called ‘nucleus’. Heterogeneous nucleation initiated at some extrinsic sites is more general in real world and assist the formation of heterophase fluctuation. In case of absence of free surfaces or internal surfaces (grain boundaries), homogeneous nucleation could be activated by large fluctuation and the new phase is formatted spontaneously and grows subsequently. Heterophase fluctuations involve the interface free energy between two different phases and related to the localization phenomena (Figure 3.6). The embryos could be induced by

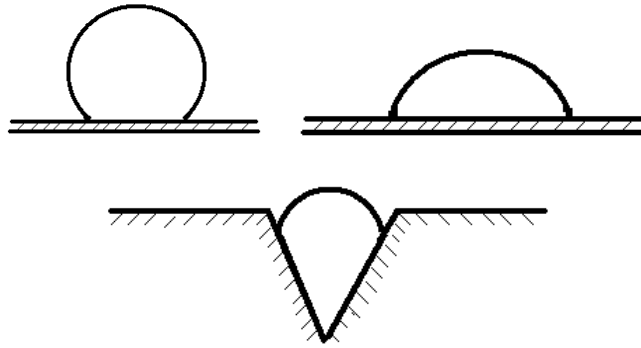


Figure 3.6 Schematic illustrations of Heterogeneous Nucleation at surfaces.

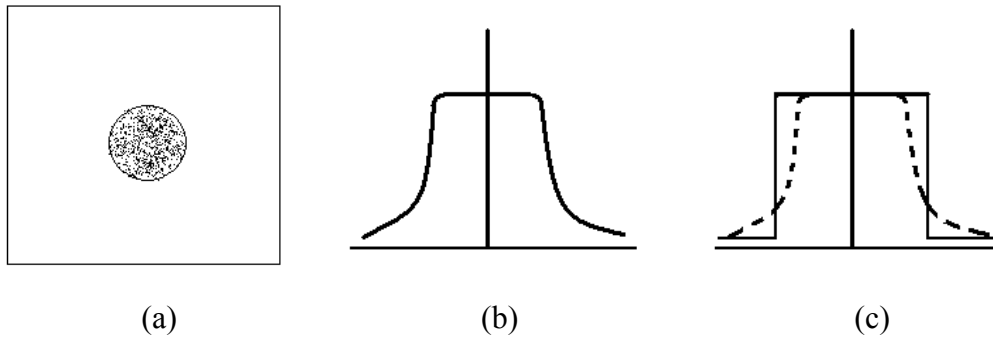


Figure 3.7 Schematic illustrations of a nucleus of Homogeneous nucleation: (a) a nucleus with dark area; (b) distribution of order parameter value in real space; (c) distribution of order parameter value for sharp interface model (solid line) and diffuse interface model (dashed line).

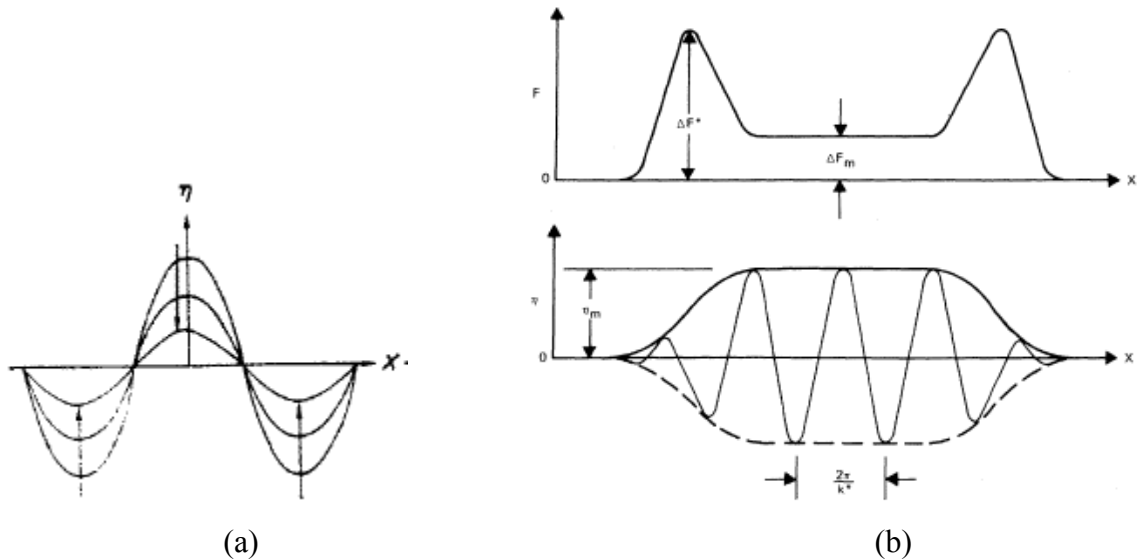


Figure 3.8 Schematic views of (a) homophase fluctuation and (b) heterophase fluctuation for first order structural phase transitions in binary alloys [101].

large fluctuations (Figure 3.7) and exist at interfaces or some foreign particles. Under certain conditions, the solid solutions may become unstable, and the small amplitude fluctuations could grow spontaneously. In most cases, homophase fluctuations will decay and be just around the stable phase.

In crystal solids, homophase fluctuations do not change the crystal symmetry and they are described by the phonons, ‘normal modes’, and called elementary excitations. On the contrary, heterophase fluctuations could break the local crystal symmetry and represented by quasi-static wave packets [101] (Figure 3.8). The microscopic mechanism of localized excitations must provide sufficient energy to activate atoms in a critical nucleus over energy barrier to the final stable phase. Large-amplitude motion of atoms and large deviation from original host lattice induced by solute atoms could play key roles as possible mechanisms for melting and amorphization in binary solid solutions.

3.3 Energy Localization in Defective Crystals: Nonlinearity and Disorder

Disorder-induced localized vibrational modes have been extensively studied for almost seventy years from theory and experiments [102]. There are three types of localized excitations in harmonic lattices: Localized, gap and resonance (or ‘quasilocalized’) modes. Localized modes is characterized by the frequency lying above the maximum frequency of the perfect host crystal, and the frequency of gap modes is found in the gap between the acoustic branch and optic branch. For both of modes, the displacements of the vibrating atoms decay exponentially from the impurity center and they are the localized normal modes of the perturbed harmonic crystal, e.g. including

small mass and large force constant defects in a monatomic lattice. If a large mass or weak force constant defect occurs the resonance mode may appear in a kind of local optic mode. The amplitude of a quasilocalized mode decays by a power law with distance from the defect. Actually, quasilocalized modes have features of localized modes and extended modes and typically are found at low frequencies [103--106]. All these type of energy localization could be treated as a result of the weak bilinear coupling between the ‘defect’ harmonic oscillator and the ‘host’ harmonic lattice.

When nonlinearity is introduced into the homogeneous lattice through interatomic interactions or some external on-site potential, intrinsic nonlinear modes, immobile or mobile [107, 108], can appear at any lattice site and are special localized with frequencies occurring outside the corresponding harmonic plane wave spectrum. The frequency of localized modes decreases with the increasing amplitude. Anharmonic resonant modes also could exist in the nonlinear lattices with negative anharmonicity terms [109--112]. When defects are added to the nonlinear lattice, localized nonlinear impurity modes could be found around the impurity sites and may be treated as intrinsic nonlinear modes trapped by the impurity [113] at low temperature. But at high temperature, these modes may be released when anharmonicity is strong enough. For the formation of the nonlinear localized modes, nonlinearity-induced modulation instability can create some excitations and increase the initial energy density of the system as the first step (Figure 3.9). After collecting energy from the other excitations, a larger excitation may be favored. Beside the localized kinetic energy, the impurity also could induce the local excitations of potential energy at low temperature. At intermediate temperature, both kinetic energy and potential energy contribute the high local energy events [114].

Both nonlinearity and disorder could be responsible for the energy localization. In disordered crystals, there are different types of localized modes and the competition between these two mechanisms will produce the complexity of localized states. They could cooperate for the formation of large amplitude nonlinear excitations [115]. At low temperature, the disorder dominates the process of the localized excitations and most of them are trapped even with the presence of nonlinearity. In the high temperature interval, nonlinearity will govern the dynamics of nonlinear energy localization with finite effect of the disorder [116, 117].

To understand the vibrational properties of glasses, inelastic photon (Raman, x-ray) and neutron scattering experiments are generally used and a peak is observed at low frequencies in the order of THz, which is called Boson peak. The Boson peak is interpreted as an excess of vibrational density of states comparing to the Debye model. And the Boson peak is also found from the heat capacity measurement of glasses, which is normalized by the Debye T^3 law, as a function of temperature. The origin of Boson peak is still in controversially debated, either collective in nature [118] or related to the localized modes [119]. And nonlinearity and disorder are used to build various alternative models, nonlinear localized potential model [119], force constant disorder model and elastic constant disorder model (a review see [35, 120]). Disorder will be critical if only harmonic degree of freedom considered and quasilocalized vibrational modes could be responsible for the peak [34]. The presence of anharmonicity and static displacements could stabilize the unstable harmonic vibrational modes, which are necessary to form the equilibrium glass structure [34].

The nonlinear localized excitations could be possible mechanism for the localized activation processes [121, 122]. Based on the detailed analytical and numerical studies of discrete lattices, e.g. DNA denaturation [122] (Figure 3.10) and Toda lattices [121], localized energy produced by nonlinear excitations at certain sites could be responsible to drive the transition over a barrier. Several attempts have been made to connect the nonlinear energy localization, which is associated with intrinsic nonlinear localized modes, with the microscopic theory of first order phase transition for homogeneous model [123, 124]. For inhomogeneous model of DNA denaturation, the disorder induced by the sequence of base pairs only could have slight effect on denaturation at high temperature, though the disorder govern the dynamics at low temperature [125, 126].

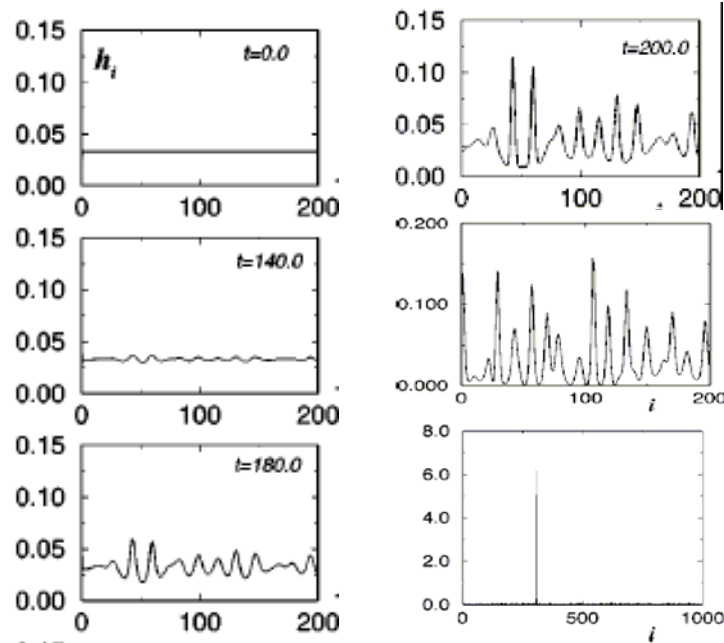


Figure 3.9 Modulation instability for the quartic FPU model from [117]. For the last two picture (from top to bottom), $t=800$ and $t=8 \times 10^4$.

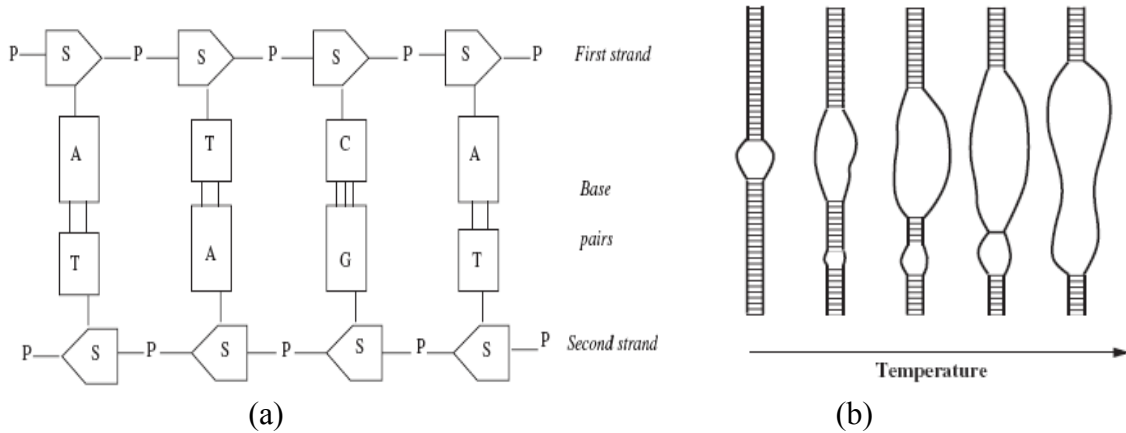
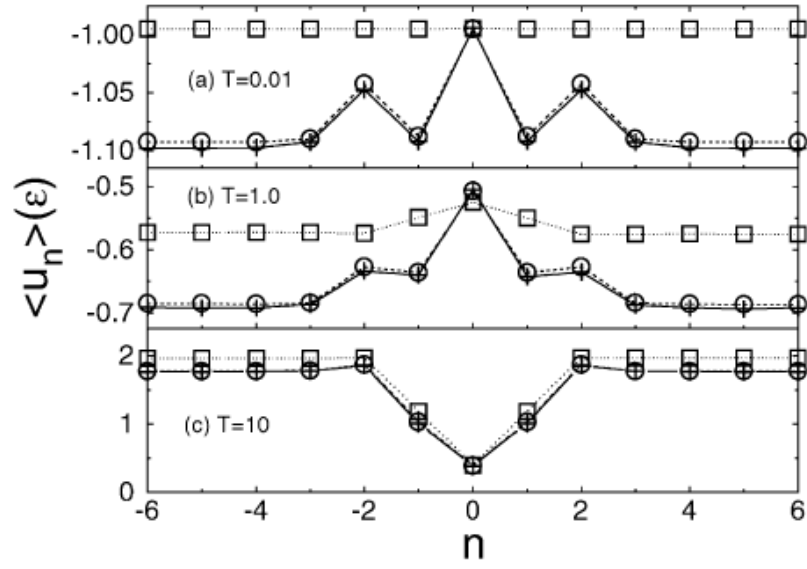


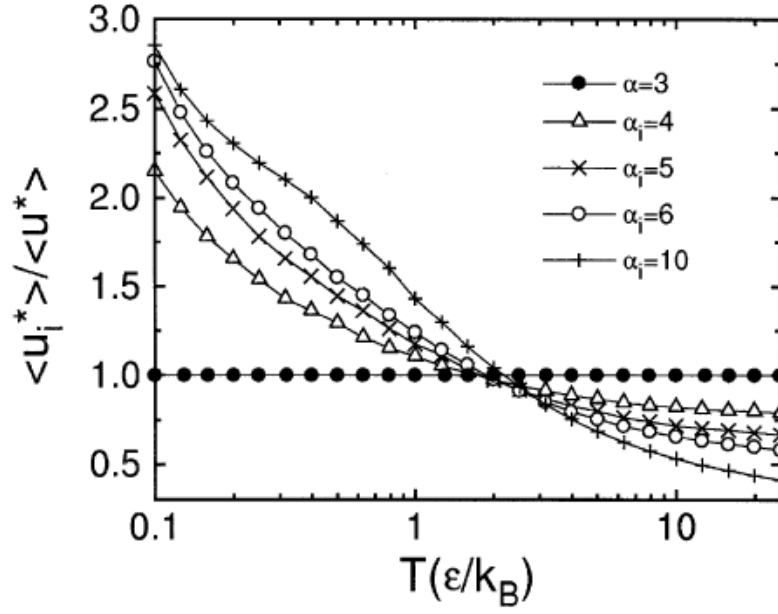
Figure 3.10 (a) Sketch of two nucleotide chains with two types of base pairs A-T (Adenine-Thymine) and G-C (Guanine-Cytosine) and (b) DNA thermal denaturation [127].

The studies show that nonlinearity and disorder could coexist and competition with each other in disordered systems, and the disorder could trap the localized excitation. As a one-dimensional model, DNA denaturation is a one-dimensional phase transition, which has short-range interactions and the appropriate nonlinearity through the coupling [124].

At high temperature, thermal energy is responsible for nonlinear energy localization in nonlinear lattices with or without impurities, though the impurities do have some influence on the properties of nonlinear thermal excitations. Investigations in nonlinear lattices show that potential energy localization is related to the impurities [128, 129, 130]. At high temperature, potential energy could be localized at impurity sites even in nonlinear lattices with next-neighbor interaction. With decreasing temperature, near-next-neighbor interaction is also involved for the potential energy localization. When reaching low temperature, long-range interaction is critical for the potential energy localization at the impurity site, which is defined by the different stiffness constant with the host particles, but it could be neglected at high temperature [130] (Figure 3.11).



(a)

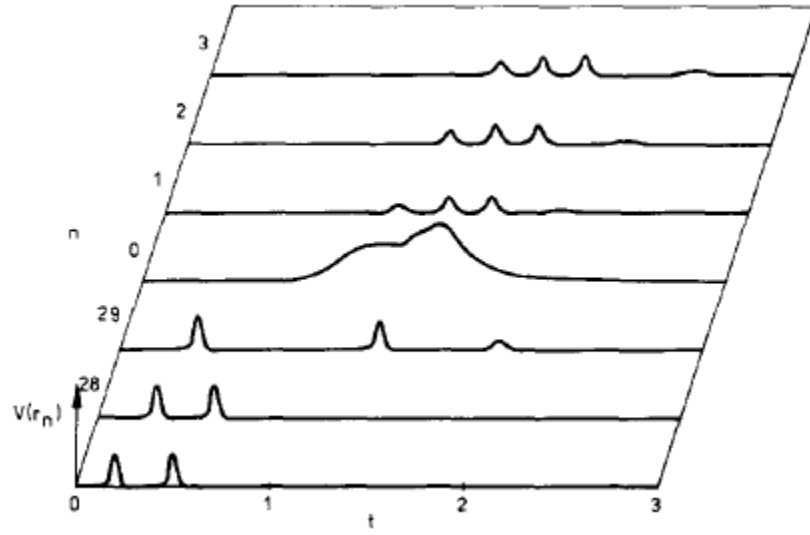


(b)

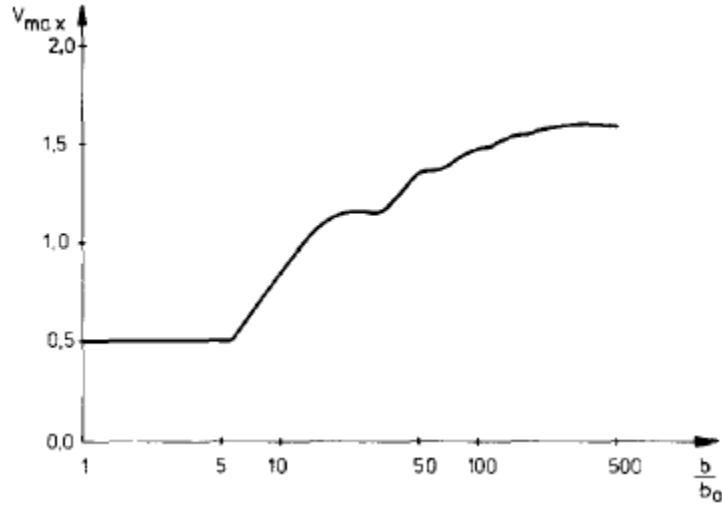
Figure 3.11 (a) The distribution of average potential energy of soft host chain with an impurity characterized by stiffness α_i at three different temperatures. (b) The ratio of the average potential energy of an impurity site to that of a host particle as a function of temperature and stiffness [130].

For solid-state amorphization caused by composition in binary solutions, frozen-in disorder could bring up mesoscopic spatial structure fluctuations since the lifetime of disorder τ_{dis} is longer than the observation time τ_{obs} . For high temperature melting, the structural fluctuations could be induced the thermal effect with $\tau_{dis} < \tau_{obs}$ [5, 131]. The intrinsic origin of melting is initiated from the energy localization induced by large amplitude localized excitations. Soliton-like excitation and fusion of these excitations (Figure 3.12), which are analogies to the soliton and soliton fusion in nonlinear lattice model, could be used to build a picture of heterophase fluctuations of polymorphic melting in binary alloys. In binary solid solutions at intermediate temperature and low temperature, heterophase fluctuations are caused by both the composition fluctuations in the unperturbed crystal lattice and subsequent structure fluctuations. In the first stage, the development of the modulational instability is induced by the composition fluctuations and small amplitude localized excitations appear. The localization could be trapped at the impurity atoms sites, where the potential energy is the dominant at low temperature, or around them. When more solute atoms are added in, those impurity atoms could act as a catalyst for the generation of a larger excitation and the interaction of these localized excitations will cause the merging of localization lengths with diminish their number. Next, more large amplitude localized excitations occur and some will have the mesoscopic length scale after merging as superposition of large amplitude elementary excitations. The critical nucleus could form, and grow when the heterophase fluctuations are large enough to overcome the critical energy barrier or be ‘eaten’ by growing grains of the new phase.

On the contrary of first order phase transition in three dimension systems, the nature of two-dimensional melting is still unclear [132]. The theory of dislocation-mediated melting of two-dimensional solids is developed by Kosterlitz and Thouless [45], Halperin and Nelson [46], and Young [47], and the possibility of two successive continuous



(a)



(b)

Figure 3.12 (a) Fusion of two solitons at an impurity site ($n=0$) in a hard lattice with the nonlinear spring parameter ratio $b/b_0=10$. (b) The maximum potential energy $V_{\max}(r_0)$ as a function of b/b_0 [133].

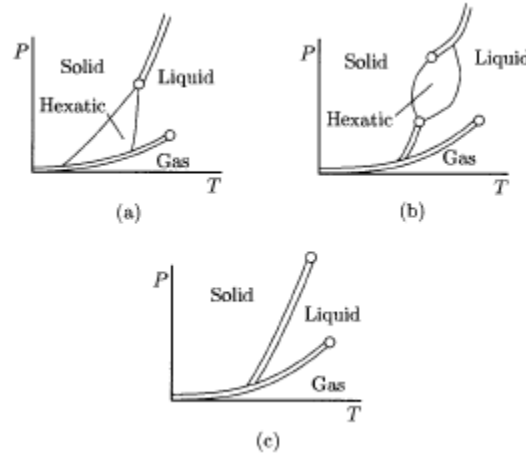


Figure 3.13 Possible pressure-temperature phase diagrams for two-dimensional model described by an attractive potential with a repulsive core. Solid, liquid, gas and hexatic phases are shown, together with double lines of first-order transitions and single lines of second-order transitions [134].

transitions for melting is suggested. The first transition is from the crystalline phase to hexatic liquid-crystalline phase through by the dissociation of pairs of dislocation. And a disclination transition is from hexatic phase to the isotropic liquid phase (Figure 3.13).

3.4 Classical and Modern Nucleation Theory

For a real critical nucleus, its maximum value should be equal to the equilibrium order parameter value. Assuming the radius of curvature of the interface is large enough comparing to the molecular dimension, called capillarity approximation, macroscopic thermodynamics are used to describe the sharp interface drop model. Also, based on the equilibrium distribution of drops, the nucleation rate could be obtained to quantify the formation of drops that exceed a critical size and grow spontaneously. Based on the classical nucleation theory [135], the excess free energy necessary for nucleation is a function of size of the spherical nucleus,

$$\Delta F = \frac{4}{3}\pi r^3 \Delta F_d + 4\pi r^2 \gamma ,$$

in which ΔF_d represents the free energy difference between the two phases and γ is the interfacial free energy (Figure 3.14). The critical size is

$$r^* = -\frac{2\gamma}{\Delta F_d} ,$$

which corresponds to the maximum value of ΔF , and a critical work is needed for nucleation

$$\Delta F = \frac{16\pi\gamma^3}{3(\Delta F_d)^2} .$$

For a nucleus with radius greater than r^* , it will continue to grow with the decreasing free energy. The number of nuclei of size r could be approximated by the Boltzmann approximation

$$m = n \exp\left(-\Delta F/kT\right),$$

where n is the number of molecules per unit volume, k Boltzmann constant, and T temperature. The nucleation rate for the homogeneous polymorphic nucleation is

$I = \nu m$, where ν is the frequency term depending on the ability of an atom to cross the interface and become a part of the new phase.

As a modification of classical theory, diffuse interface model is introduced by the Landau-Ginzburg free energy to describe an interface as an area with finite thickness that is comparable with the characteristic length of the considered system [136, 137, 138]. Recently, homogeneous nucleation process for melting in perfect crystals is considered by classical approximation and one order parameter model [139, 140]. A new type of

kinetic instability was proposed and failed to include the differences between the thermodynamics of crystals and liquids [139].

After nucleation stage, the growth of nuclei could be governed by atomic processes at the interface or controlled by diffusion conditions. For the interfacial growth, based on Avrami's approximation, the spherical volume $V_i(t) = C_d [v(t - t_i)]^d$ for a nucleus formed at t_i , where v is the interface velocity (Growth rate), d the space dimension, and C_d related to the dimension ($C_1 = 2, C_2 = \pi, C_3 = 4\pi/3$). The kinetics of a combination of nucleation and growth process could be described by the KJMA theory formulated by Kolmogorov, Johnson and Mehl, and Avrami [141--145]. The growth of droplets in systems of diffusionless first-order phase transitions was studied in terms of the time

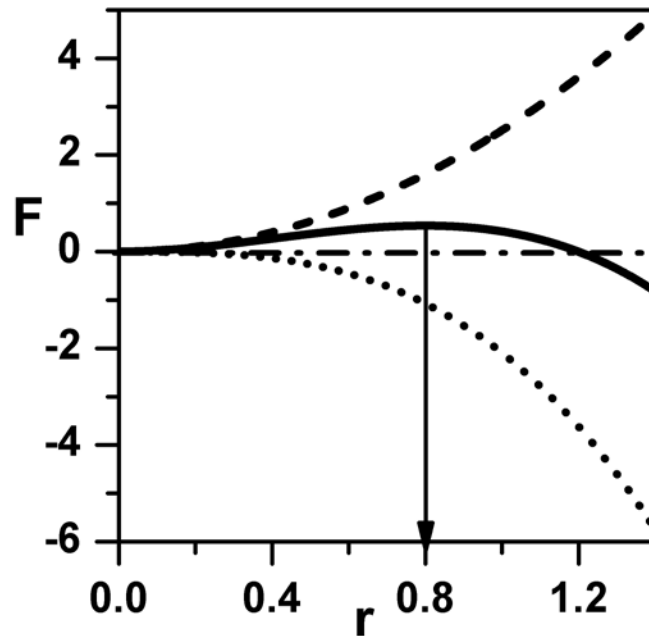


Figure 3.14 The surface (long dash line) and bulk (dot line) contributions and the total excess free energy ΔF (solid line) of a spherical nucleus depending on radius r (e.g. $\Delta F_d = -1.500$, $\gamma = 1.200$). The arrow line indicates the critical nuclei position.

dependent-Landau-Ginzburg equation with a non-conserved order parameter [146]. Based on the sharp interface model, the growth law is $r \propto t$ by the solitary wave analysis.

In the Landau-Ginzburg theory, we will use the order parameter model to examine the homogeneous nucleation and heterogeneous nucleation of polymorphic melting in binary solid solutions. Frenkel studied premelting phenomena in crystals, which show an abnormally increase of specific heats and thermal expansion coefficients slightly above the thermodynamic melting temperature, as an example of heterophase fluctuations [147]. The heterophase fluctuations are represented by the non-uniform stationary solutions of the nonlinear equations [131]. The stability of localized solutions and domain growth will be studied with the Landau-Ginzburg model.

In a solid solution, the system has the higher free energy than the host crystal and a significant contribution is from the elastic free energy. Microscopically, the elastic free energy has two parts: (i) the chemical contribution is depending on the configuration degrees of freedom, corresponding to a particular assignment of atoms to sites of the ideal lattice; (ii) the relaxation energy is due to the shifting of the atoms to their equilibrium positions by atomic size effect, which relies on the configuration and the displacive degrees of freedom. Static displacement of the atom at some site is defined as the difference between the actual position of the atom and the corresponding position of the mean crystal lattice site, described by the homogeneous strain.

First order phase transition is possible in one-dimensional systems with long-range interaction and disorder [69--73]. One-dimensional melting has been analytically and numerically studied as first-order phase transition in the discrete systems with long-range

interaction [91--98], and the crystalline, liquid, and gas phase are defined based on the density difference. In the following work, we will focus on melting in one-dimensional disordered systems with long-range interaction. In our model, the elastic degree of freedom will act as a long-range part that only the compressive behavior is considered in one dimension, and the competition between nonlinearity and disorder will determine the processes. As a possible microscopic picture of heterophase fluctuation, thermal energy localization induced by nonlinearity is dominant at high temperature melting and disorder through by the impurity atoms could have some important influence during the process. At low temperature, the elastic interaction induced by compositional disorder and size effect of the impurity atoms is necessary for the non-thermal energy localization.

3.5 Landau-Ginzburg Free Energy: Stationary Solution in One Dimension

In real metallic glasses, there are local atomic structures on different length scale: short-range order over several nearest neighbor distances and medium-range order over nanometer scale. A certain level of chemical disorder, coupling to position disorder, is necessary to build a topological disorder structure, i.e. to form amorphous phase [148], in two and three dimension systems. In one-dimensional model, melting is first order phase transition from an order state to a disordered state [149, 150]. For inhomogeneous system, Landau-Ginzburg theory is used to take into account the spatial fluctuations. We choose the root mean square of atomic displacement as the primary order parameter, and coefficients of the nonlinear Landau potential are determined by temperature and composition, which represent the influence of the thermal disorder and the chemical

disorder on a length scale (correlation length). The elastic degree freedom is considered as the long-range interaction and a macroscopic modulation of chemical disorder and atomic size effect.

3.5.1 Rescale

Under mechanical equilibrium condition (unstressed), the renormalized Landau-Ginzburg free energy density is:

$$f(M(x)) = \tilde{A}(T, X) \cdot M(x)^2 - C(X) \cdot M(x)^4 + E \cdot M(x)^6 + G_0 (\nabla M(x))^2. \quad (3.1)$$

Rescaling the free energy with $M = \left(\frac{|C(X)|}{E} \right)^{1/2} \eta$, $F_0 = \frac{|C(X)|^3}{E^2}$, we obtain the dimensionless form of the Landau-Ginzburg free energy density as

$$\bar{f} = \frac{f}{F_0} = a \cdot \eta^2 - \eta^4 + \eta^6 + \left(\frac{\partial \eta}{\partial y} \right)^2 \quad (3.2)$$

with $a = \frac{\tilde{A}(T, X)E}{|C(X)|^2}$, $q = \left(\frac{E}{|C(X)|} \right)^{1/2}$, and the rescaled space coordinate $y = \frac{|C(X)|}{\sqrt{G_0 E}} x$.

The total free energy is

$$F = \int \bar{f} dy \quad (3.3)$$

The evolution equation is

$$\frac{\partial \eta}{\partial t} = -\frac{\partial \bar{f}(\eta)}{\partial \eta} + 2 \frac{\partial^2 \eta}{\partial y^2} \quad (3.4)$$

with the rescaled time $t = \Gamma_0 \tau$. Γ_0 is the Landau-Khalatnikov coefficient that is related to the relaxation process and depends on the temperature and composition.

3.5.2 Uniform Solutions and Linear Stability Analysis

For uniform solutions, the gradient term disappears and we have:

$$2\eta - 4\eta^3 + 6\eta^5 = 0.$$

We get

$$\bar{\eta}_1 = 0 \tag{3.5}$$

$$\bar{\eta}_2 = \pm \sqrt{\frac{1 - \sqrt{1 - 3a}}{3}} \tag{3.6}$$

$$\bar{\eta}_3 = \pm \sqrt{\frac{1 + \sqrt{1 - 3a}}{3}}. \tag{3.7}$$

We add small perturbation to do the linear stability analysis:

$$\eta(y, t) = \bar{\eta} + \delta\eta \cdot \exp(\Gamma \cdot t) \cdot \exp(i \cdot k \cdot y). \tag{3.8}$$

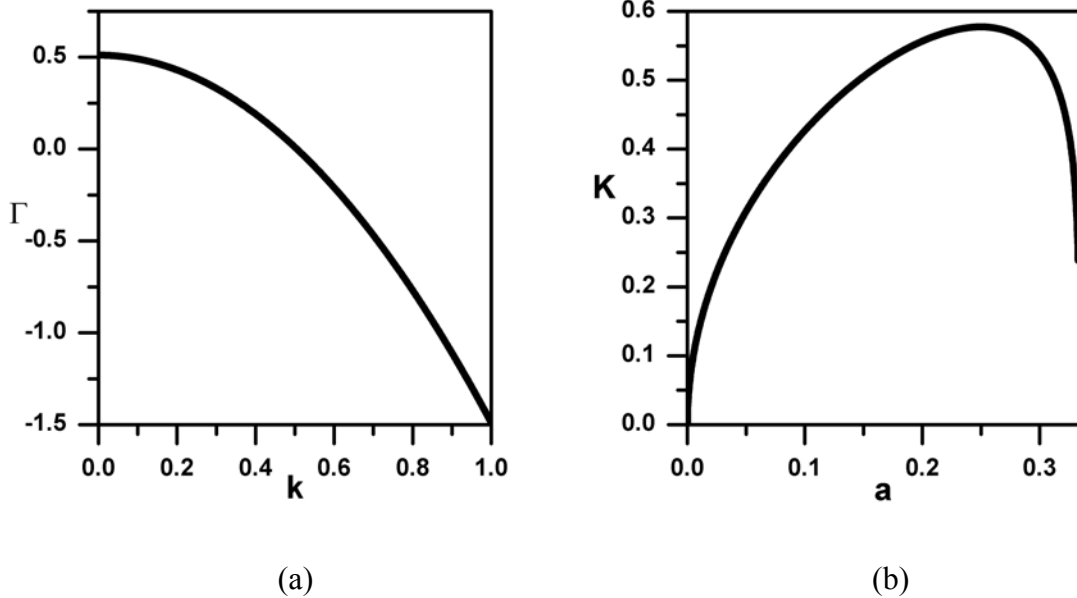


Figure 3.15 (a) The growth rate of the uniform solution $\bar{\eta}_2$ for $a=0.150$; (b) The cut-off wave vector of the uniform solution $\bar{\eta}_2$.

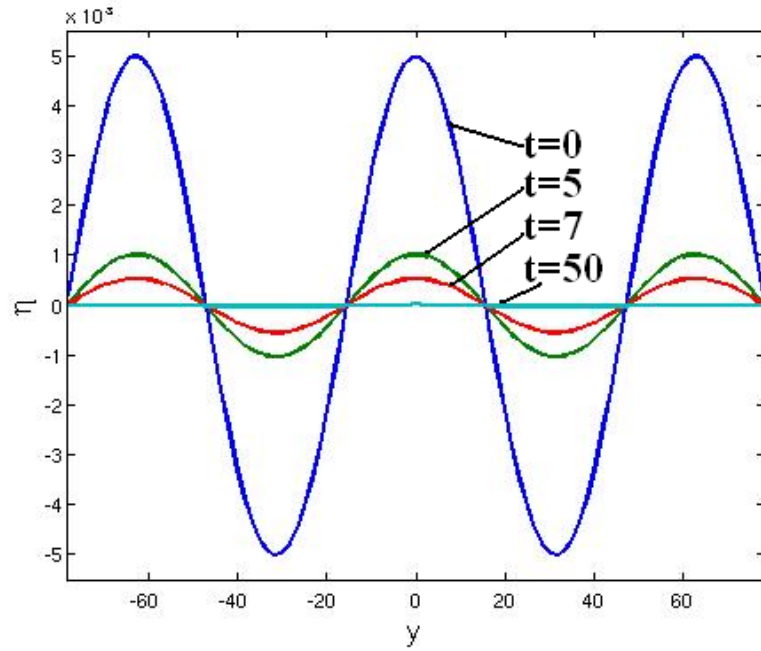
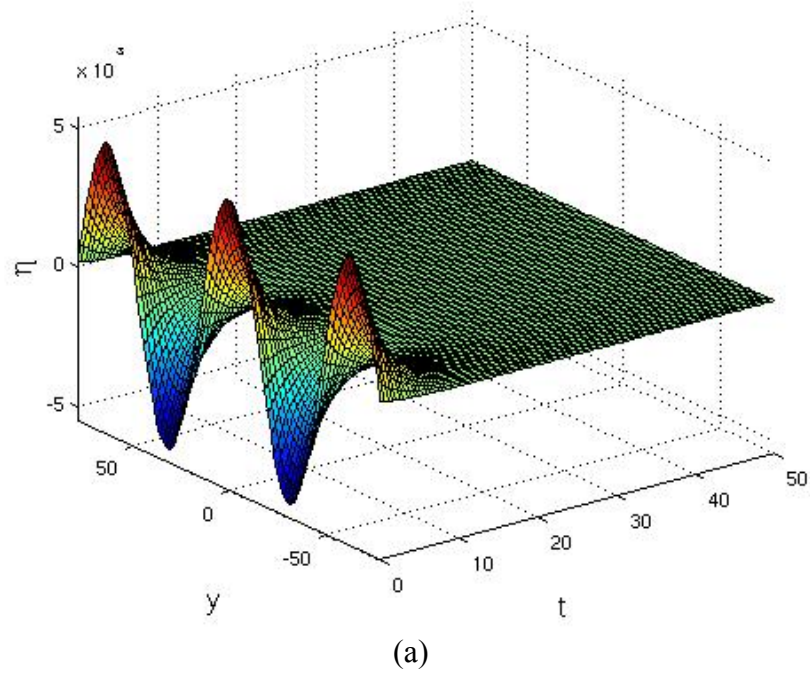


Figure 3.16 Evolution of small perturbation around the uniform solution $\bar{\eta}_1$ (a) in time-space coordinates and (b) space distribution of order parameter profiles with $t=0, 5, 7, 50$ for $L=156.232$, $\delta=0.005$, $a=0.150$.

Keeping the lowest order, we obtain the growth rate (Figure 3.15(a)):

$$\Gamma(k) = -(2 \cdot a - 12 \cdot \bar{\eta}^2 + 30 \cdot \bar{\eta}^4) - 2 \cdot k^2. \quad (3.9)$$

We could see the two solutions $\bar{\eta}_1$ and $\bar{\eta}_3$ are stable. There is a cut-off wave-vector K , which determines the stability limit for uniform solution $\bar{\eta}_2$ (Figure 3.15(b)).

$$K = 2 \sqrt{\frac{2}{3g}} \cdot \sqrt{\sqrt{1-3 \cdot a} \cdot (1 - \sqrt{1-3 \cdot a})} \quad (3.10)$$

The uniform solutions describe the macroscopic states of the systems. Small perturbation around the stable state will decay. An example of homophase fluctuation is shown in Figure 3.16. We use the initial condition

$$\eta(y,0) = \bar{\eta}_1 + \delta \cdot \cos(k \cdot y)$$

with $\delta = 0.005$, $k = 0.100$.

3.5.3 Non-uniform Solution and Stability Analysis

The non-uniform steady solutions are described by

$$2a\eta - 4\eta^3 + 6\eta^5 = 2 \frac{d^2\eta}{dy^2} \quad (3.11)$$

i.e.

$$2 \frac{d^2\eta}{dy^2} = -\frac{dV(\eta)}{dy} \quad (3.12)$$

$$V(\eta) = -a \cdot \eta^2 + \eta^4 - \eta^6 \quad (3.13)$$

which describes a particle's motion in the potential well $V(\eta)$ with mass $m = 2$. The first integral of motion of Eq. (3.12) is

$$\left(\frac{d\eta}{dy}\right)^2 + V(\eta) = U_0 = \text{Const} \quad (3.14)$$

$$\frac{d\eta}{dy} = \pm(U_0 - V(\eta))^{1/2} \quad (3.15)$$

and analogous to mechanical energy conservation. The various possible phase trajectories could be obtained in phase space by Eq. (3.15). For one kind of non-uniform stationary solutions, the following boundary condition is used:

$$\left.\frac{d\eta}{dy}\right|_{y=-l} = \left.\frac{d\eta}{dy}\right|_{y=l} = 0 \quad (3.16)$$

$$\bar{f}(y = -l) = \bar{f}(y = l) = \bar{f}_0 \quad (3.17)$$

$$\pm(y - y_0) = \int \frac{d\eta}{\sqrt{a \cdot \eta^2 - \eta^4 + \eta^6 - \bar{f}_0}} \quad (3.18)$$

For the case $\bar{f}_0 = 0$, the solution is

$$\eta(y) = \frac{\eta_2}{\sqrt{1 + \left(1 - \frac{\eta_2^2}{\eta_3^2}\right) \cdot \sinh^2[\sqrt{a} \cdot (y - y_0)]}} \quad (3.19)$$

with $\bar{f}(\eta) = \eta^2 \cdot (\eta^2 - \eta_2^2) \cdot (\eta^2 - \eta_3^2)$. An alternative form of Eq. (3.19) is

$$\eta(y) = \frac{\sqrt{6\bar{\eta}_2\bar{\eta}_3}}{\sqrt{1 + \left(1 - 12\bar{\eta}_2^2\bar{\eta}_3^2\right)^{1/2} \cdot \cosh[2\sqrt{a} \cdot (y - y_0)]}}. \quad (3.20)$$

We could rewrite Eq. (3.11) with $X = \eta$ as two first order ordinary differential equations:

$$\frac{dX}{dy} = Y$$

$$\frac{dY}{dy} = aX - 2X^3 + 3X^5.$$

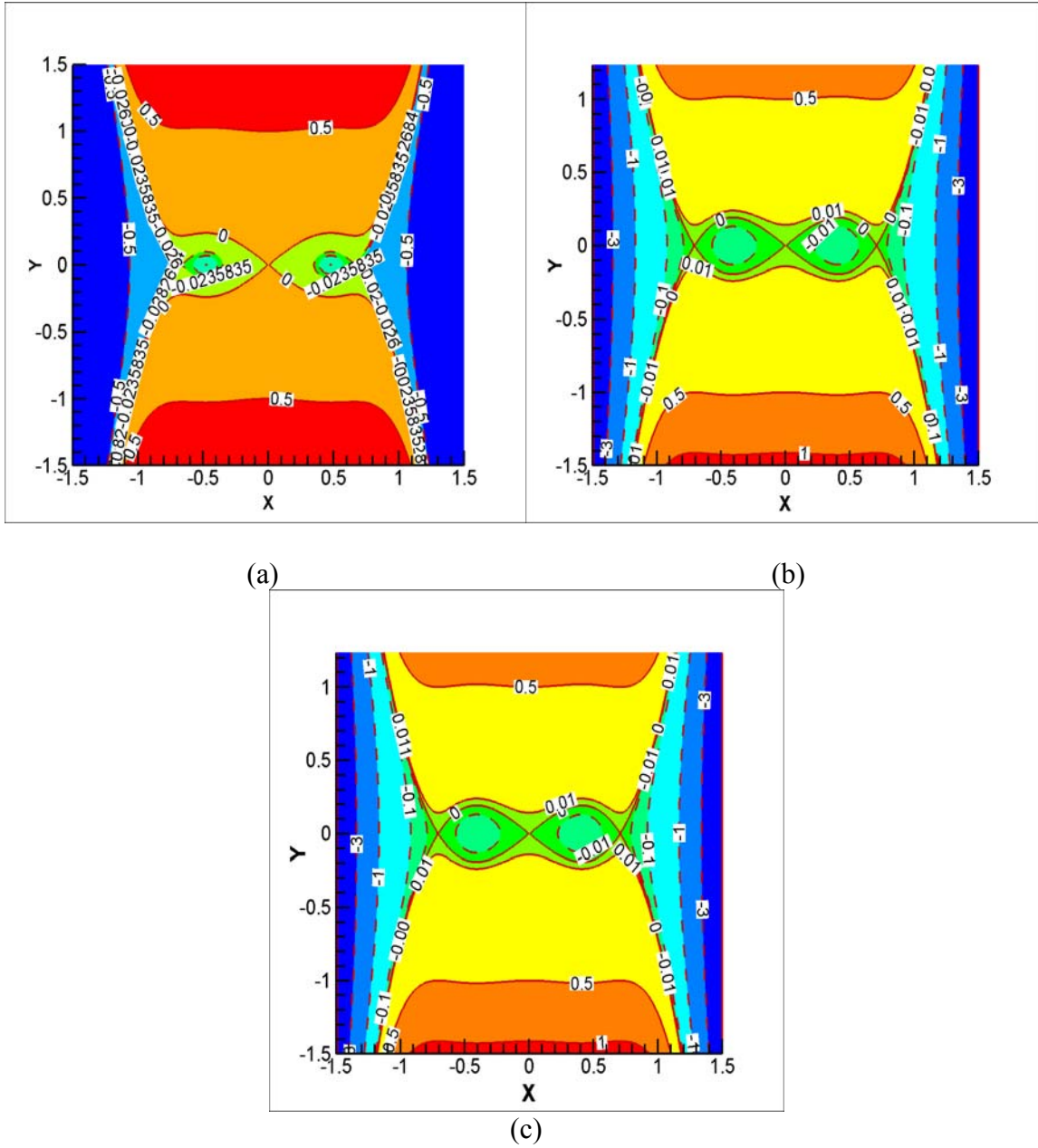


Figure 3.17 Phase portrait for (a) $a=0.300$, (b) $a=0.250$ and (c) $a=0.150$, where X represents the order parameter and Y is the ‘velocity’.

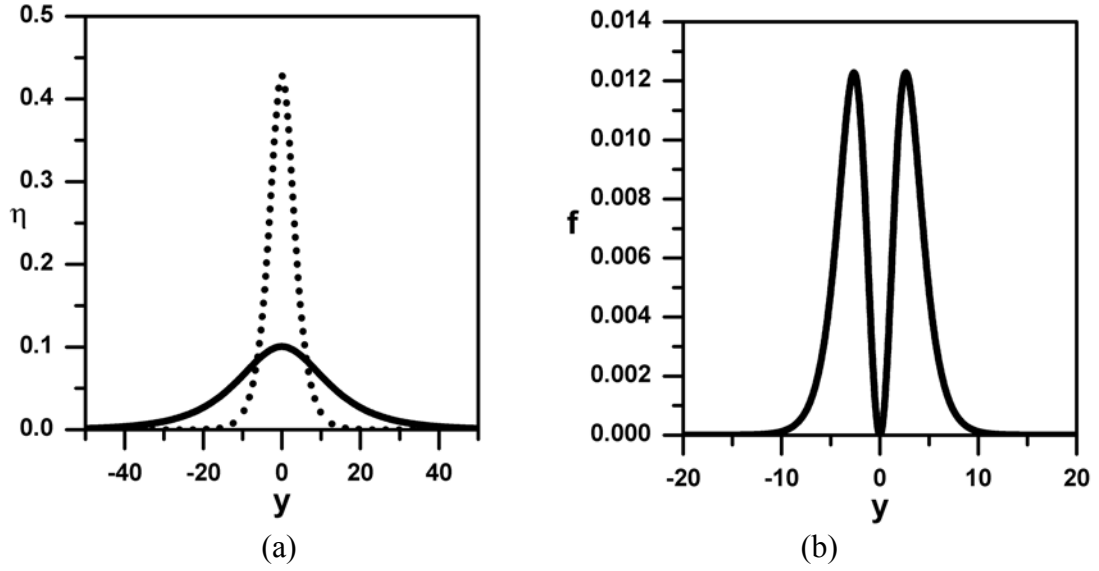


Figure 3.18 (a) Two non-uniform solutions for $a=0.010$ (solid line) and $a=0.150$ (dot line); (b) free energy dependence on the space coordinate for the non-uniform solution with $a=0.150$.

From the phase plane analysis, we have two saddle points $\bar{\eta}_1$, $\bar{\eta}_3$ and one center point $\bar{\eta}_2$ for $0 < a < \frac{1}{3}$. Close curves around $\bar{\eta}_2$ are periodic solutions, and there is a bounded non-uniform solution for $\bar{\eta}_3$ in physical space. The solution of Eq. (3.19) is along the characteristic $f_0 = 0$ in Figure 3.17(c). And there are two non-uniform solutions connecting two roots of $\bar{\eta}_3$ that separate the periodic solutions around $\bar{\eta}_1$, $\bar{\eta}_2$ and the unbounded states. To characterize the relative stability of the two stable uniform solutions, we define the supersaturation [151] as:

$$\Omega = \int_{\bar{\eta}_1}^{\bar{\eta}_3} Df(\eta) d\eta = \left(\frac{1}{3} - 2\bar{\eta}_2^2 \right) \left(\frac{2}{3} - \bar{\eta}_2^2 \right)^2 \quad (3.21)$$

with $Df(\eta) = -(2a\eta - 4\eta^3 + 6\eta^5)$. For $a < 0.250$, the state $\bar{\eta}_3$ is globally stable since $\Omega > 0$.

We rewrite the solution Eq. (3.19) as:

$$\eta(y) = \frac{\sqrt{\bar{\eta}_2^2(4 - 6\bar{\eta}_2^2)}}{\sqrt{1 + \left(1 - \bar{\eta}_2^2(8 - 12\bar{\eta}_2^2)\right)^{1/2} \cdot \cosh[2\sqrt{a} \cdot (y - y_0)]}}. \quad (3.22)$$

We set the maximum value of Eq. (3.22) at $y_0 = 0$ (Figure 3.18):

$$\eta_M(\bar{\eta}_2^2) = \frac{\sqrt{\bar{\eta}_2^2(4 - 6\bar{\eta}_2^2)}}{\sqrt{1 + \left(1 - \bar{\eta}_2^2(8 - 12\bar{\eta}_2^2)\right)^{1/2}}}. \quad (3.23)$$

We define the width R of domain as:

$$\eta(R) = \bar{\eta}_2$$

with $y_0 = 0$ and $\bar{\eta}_2 = \sqrt{\frac{1 - \sqrt{1 - 3a}}{3}}$. For large supersaturation, which is closing to the

critical point, the domain width is large but with low maximum value (Figure 3.19).

When closing to the transition point, we have small saturation with large width and large maximum value. The minimum domain width is around $R_{\min} = 2.732$. Substituting Eq.

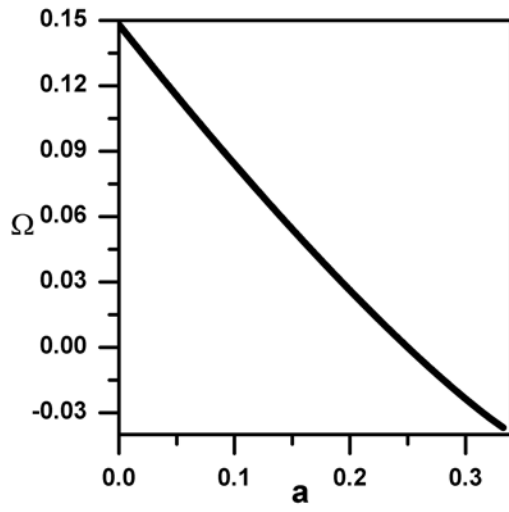
(3.19) into Eq. (3.3), we have the free energy of the non-uniform solution

$$F = \int \left(2 \left(\frac{d\eta(y)}{dy} \right)^2 - U_0 \right) dy \quad (3.24)$$

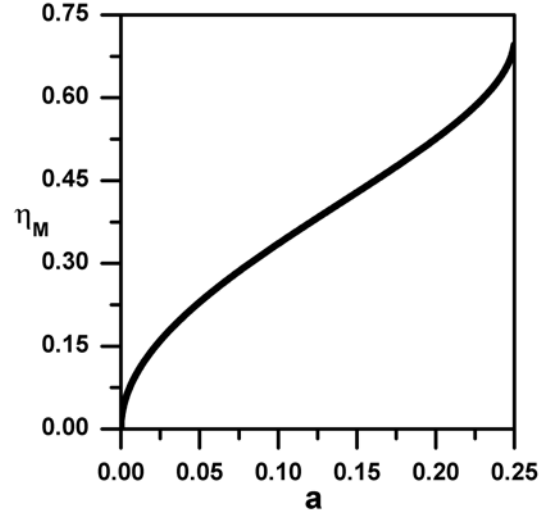
The excess free energy of the non-uniform solution is defined as [140]

$$\Delta F = F - \bar{F} = \int \left(2 \left(\frac{d\eta(y)}{dy} \right)^2 - U_0 - f(\bar{\eta}) \right) dy \quad (3.25)$$

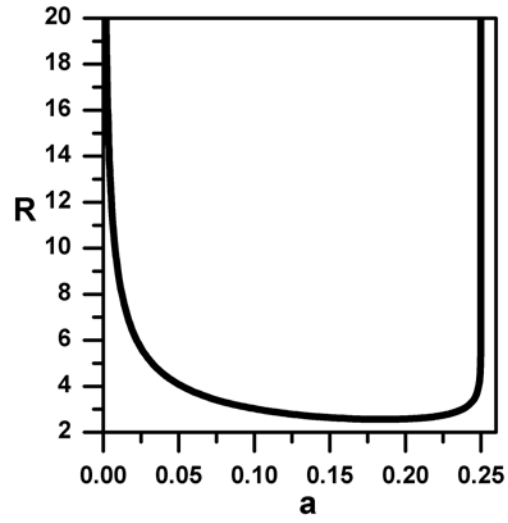
where \bar{F} is the free energy of the uniform state $\bar{\eta}$ (Figure 3.20).



(a)



(b)



(c)

Figure 3.19 (a) Supersaturation as a function of parameter a ; (b) The maximum value of the non-uniform solution of Eq. (3.23) as a function of parameter a ; (c) The domain width of the non-uniform solution of Eq. (3.19) as a function of parameter a .

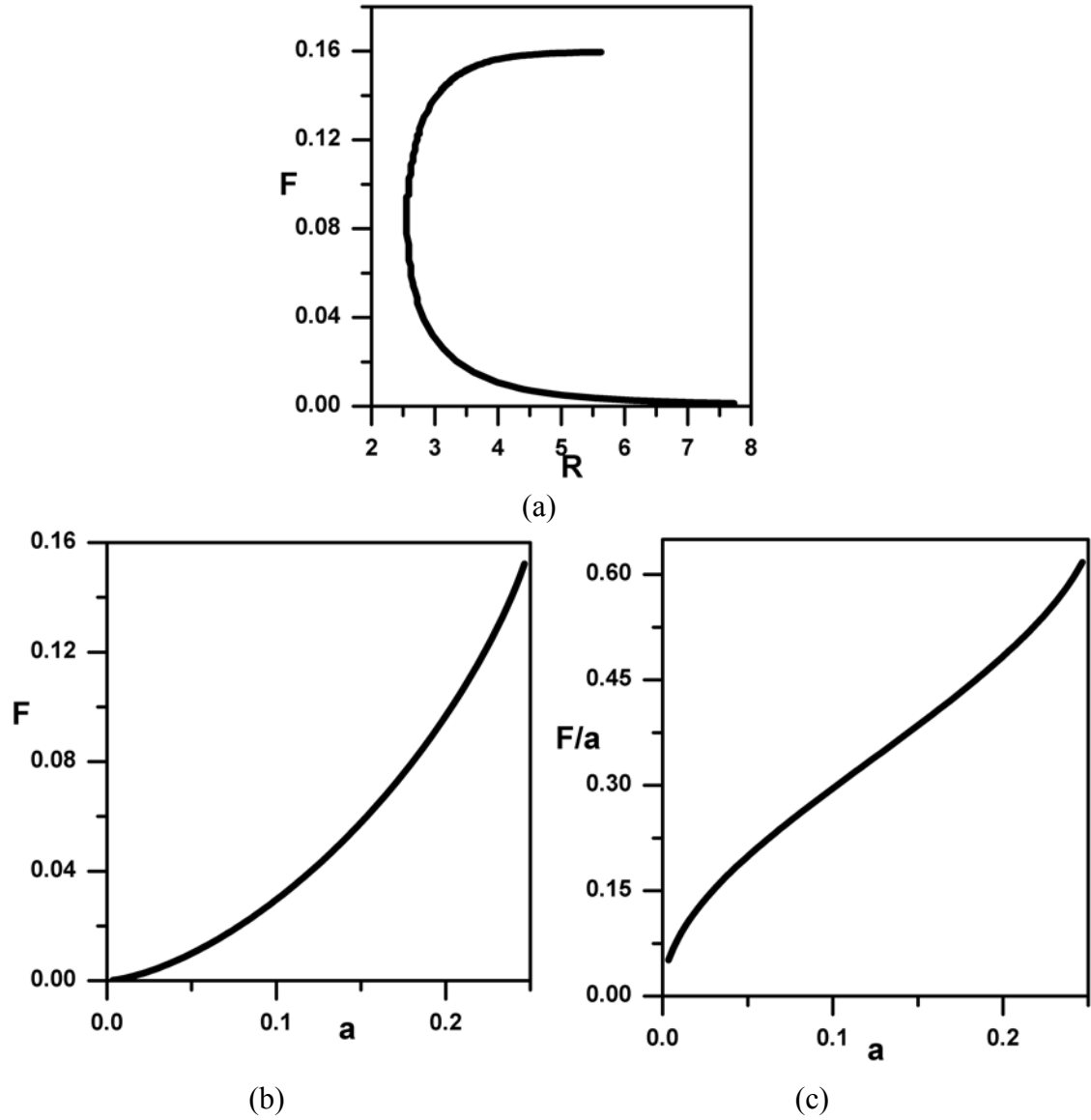


Figure 3.20 Free energy of critical nucleus as a function of (a) the domain width and (b) the normalized quadratic coefficient a ; (c) Ratio F/a over coefficient a .

Table 3 Eigenvalues for $a=0.150$

Index	Eigenvalue for $a=0.150$
1	-0.584
2	0.0
3	0.299

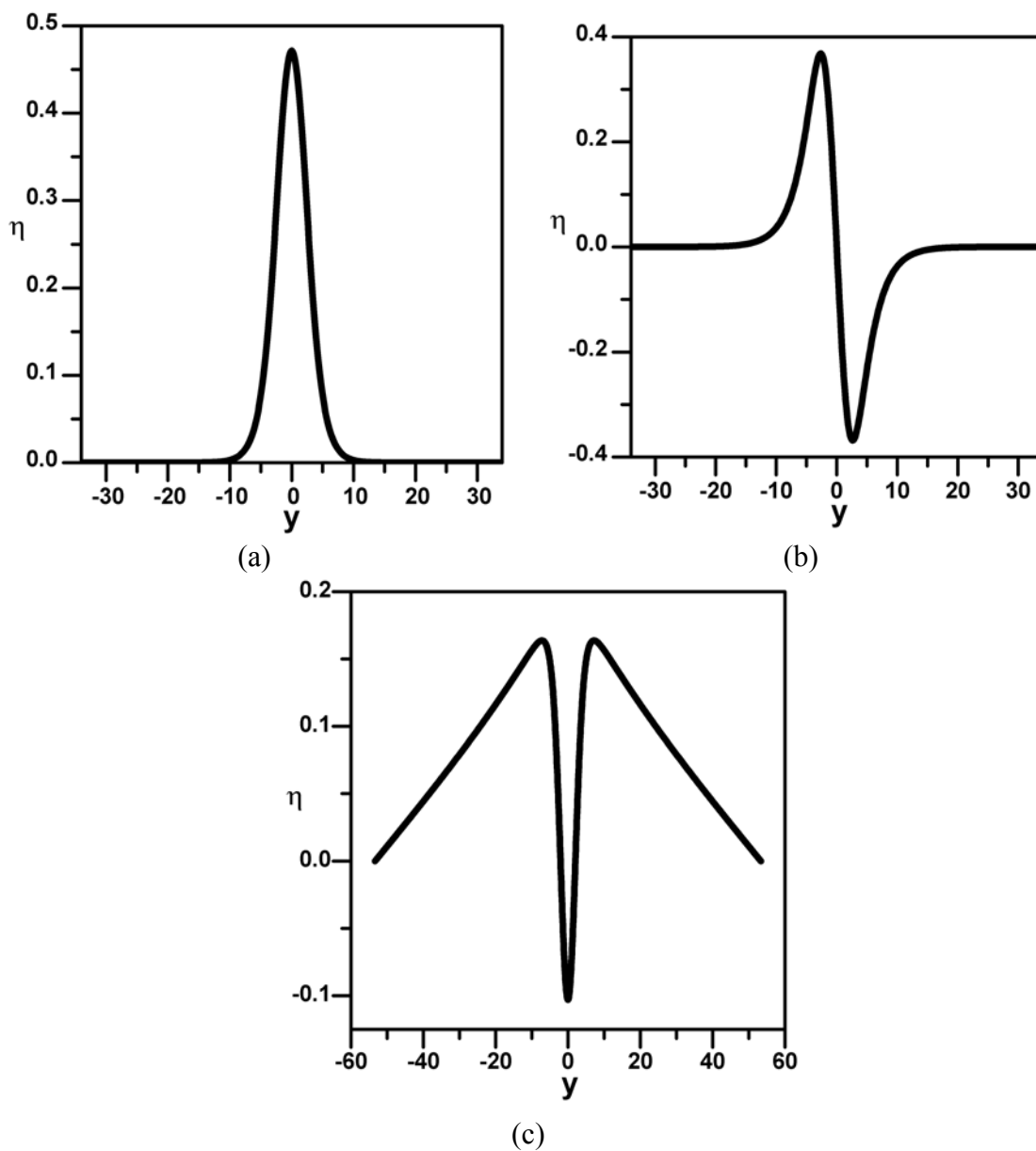


Figure 3.21 Eigenfunctions for the eigenvalues (a) $\lambda = -0.584$, (b) $\lambda = 0$, and (c) $\lambda = 0.299$ with $a = 0.150$.

To do the linear stability analysis, we need to solve the eigenvalue problem

$$L(\eta_s(y))\delta\eta(y) = \lambda\delta\eta(y) \quad (3.26)$$

where the linear operator has the following form:

$$L(\eta_s(y)) = \frac{\partial^2 \bar{f}(\eta)}{\partial \eta^2} \bigg|_{\eta_s(y)} - 2 \frac{d^2 \eta_s(y)}{dy^2}. \quad (3.27)$$

And the perturbation is

$$\eta(y) = \eta_s(y) + \delta\eta(y)\exp(-\lambda\tau). \quad (3.28)$$

The Goldstone mode

$$\delta\eta(y) = \frac{d\eta_s(y)}{dy} \quad (3.29)$$

is obvious with eigenvalue $\lambda = 0$. The discrete eigenvalues for $a = 0.150$ are listed in the Table .1. And the corresponding eigenfunctions are also shown in Figure 3.21. The spectrum is obtained numerically (Figure 3.22).

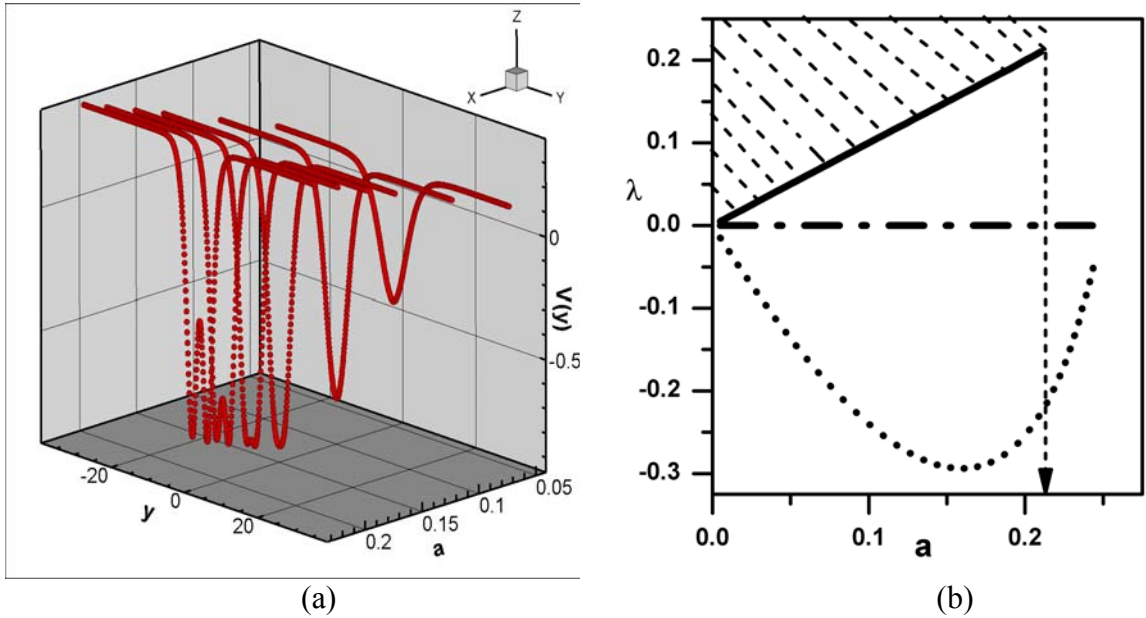


Figure 3.22 (a) Potential Function for $a=0.050, 0.10, 0.150, 0.175, 0.200$; (b) Spectrum of Eq. (3.26): the shaded area is the corresponding continuous spectrum and the dot line, dash dot line and solid line represent the discrete spectrum.

3.6 Homogeneous Nucleation in One Dimension: Numerical Results

As shown in Figure 3.16, homophase fluctuations are small amplitude fluctuations around the initial phase and do not change the symmetry, which represent the elementary excitations that exist in the initial thermodynamic phase and could be described by a single plane wave function or superposition of them with finite numbers. Homophase fluctuations are in the framework of equilibrium statistical physics.

In Figure 3.23 , the initial condition

$$\eta(y,0)=|\overline{\eta}_2|+\delta\cdot\cos\left(\chi\cdot\frac{2\pi}{L}\cdot y\right) \quad (3.30)$$

is used, where $\chi = 2.534$, $\delta = 0.005$ are chosen to make $k = 0.100$ (the cut-off $K = 0.141$). The pictures in Figure 3.23 are only possible mathematically and we could still call it as a homophase fluctuation since it is small amplitude around the unstable equilibrium state.

As a term, ‘heterophase fluctuation’ is first used by Frenkel [147] and was referred to macroscopic small nuclei of the final phase B dissolved in the solvent----the initial phase A in the vicinity of the corresponding transition points. Comparing to the dynamic character of homophase fluctuations, local equilibrium could be obtained for mesoscopic heterophase fluctuations under quasistatic condition

$$\tau_{\text{loca}} < \tau_{\text{life}} < \tau_{\text{obs}}$$

that the characteristic life time scale τ_{life} of heterophase fluctuations is larger than the local relaxation time scale τ_{loca} and τ_{obs} is the observation time scale. The appearing and dissolution of those fluctuations are typical dynamical. As localized large-energy fluctuations, heterophase fluctuations are nonergodic and are associated with the

nonlinear degree of freedoms. Based on the nonequilibrium and inhomogeneous nature, the heterophase fluctuations could be induced by the intrinsic properties, strong external source and stochastic perturbation [152]. Based on statistical theory of heterophase fluctuations, Yukalov studied melting, crystallization and glass-to-liquid transitions for pure elements and phase probabilities were obtained [131, 153, 154, 155].

Since the homophase fluctuations are defined as phonons in crystals, what is the possible microscopic origin of heterophase fluctuations in binary alloys [156]? Nonlinear energy localization phenomena have drawn so much attention in nonlinear lattice modes. It has been long recognized that localized vibrational modes could be induced by impurities in linear lattices. Since 1980s, theoretically the presence of nonlinearity, by coupling or onsite potentials, can also lead to localized vibrational modes, called ‘intrinsic localized modes’. Also in nonlinear lattices, the impurities may lead to energy trapping and localization around the impurities sites. Large spatial extent of localization may be obtained by the fusion of solitons. Even at low temperature, potential energy localization could be induced at the impurity sites by long-range interaction in lattice models [130]. Recently, nonlinear energy localization mechanism has been proposed to be responsible for the DNA denaturation as a one-dimensional nonlinear model. In more realistic models, solitons are unstable and soliton-like excitation and interaction of those excitations could be responsible for the nonlinear energy localization. For polymorphic melting in binary alloys, nonlinearity and disorder govern the whole process either at high temperature or low temperature. At low temperature, composition modulation may initiate the small amplitude localization with small amount of impurity atoms and

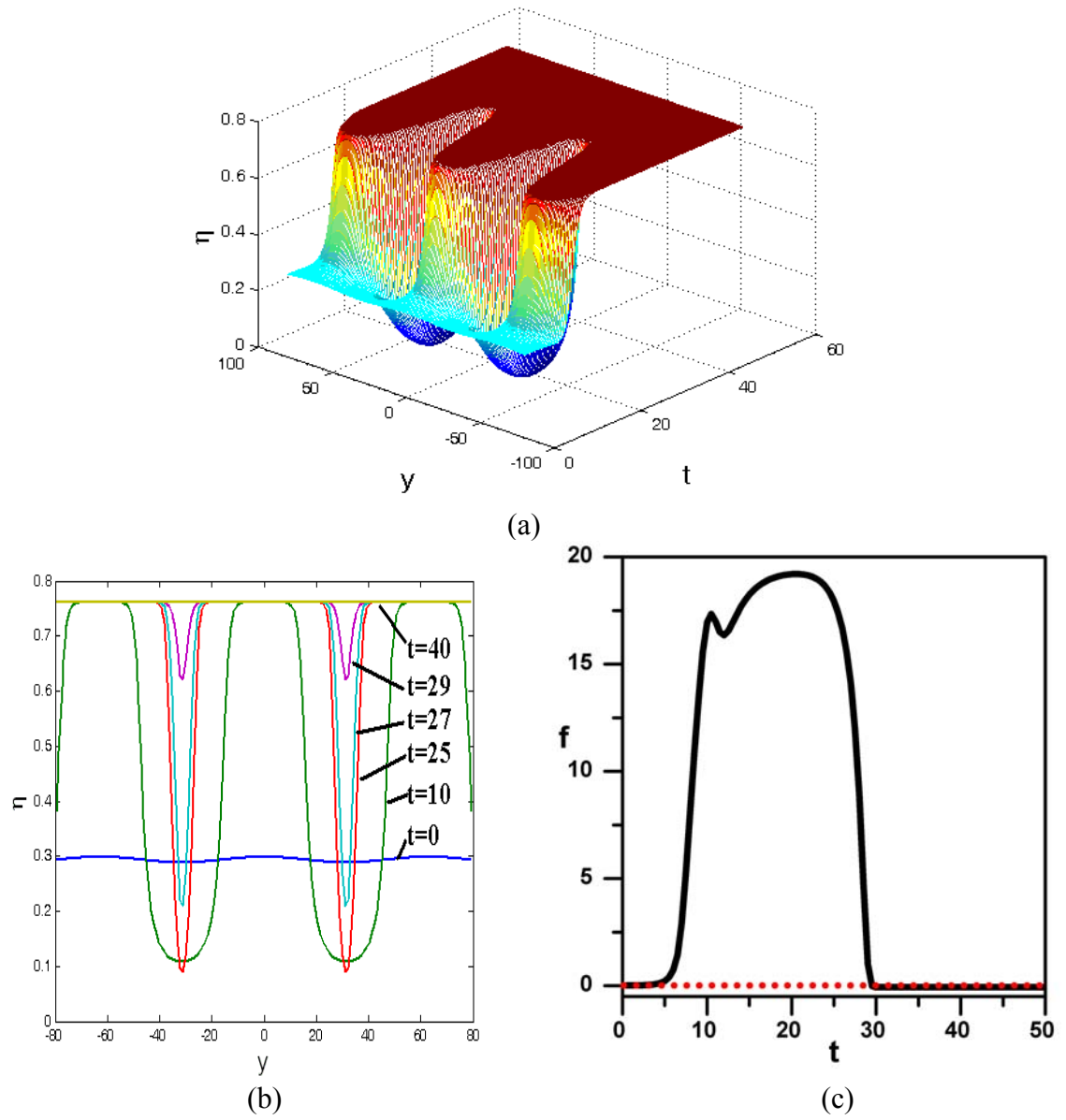


Figure 3.23 Growth of a new phase region with $a=0.150$, $L=159.234$: (a) evolution of order parameter values with time and space coordinates; (b) spatial distribution of order parameter profiles for different time; (c) free energy density as a function of time.

structure fluctuations could subsequently happen with the increasing composition after the development of modulation instability, which induces the energy localization with large amplitude.

The time evolution of the heterophase nuclei in a metastable system is described by the nucleation and growth theory. Landau-Ginzburg approach has been used to describe the kinetics of diffusionless first-order phase transitions [146, 157]. The growth law is derived as $R \propto t$ for a 2-3-4 type of Landau potential for one, two and three dimensions by solitary wave asymptotical analysis [146] and the dissolution law is also discussed. The critical nuclei are obtained by solving the stationary solutions of time-dependent Landau-Ginzburg equation analytically (Eq. (3.22) and Eq. (3.23)). Based on the nonlinear stability analysis, small perturbations are added to study the time evolution of initial critical nuclei (Eq. (3.26), Table 3 and Figure 3.21). We add small perturbation from the eigenfunction of λ_2 :

$$\eta(y) = \eta_s(y) + \Delta \cdot \delta\eta(y) \quad (3.31)$$

with $\Delta = 0.005$. The system decay and finally go back to the uniform state $\bar{\eta}_1 = 0$, which is corresponding an example of dissolution of the initial critical nuclei in Figure 3.24. For goldstone mode, the nucleus has no change for small positive perturbation (Figure 3.25).

The growth law is studied for the unstable mode λ_1 with small perturbation $\Delta = -0.005$. Initially, the nucleus experiences a transient growth until the maximum order parameter over space turns into the corresponding bulk equilibrium value (Figure 3.26 (b)), and the free energy keeps increasing with time (Figure 3.27(b)). At the second stage, the front begins to propagate to both directions until it reaches out the size limit and the system is completely transformed into new phase with lower free energy (Figure 3.26(c), Figure

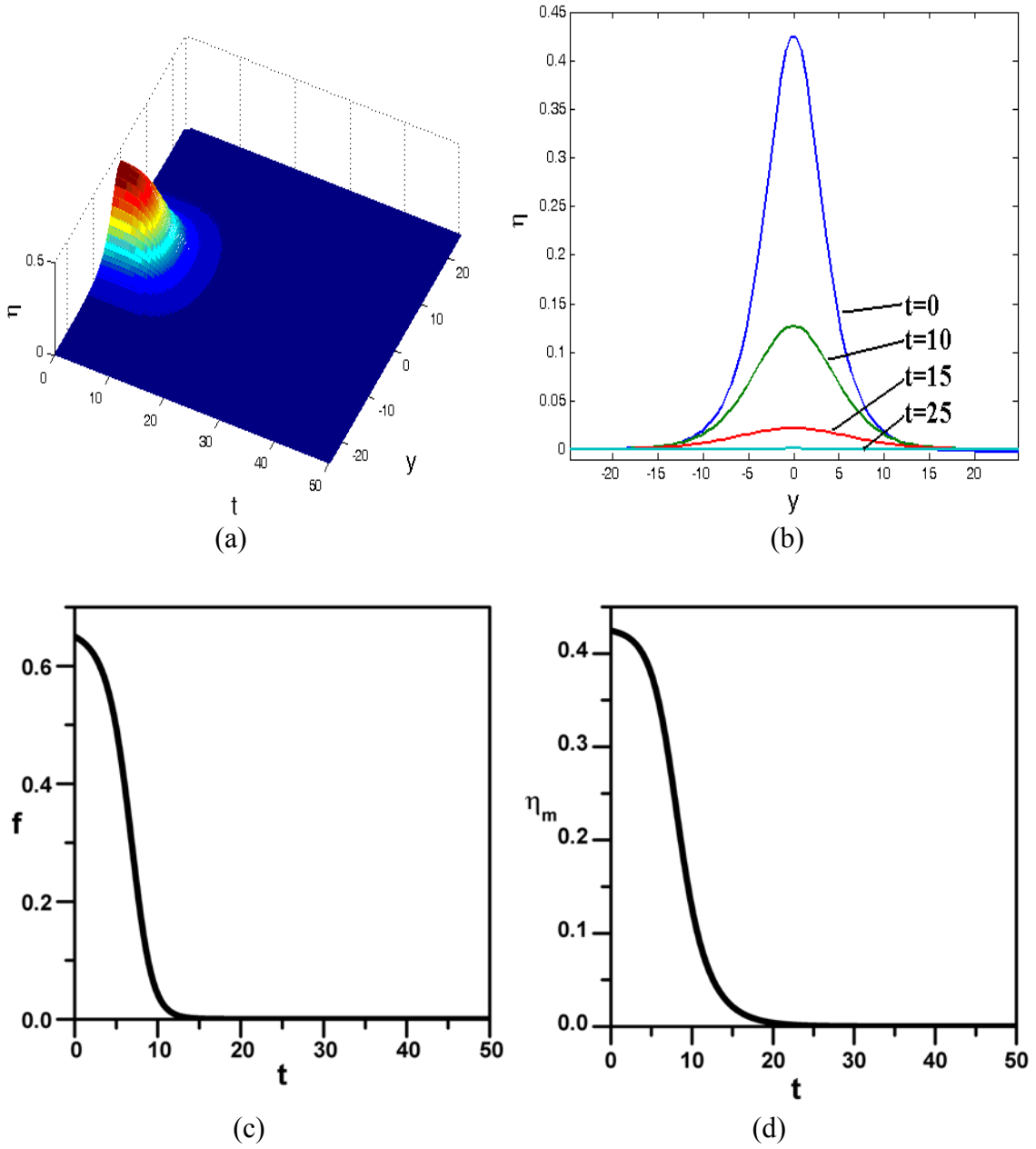


Figure 3.24 Decay of the system with the small perturbation: $L=49.405$, $\Delta=-0.005$: (a) evolution of order parameter values with time and space coordinates; (b) spatial distribution of order parameter for different time; (c) free energy density as a function of time; (d) maximum order parameter values as a function of time.

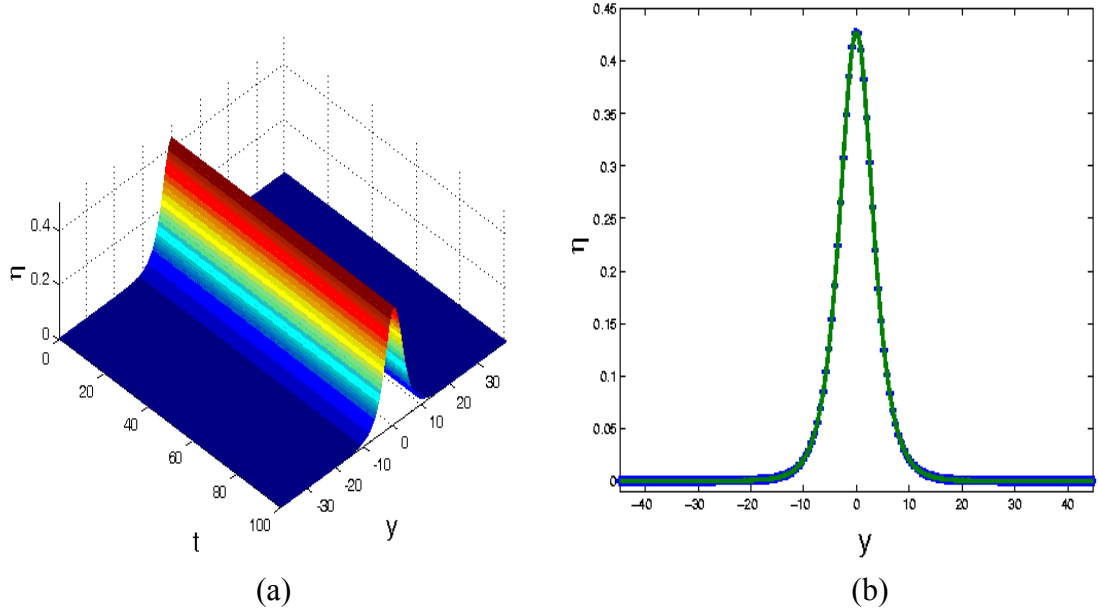


Figure 3.25 Small perturbation from the Goldstone mode with $L=89.443$, $\Delta=0.005$, $a=0.150$: (a) evolution of order parameter values with time and space coordinates; (b) spatial distribution of order parameter profiles for different time.

3.27(b)). The time evolution of domain width shows the linear growth rate of new phase after the initial transient state in Figure 3.28(a). We also define another linear dimension L_d , which is defined by the area between the spatial order parameter profiles and the space coordinates in Figure 3.26(c) divided by the maximum order parameter value, and the corresponding time evolution still show the same linear growth rate after the transient stage (Figure 3.28(b)).

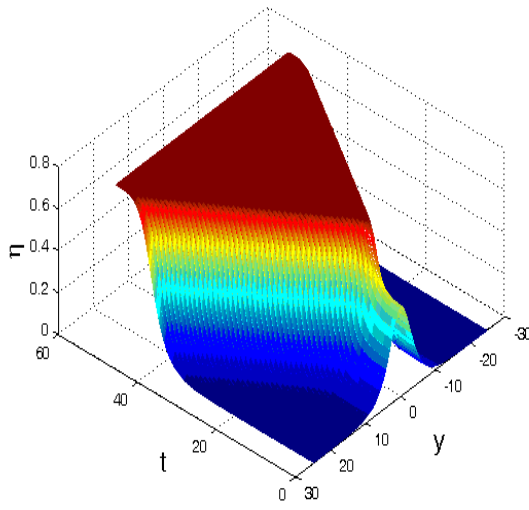
From the time evolution equation of Eq. (3.4), the time derivative and the space derivative are invariant under the general translation in time and space coordinates

$$t \rightarrow t + \Delta t, \quad y \rightarrow y + \Delta y \quad (3.32)$$

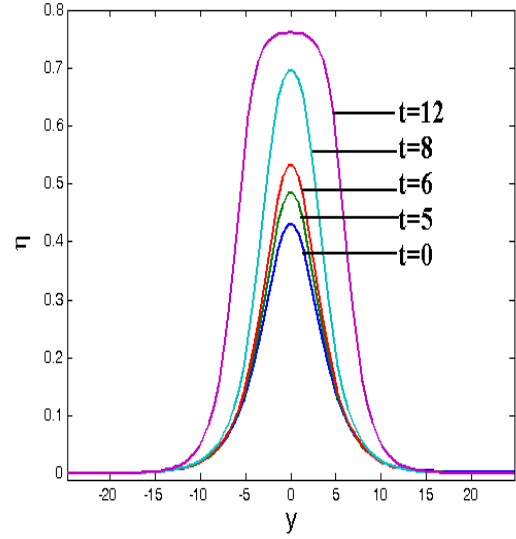
where Δt and Δy are arbitrary. Based the definition of domain width

$$\eta(R(t), t) = \bar{\eta}_2, \quad (3.33)$$

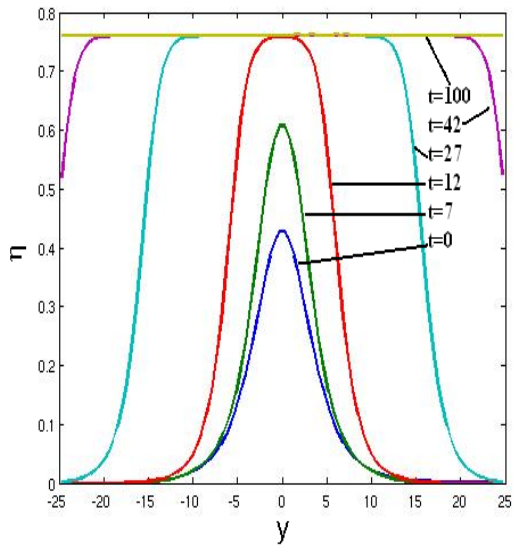
where $\bar{\eta}_2$ is the unstable uniform solution of Eq. (3.6) and we have



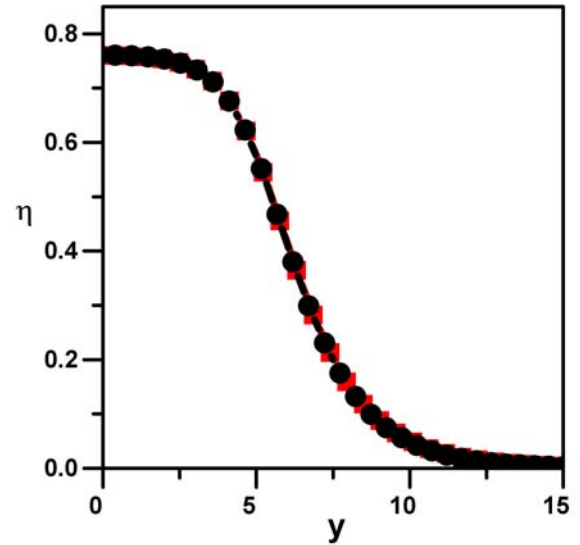
(a)



(b)



(c)



(d)

Figure 3.26 Growth of the system with the small perturbation: $L=49.405$, $\Delta=-0.005$: (a) order parameter profiles as a function time and space coordinates; (b) spatial distribution of order parameter for different time $t=0, 5, 6, 8, 12$; (c) order parameter values for $t=0, 7, 12, 27, 42, 100$; (d) overlapping solutions (propagation front) for $t=12$ (red square solid line) and $t=27$ (black circle line) which is shifted to the space at $t=12$.

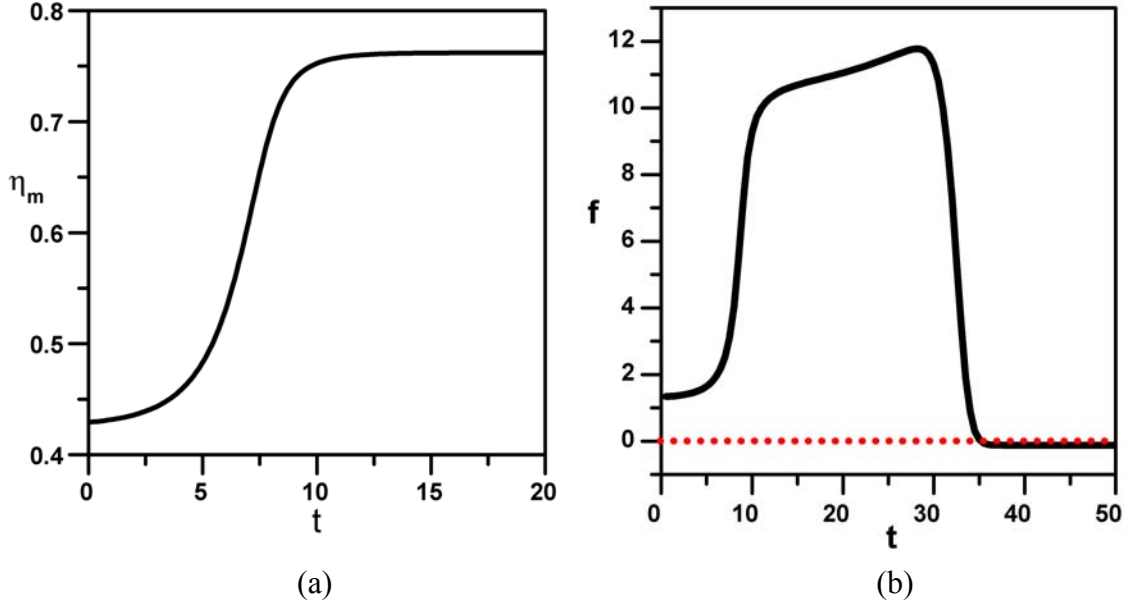


Figure 3.27 (a) Maximum order parameter value and (b) free energy density as a function of time ($a=0.150$, $L=49.405$, $\Delta=-0.005$).

$$\frac{\partial \eta}{\partial t} + \frac{\partial \eta}{\partial R} \cdot \frac{dR}{dt} = 0. \quad (3.34)$$

We redefine the space coordinate as

$$z = y - R(t), \quad (3.35)$$

and a particular solution could exist with the following form

$$\eta(y, t) = \eta(z(y, t)). \quad (3.36)$$

With this kind of solution, the evolution equation of Eq. (3.4) is transformed into

$$2 \frac{d^2 \eta}{dz^2} + \frac{dR}{dt} \cdot \frac{d\eta}{dz} - \frac{\partial \bar{f}(\eta)}{\partial \eta} = 0, \quad (3.37)$$

which suggests

$$\frac{dR}{dt} = v \quad (3.38)$$

and v is a constant [146].

Our numerical result shows our solution for Eq. (3.4) is the translation invariant with time and space. An example is shown in Figure 3.26(c) and the growth rate of domain width is $v=0.657$ from Figure 3.28(a).

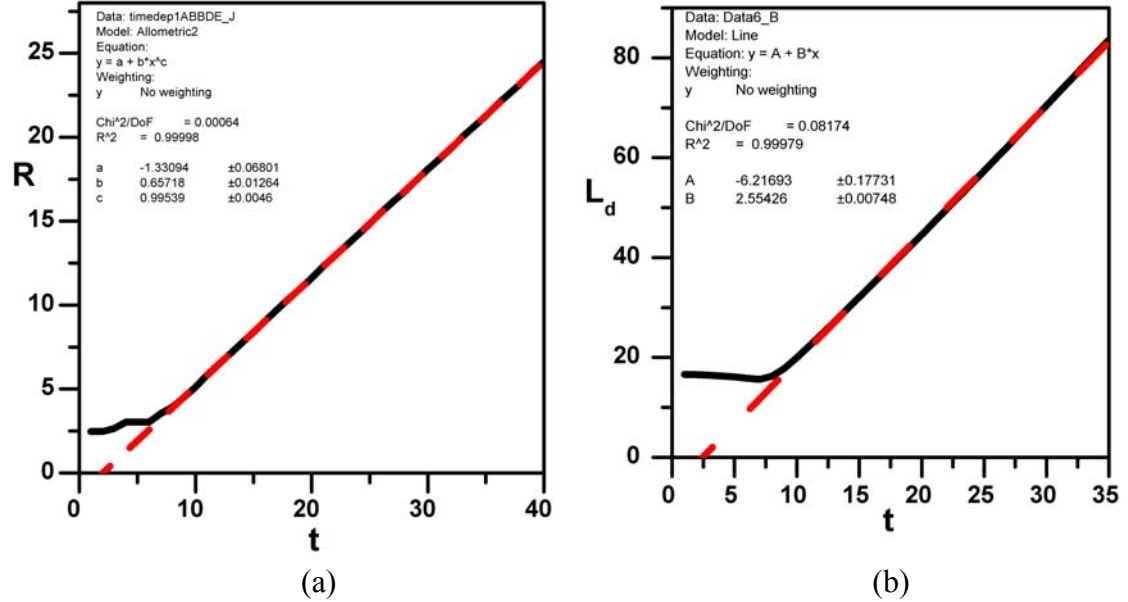


Figure 3.28 Domain width (a) and linear dimension (b) as a function of time. Red lines are fitting curves ($a=0.150$, $L=49.405$, $\Delta=-0.005$).

We consider the interaction of two identical nuclei with the same initial perturbation and a large enough separation distance. At the initial state, the top of both them begins to rise up until reaching the new phase, i.e. the corresponding bulk equilibrium value, and then the fronts propagate separately (Figure 3.29). At the second stage, the inside fronts meet at the center $y=0$ and then begin to reach the new phase until the valley disappear between two nuclei. After that, two nuclei turn into the bigger nucleus and the growth act the same as the previous single one though the rate of linear dimension is a nonlinear function of time.

One-dimensional melting in binary alloys is studied as a continuum model defined by a Landau-Ginzburg free energy. As inhomogeneous systems govern by nonlinearity and

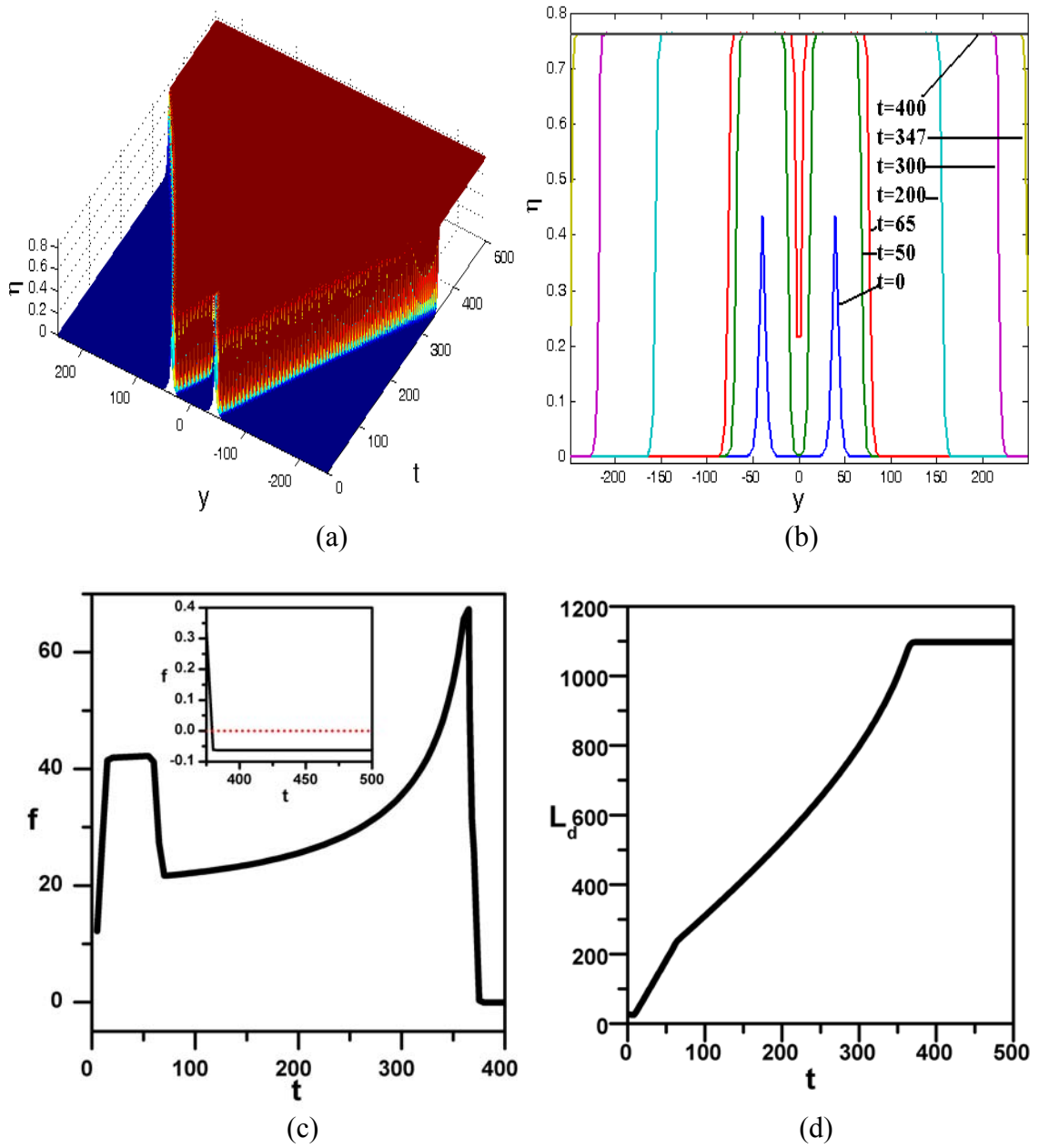


Figure 3.29 Collision of two identical nuclei with separation distance $L_s=40$, $a=0.150$, $\Delta=-0.005$, and $L=565.690$: (a) space-time evolution of order parameter values; (b) space distribution of order parameter profiles at different time values; (c) free energy density and (c) linear dimension as a function of time.

disorder, nonlinear energy localization mechanism is proposed to be responsible for the heterophase fluctuations. Nucleation and growth of domains are investigated based on the analytical solutions of the well-known nonlinear evolution equation defined by the 2-4-6 type of Landau free energy and numerical results are presented.

3.7 Homogeneous Nucleation in Two Dimension: Numerical Results

We will use our model of Eq. (3.4) to study the formation of a nucleus and the subsequent expansion of domains of new phases in two-dimensional systems. The nonlinear evolution equation is

$$\frac{\partial \eta}{\partial t} = -\frac{\partial \bar{f}(\eta)}{\partial \eta} + 2 \left(\frac{\partial^2 \eta}{\partial y^2} + \frac{\partial^2 \eta}{\partial x^2} \right). \quad (3.39)$$

Numerical solutions are obtained by solve the evolution equation with periodic boundary condition through Fourier Spectral methods and show how a large-scale fluctuation of order parameter initiates and turns the system from a metastable state to an absolutely new state. To investigate the dynamics of arbitrary mesoscopic inhomogeneities of the sytem, we consider two different initial perturbations, i.e. thermal fluctuations and soliton-like excitations.

For the thermal fluctuations, the initial condition has the following form

$$\eta(x, y, 0) = |\bar{\eta}_2| + \delta \cdot \left(\cos \left(\chi \cdot \frac{2\pi}{L} \cdot (y - y_0) \right) + \cos \left(\chi \cdot \frac{2\pi}{L} \cdot (x - x_0) \right) \right) \quad (3.40)$$

where $\bar{\eta}_2$ is the unstable equilibrium state Eq. (3.6) and we choose the location of (x_0, y_0) at the center of the systems. From our results in Figure 3.30, it is clearly show a nucleus starts from the center around $25 < t < 27$ with isotropic shape. Once the maximum order

parameter value reaches the new equilibrium profile, the front begins to propagate and finally reach the anisotropic shape (Figure 3.30(f)).

Based on the corresponding one-dimensional analytical solutions of the critical nuclei, we construct the initial spherical soliton-like perturbation

$$\eta(x, y, 0) = \delta \cdot \eta_s(r) \quad (3.41)$$

where $\eta_s(r)$ has the same mathematical form as the corresponding one-dimensional critical nucleus solution and

$$r = \sqrt{(x - x_0)^2 + (y - y_0)^2} \quad (3.42)$$

with the location of (x_0, y_0) at the center of the systems. A spherical nucleus initiates at the center around $17 < t < 19$ and the final shape still keeps the spherical shape after the expansion (Figure 3.32).

Why the final shapes of excitations are different, i.e. anisotropic or isotropic? The contour plots of initial state of the above two cases indicate that the final shape i.e. determined by the details of the initial perturbations (Figure 3.31(a), Figure 3.33 (a)). After the formation of a nucleus, the velocity of the front propagation is depend on the local curvature of initial order parameter fields, i.e. the higher the larger radius of local curvature. This result is different from Kuzovlev et al's results [158] that the final shape of excitation became isotropic with an anisotropic perturbation.

The final stable domain width of two nuclei shows different behavior with variation of the size of systems. We study the front propagation by tracing the moving location $\eta(y) = \bar{\eta} / 2$ along some fixed grid lines. The final stable domain width of nuclei initiated from thermal fluctuations increases with the increasing systems' size (Figure 3.42(a)). On

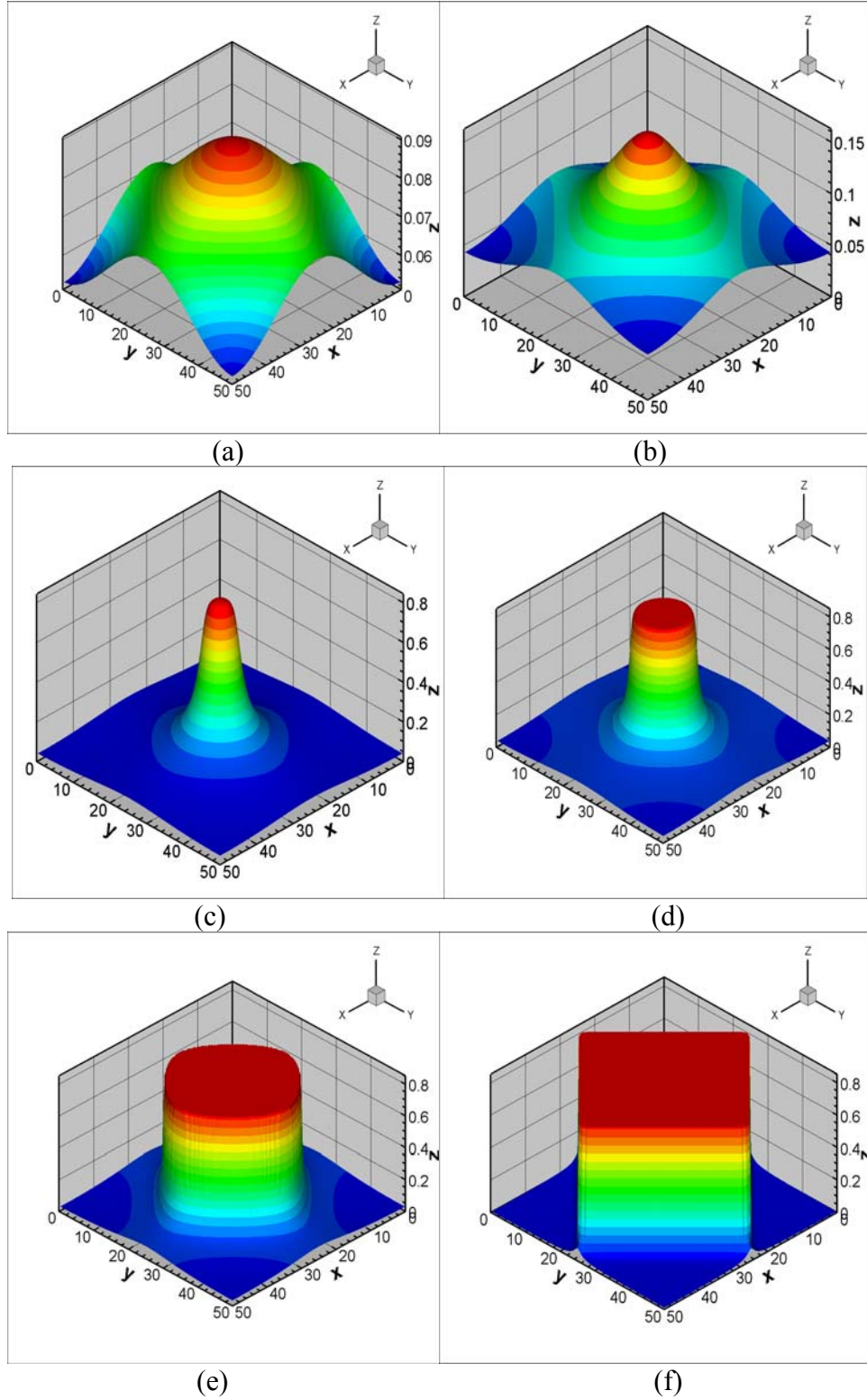
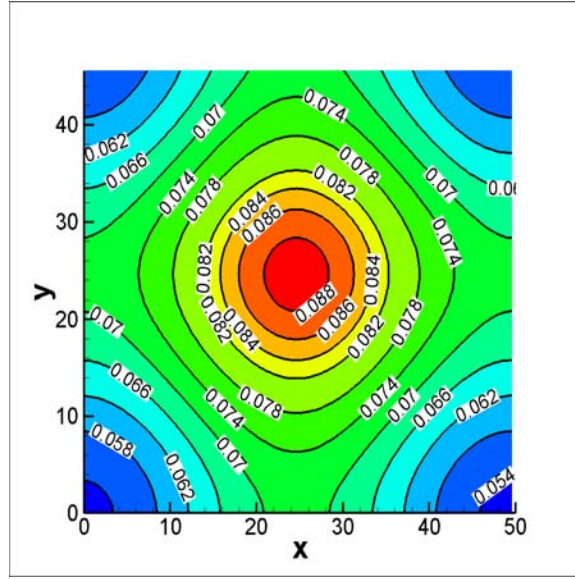
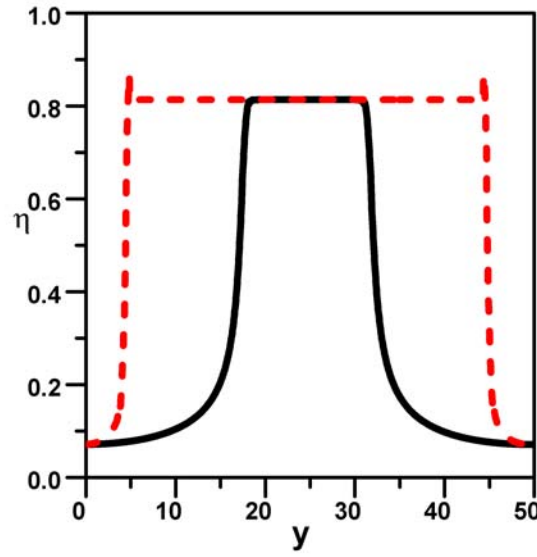


Figure 3.30 Spatial dependence of order parameter profiles for different time values (a) $t=0$, (b) $t=20$, (c) $t=27$, (d) $t=30$, (e) $t=50$ and (f) $t=160$ with $a=0.010$, $\delta=0.009$, $\chi=1$, $L=50$ in Eq. (3.40).



(a)



(a)

Figure 3.31 (a) Contour plot for initial state at $t=0$ and (b) cross section along $x=24.610$ line for $t=30$ (black solid line) and $t=80$ (red dash line) with $a=0.010$, $\delta=0.009$, $\chi=1$, $L=50$ in Eq. (3.40).

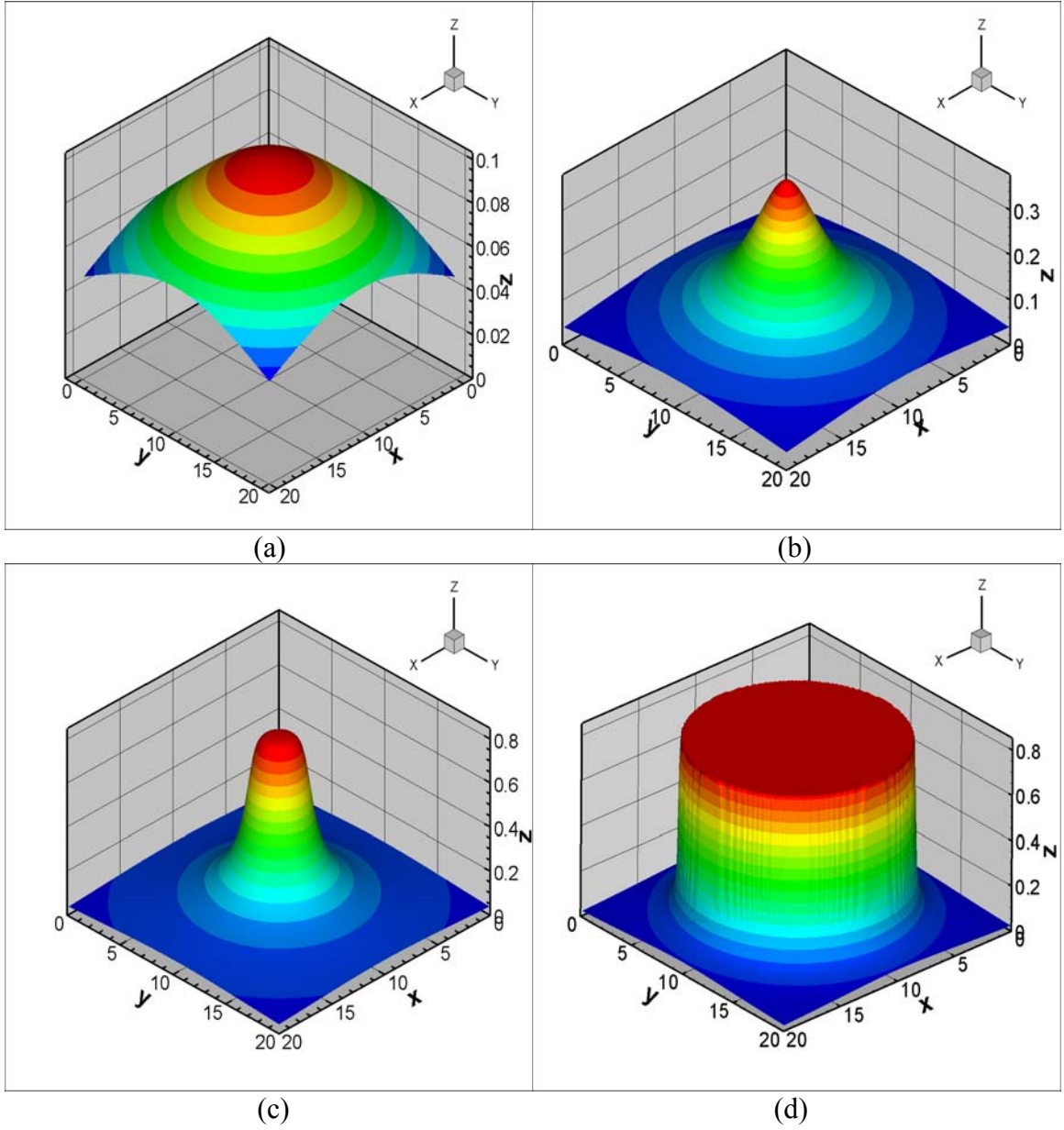


Figure 3.32 Spatial dependence of order parameter profiles for different time values (a) $t=0$, (b) $t=17$, (c) $t=19$ and (d) $t=50$ with $a=0.010$, $\delta=0.005$, $L=20$ in Eq. (3.41).

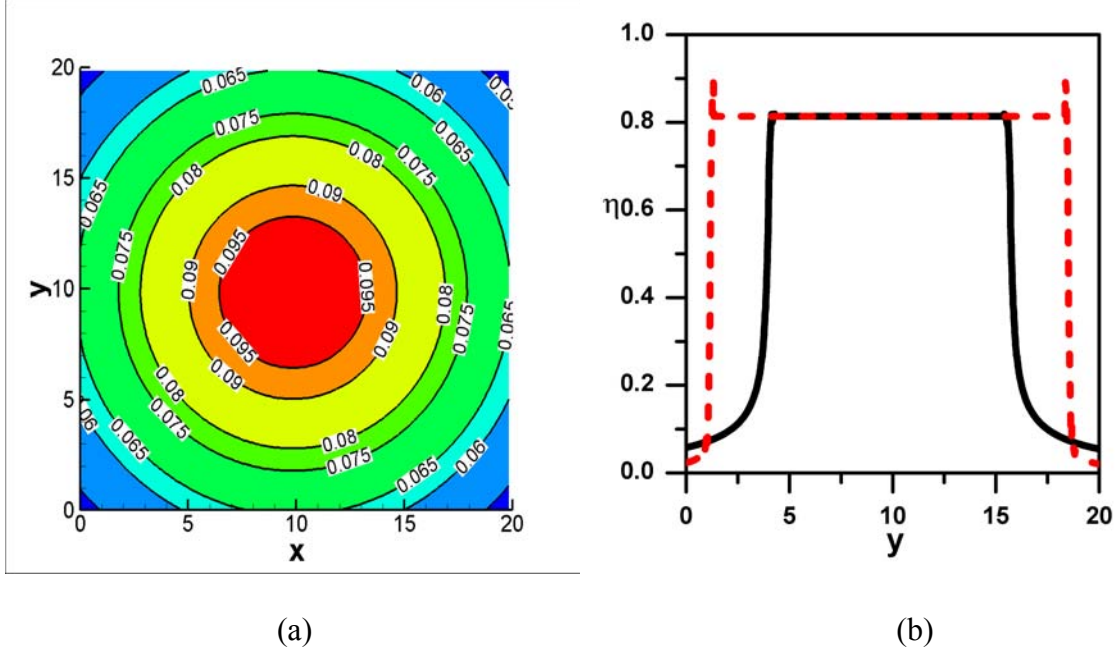


Figure 3.33 (a) Contour plots for initial state at $t=0$ and (b) cross section along $x=9.840$ line for $t=30$ (solid line) and $t=100$ (dash line) with $a=0.010$, $\delta=0.005$, $L=20$ in Eq. (3.41).

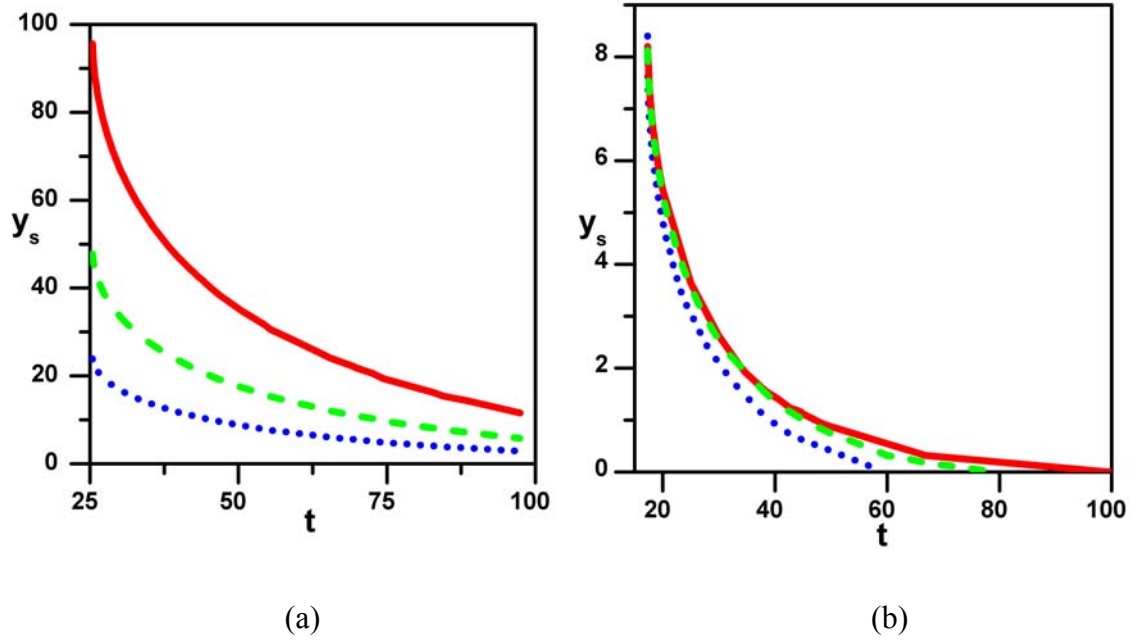


Figure 3.34 (a) front propagation showed by the moving location of $\eta(y)=\bar{\eta}/2$ for thermal fluctuations with $a=0.010$, $\delta=0.009$, $\chi=1$ in Eq. (3.40), along grid lines $x=24.610$ for $L=50$, $x=49.120$ (dot line) for $L=100$ (dash line) and $x=98.240$ for $L=200$ (solid line); (b) front propagation showed by the location of $\eta(y_s)=\eta(y-y_f)=\bar{\eta}/2$ where y_f is the final stable location for soliton-like fluctuations with $a=0.010$, $\delta=0.005$ in Eq. (3.41), along grid lines $x=9.840$ for $L=20$ (dash line), $x=19.680$ for $L=40$ (dot line) and $x=39.360$ for $L=80$ (solid line).

the contrary, we obtain a stable nucleus with fixed domain width $R \approx 8.420$ that is excited from the initial isotropic soliton-like fluctuations (Figure 3.34(b)).

3.8 Heterogeneous Nucleation: Application to Nanosolids

Structure and thermodynamic instability of low-dimensional systems including nanoparticles, nanowires, nanofilms, and nanocrystals, is both scientific and technological interest, in which surfaces and interfaces energy play the important role [159, 160, 161]. Experiments on solid-state amorphization show that a critical crystallite grain size could be achieved in nanocrystalline materials of alloys and single elements systems by using various techniques such as ion implantation, mechanical attrition, vapor deposition, and so on [162--166]. Comparing to the pure element samples, the alloys have a larger critical grain size in presence of solute elements and the size will increase with the composition from a few nanometers to hundreds of nanometers. The energy of grain boundaries may contribute significantly to the crystal to amorphous transformation since the grain size is in the nanometer range. The formation of a topological disordered layer on the boundary by prewetting [167] or premelting would be necessary for the transition to amorphous state [164, 168]. This layer with high strain has the higher value of atomic mean square displacement than the interior of the grain and is amorphous-like. At nanometer scale, the grain in nanocrystals is more closely resemble clusters with short- or medium-range crystalline order embedded in the disordered layer. Once the formation of the disordered layer at the grain boundaries, there will be two possible scenarios, which depends on the interfaces and size of the grains, for the grain from the ordered state to the amorphous state below a critical grain size. The first one is size-driven transition or

‘complete melting’, and the grain is transformed into amorphous phase in one step. Beside the disordered layer surrounded by the grain, another amorphous layer could be induced by the interface between the grains and the grain boundaries before the amorphization and it is called ‘surface-induced melting’ as a two-step process for the second scenario. This phenomenon is analogous to the structure phase transitions in ferroelectric nanostructures [169] and melting in nanoparticles [161].

Experimentally observed enhancement or depression of size-dependent melting points of nanosolids is essentially controlled by the interface properties between the nanoscale objects and its surroundings [170--173]. In 1909, Pawlow [174] reported the decreasing melting points with the decreasing particles’ size and Takagi is the first one to demonstrate the melting depression experimentally in 1954 [175]. From known results, the depressed melting temperature could be linearly or nonlinearly proportional to the reciprocal size [159, 176]. The superheating of nanoparticles in a matrix presents only for coherent or semi-coherent interfaces and melting could be hindered by the lower mean square atomic displacements at the interfaces [176]. Lindemann criterion has been developed to explain the melting depression of nanosolids, which takes account into the influence of surfaces [176],

$$\sigma^2(r) = \sigma_v^2 + (\sigma_s^2 - \sigma_v^2) n_s / n, \quad (3.43)$$

where $\sigma^2(r)$ is the average mean square displacement over the nanosolid, the subscripts s and v represent surface atoms and atoms volume, and n_s is the number of surface atoms and n the total number of atoms of the nanosolid with $n_s/n \sim 1/r$, r is the radius of the nanosolid.

For both solid-state amorphization and melting in nanosolids, the ordered crystalline state may transform to the disordered (amorphous or liquid) state below a critical size. Based on the two scenarios, the polymorphous melting concept could be used to study the size dependent effects, either lowering or enhancing the melting point, where the amorphous state is considered as the undercooled liquid state. In alloy nanosolids, composition disorder will also play an important role to describe the structure and thermodynamic stability beside the structure disorder and size effect [23]. As first order phase transition, Landau theory has been used to investigate the melting of small particles with a semi-finite approach, and size dependent melting temperature and thermodynamic quantities are calculated [177--181]. Also, a thin film model or slab model is applied to study the surface-induced melting of nanoparticles with a parabolic form of Landau free energy and short-range atomic interactions at two boundaries [179], and a two-step melting process is recognized, which include a continuous surface-induced melting and a first order transition. For solid-state amorphization and melting in alloy nanocrystals, composition disorder is included into one-dimensional model based on the flat grain boundary approach [182, 183]. They focus on the grain boundary with finite thickness and the boundary is considered as the undercooled liquid state.

In alloy nanosolids, composition disorder will also play an important role to describe the structure and thermodynamic stability beside the structure disorder and size effect [182]. For solid-state amorphization and melting in alloy nanocrystals, composition disorder is included into one-dimensional model based on the flat grain boundary approach [182, 183]. They focus on the grain boundary with finite thickness and take the two grains as the infinite large systems. A phase diagram is established with a quadratic

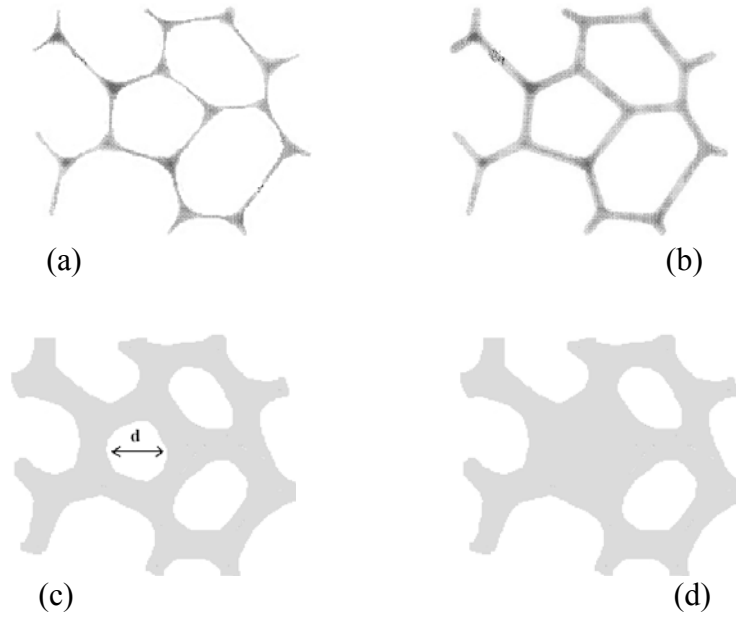


Figure 3.35 Schematic representations of formation of disordered layers at grain boundaries (prewetting or premelting) ((a), (b)) and a subsequent destabilization of grains that have two different models as shown in Figure 3.36 after reaching a critical grain size d (c).

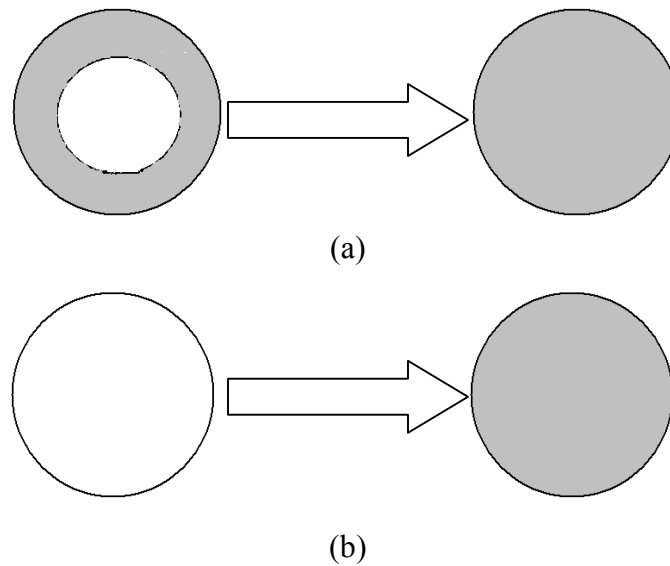


Figure 3.36 Schematic view of two basic processes for melting and amorphization of nanosolids: (a) two-step model with surface-induced transition and first order transition and (b) homogeneous transition.

form of Landau free energy that describes the amorphous phase layer approximation of grain boundary [182].

To understanding the thermodynamic stability of nanoscale crystalline solids, we will apply the built Landau theory from the Chapter II, which include the position disorder and composition disorder, to the thin film model. Phase diagrams are obtained and size-driven phase transition and surface-induced phase transition is observed from our numerical results. Also this model is used to explain the melting depression and superheating in pure elements nanosolids based on the comparison with experimental results. In this part, we will discuss the model and the derivation of the theory for thin film model in Section 1, and the numerical results will be presented and applied to various examples in Section 2 and Section 3. The discussion will be given in Section 4.

3.8.1 Model

We consider a thin film model that a crystalline solid is between two interfaces at $y=0$ and $y=L$, where L is large enough comparing to the microscopic structure, and it is infinite and homogeneous in a plane perpendicular to the direction y . Under stress free condition, we use the same mathematical form as Eq. (3.1) and Eq. (3.2) and the renormalized Landau free energy per unit area is given by

$$F = \int_0^L \left[a\eta^2 - \eta^4 + \eta^6 + \left(\frac{\partial \eta}{\partial y} \right)^2 \right] + f_1(\eta(0)) + f_2(\eta(L)), \quad (3.44)$$

where the terms $f_1(\eta(0))$ and $f_2(\eta(L))$ are the free energy contribution from the surface per unit area and the integral is the part from the bulk free energy. In the following case,

we only assume short-range force at the surfaces and symmetric configuration. For the surface contributions $f_1(\eta(0))$ and $f_2(\eta(L))$, we take them as

$$f_1(\eta(0)) = \frac{1}{\delta} \eta^2(0) \text{ and } f_2(\eta(L)) = \frac{1}{\delta} \eta^2(L), \quad (3.45)$$

which describe the disordering effects of the surfaces with $\eta(0) = \eta(L) = \eta_1$. For $\delta < 0$, the surfaces would like to be in a disordered state; for $\delta > 0$, the tendency of disorder could be suppressed. The spatial dependence of the order parameter is determined by the Euler-Lagrange equation and boundary conditions derived from the free energy Eq. (3.44):

$$\frac{d^2 \eta}{dy^2} = a\eta - 2\eta^3 + 3\eta^5 \quad (3.46)$$

$$\left. \frac{d\eta}{dy} \right|_{y=0} = \frac{1}{\delta} \eta_0 \quad (3.47.a)$$

$$\left. \frac{d\eta}{dy} \right|_{y=L} = \frac{-1}{\delta} \eta_0. \quad (3.47.b)$$

Because of our choice on $C(X)$ in Chapter II, we don't include the temperature dependence on the coefficients q and F_0 . We present some examples and show those coefficients varying with the composition or temperature in Figure 3.37, Figure 3.38 and Figure 3.39. The corresponding correlation length is defined as $\xi = \left(\frac{1}{a}\right)^{1/2}$. We show two

examples for fixed temperature and fixed composition in Figure 3.40 and Figure 3.41. The spatial correlated disorder is increasing with increasing composition at fixed temperature or increasing with decreasing temperature at fixed composition for reentrant melting at low temperature. The increasing thermal disorder will increase the atom mobility and tend to promote the probability of crystallization. Static disorder and

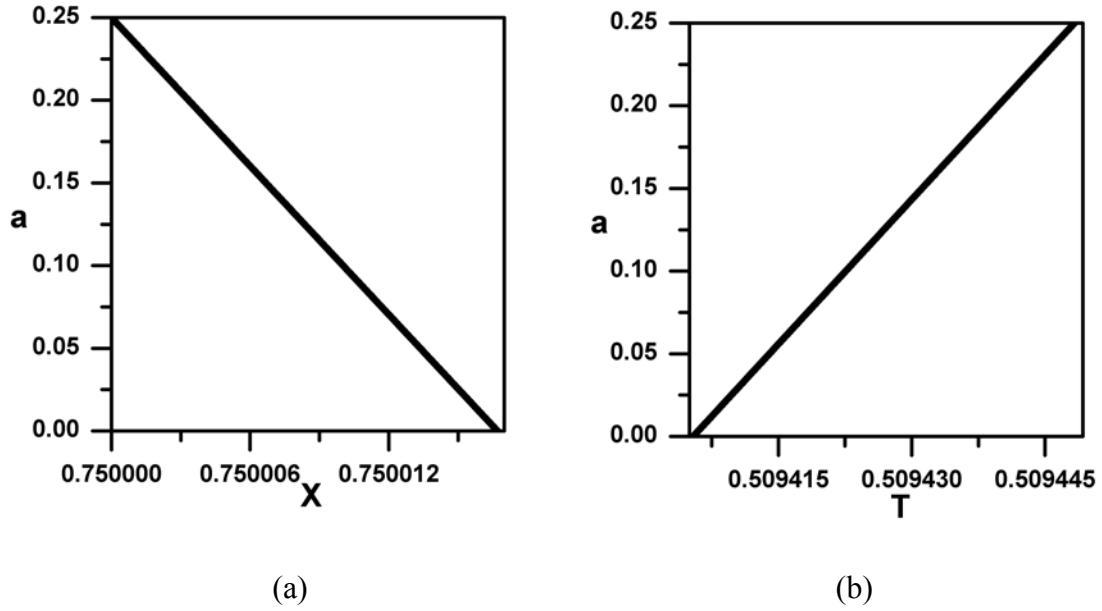


Figure 3.37 Renormalized coefficients of quadratic term of free energy of Eq. (3.2) with parameters in Table 2 (a) At fixed temperature ($T=0.509$); (b) At fixed composition ($X=0.750$).

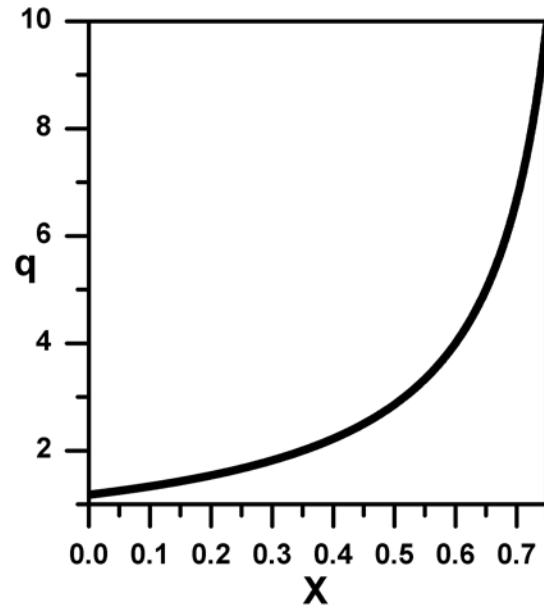


Figure 3.38 The coefficient to rescale the order parameter $q = \left(\frac{E}{|C(X)|} \right)^{1/2}$ as a function of composition at fixed temperature $T=0.509$ with parameters in Table 2.

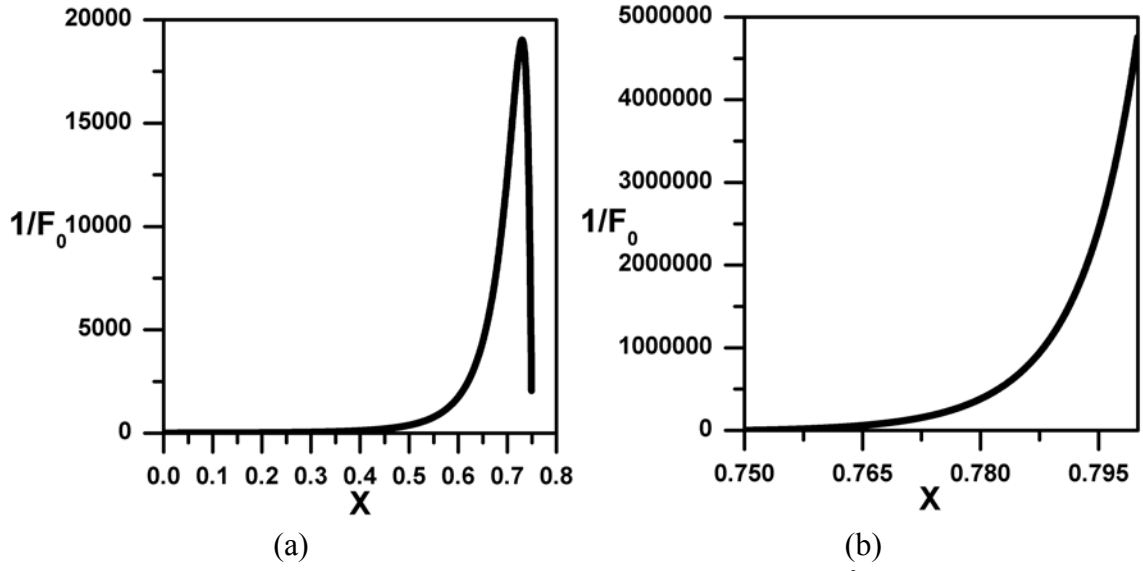


Figure 3.39 The coefficient to rescale the free energy $F_0 = \frac{|C(X)|^3}{E^2}$ as a function of X :
 (a) $X < 0.750$, (b) $X > 0.750$ at fixed temperature $T = 0.509$ with parameters in Table 2.

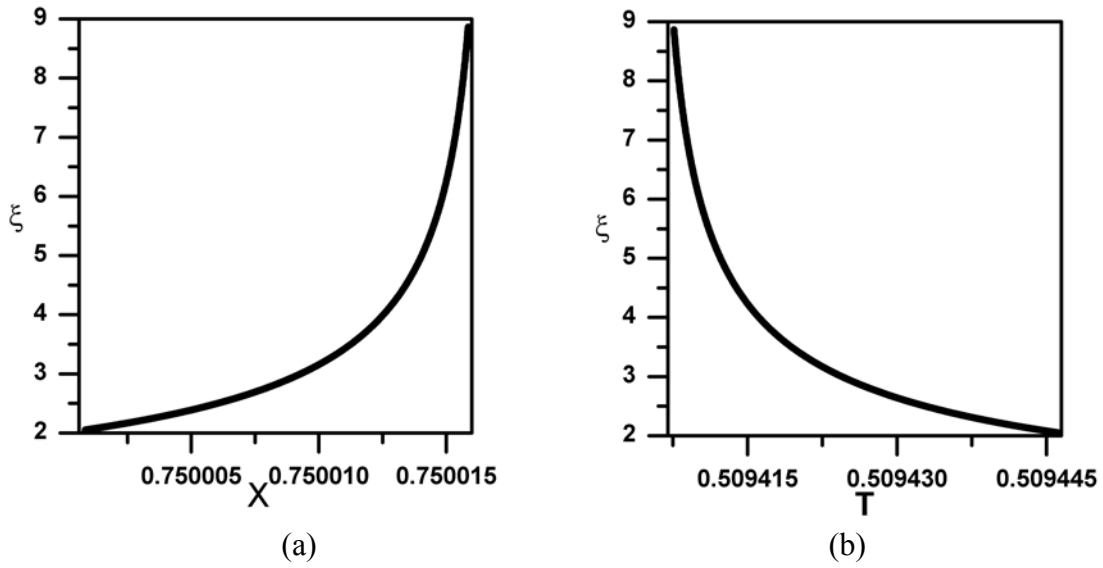


Figure 3.40 Renormalized correlation function $\xi = \left(\frac{1}{a}\right)^{1/2}$: (a) at fixed temperature ($T = 0.509$); (b) at fixed composition ($X = 0.750$) at fixed temperature $T = 0.509$ with parameters in Table 2.

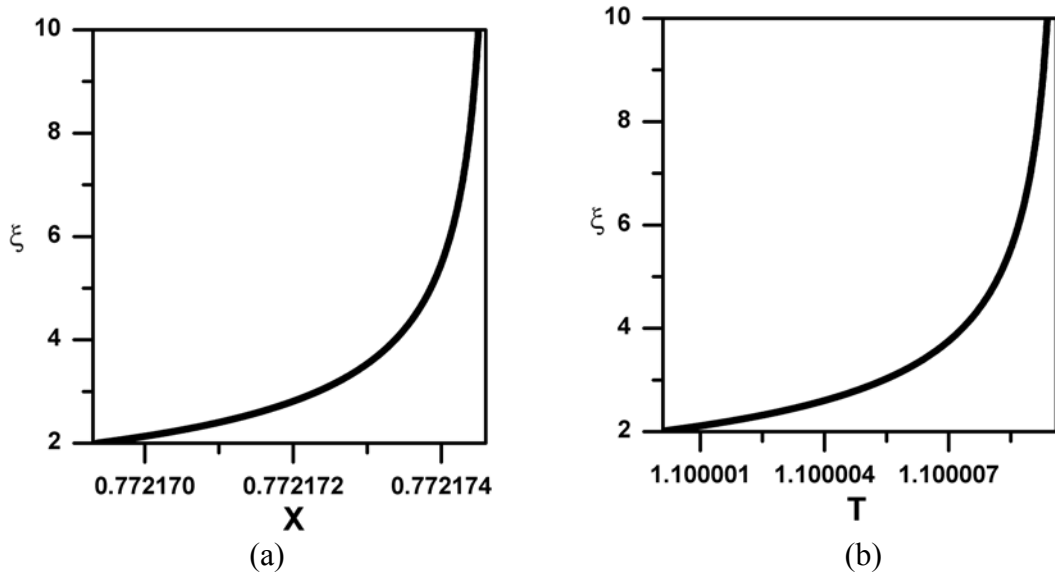


Figure 3.41 Renormalized correlation function $\xi = \left(\frac{1}{a}\right)^{1/2}$: (a) at fixed temperature ($T=1.100$); (b) at fixed composition ($X=0.772$) with parameters in Table 1.

chemical disorder could produce higher probability of nucleation of the amorphous phase with the addition of alloy element.

3.8.2 Numerical Results: Order Parameter Profiles and Phase Diagrams

We will obtain the order parameter profiles at equilibrium by numerical integration of Eq. (3.46). At the transition point, the free energy of the nonzero order parameter solution of Eq. (3.46) is the same as the zero solution. Once the numerical solutions of Eq. (3.46) are found, the free energy of the corresponding system is then determined by numerical integration of Eq. (3.44). The nonzero order parameter solution, the transition point and the free energy could be modified by the relative values of the correlation length ξ , the extrapolation length δ and the thickness L . In our investigation, we will scale δ and L relative to the fixed bulk correlation length $\xi=2$. The extrapolation length δ could be

positive or negative that depends on the depressed or enhanced disordering influence from the interface in our model.

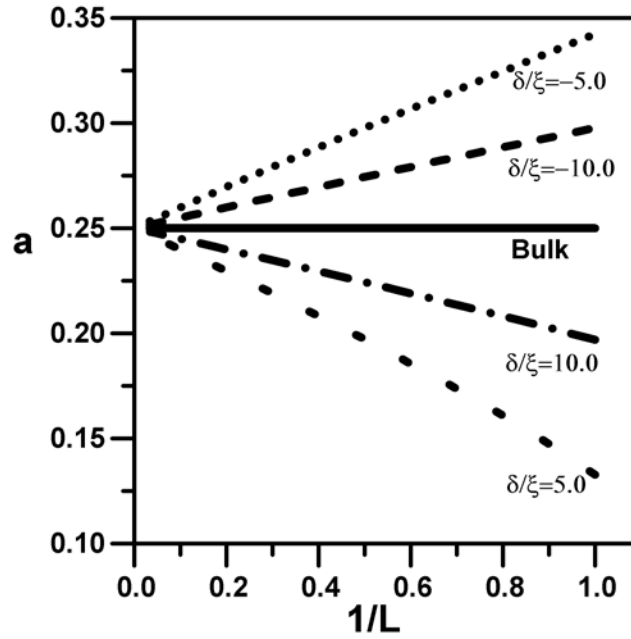
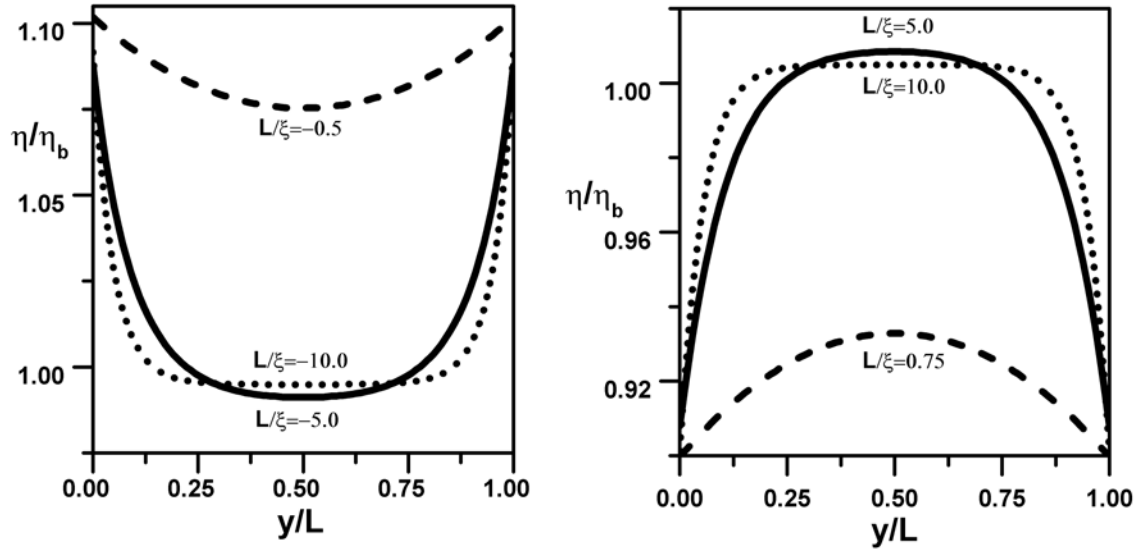


Figure 3.42 The transition points with the reciprocal rescaled thickness for several different δ values.

When $\delta < 0$, the order parameter profiles at the transition points could be slightly increased with the large thickness, and the dependence on the thickness is shown in Figure 3.42. The transition parameter a is increased over the bulk value $a=0.250$, and the decreasing extrapolation length will raise the value of a in Figure 3.42. If $\delta > 0$, the order parameter profiles for different thickness are shown in Figure 3.43, and $\eta(y)$ decreases when the thickness is decreasing. And the transition parameter a is reduced by the surface and lower than the bulk transition parameter. In the limit $L \rightarrow \infty$, the transition parameters will approach the bulk transition value for $\delta > 0$ and $\delta < 0$. For $\delta < 0$, a first order phase transition is observed for large $|\delta|/\xi$ (Figure 3.44) and a surface-induced first order transition is observed when $|\delta|/\xi \ll 1$ and $|\delta|/L \ll 1$ in Figure 3.45(a). The spatial order



(a) (b)
Figure 3.43 The renormalized nonzero order parameter solutions for different rescaled thickness at $\delta/\xi = -5$ (a) and $\delta/\xi = 5$ (b).

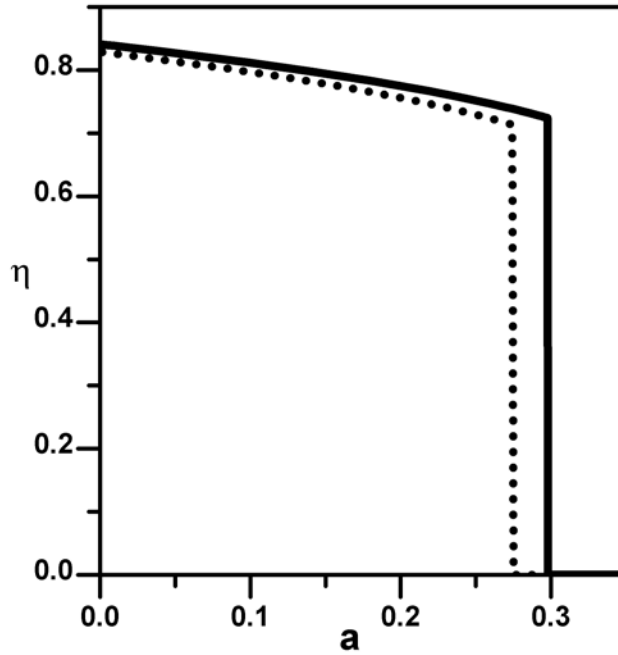


Figure 3.44 The mean order parameter as a function of transition parameters for $L=20$ (dash line) and $L=10$ (solid line) with $\delta/\xi = -1$.

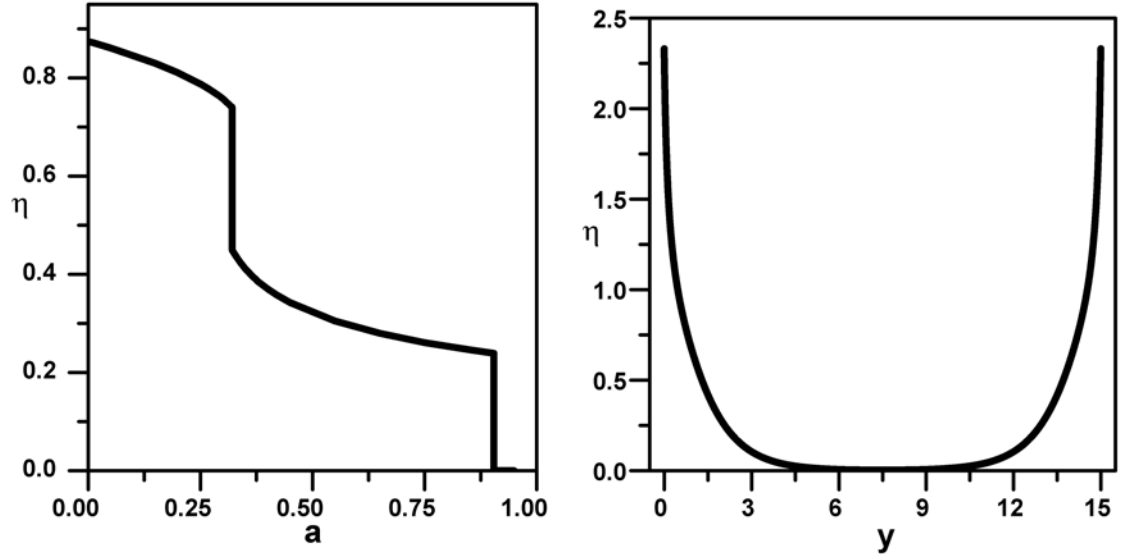


Figure 3.45 (a) The average order parameters as a function of transition parameter for $L=15$ with $\delta/\xi=-0.100$. (b) The order parameter profiles as a function of space coordinates at the surface transition point for $L=15$ with $\delta/\xi=-0.100$.

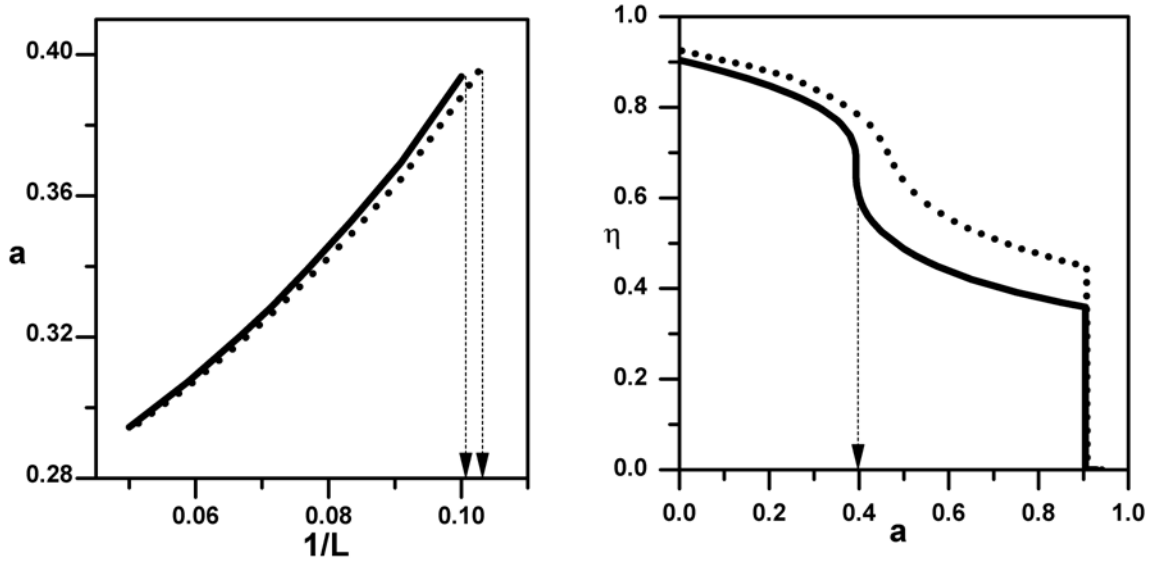


Figure 3.46 (a) The transition points with the reciprocal rescaled thickness for $\delta=-0.100$ (solid line) and $\delta=-0.200$ (dash line). Two arrow lines show the cut-off reciprocal thickness: $L=10$ for $\delta=-0.100$ (solid line) and $L=9.750$ for $\delta=-0.200$ (dash line). (b) The average order parameters as a function of transition parameter for $L=10$ (solid line) and $L=8$ (dot line) with $\delta/\xi=-0.100$. The arrow line shows the second transition point $a \approx 0.390$.

parameter profiles are characterized by a smooth increasing with the distance from the center, which depends on the extrapolation length (Figure 3.45(b)). With the decreasing thickness, the second first order transition point will disappear, and the jump of the order parameter values will increase at the first first-order transition point (Figure 3.46, Figure 3.46). The second transition point disappears around $L=10$ for $\delta/\xi=-0.100$ and around $L=9.750$ for $\delta/\xi=-0.200$ (Figure 3.46).

3.8.3 Numerical Results: Comparison with Experiments

The melting temperature of nanosolids with free surface decreases with their decreasing size, and the similar depression is also observed for nanoparticles embedded in a matrix [170--173]. On the other hand, nanocrystals embedded in a matrix could melt above the bulk melting point. It is reported that Ar, Pb and In particles embedding in a Al matrix show the large enhancement of melting points and the amplitude of thermal vibrations near the interfaces is depressed (Figure 3.47). Either superheating or depression of melting essentially depends on the nature of the interfaces or surfaces [176]. In our model, the nature of the interfaces or surfaces is qualitatively described by the surface free energy term, which depends on the sign and the amplitude of the extrapolation length relative to the thickness and correlation length. Based on our numerical results of Chapter II, we use the coefficients of bulk Landau free energy for the exothermic melting case. For the pure element case, we could set the composition $X=0$ and obtain the corresponding renormalized melting points as a function of reciprocal rescaled thickness for different ratio between the extrapolation length and correlation

length in Figure 3.48(a). Although we couldn't directly set up the corresponding theoretical boundary condition and the corresponding space scale from the experimental data, the obtained renormalized melting point from our model is still give us some valuable information comparing the experiments.

The depression of melting points is caused by the enhanced mean square atomic displacement at the surfaces, and the smaller amplitude of δ suggests the stronger disorder influence from the surfaces (Figure 3.48(b)). On the other hand, the depressed mean square atomic displacement could induce the superheating, which reflects the strongly ordering from the surfaces (Figure 3.48). For large amplitude of δ , either the melting points or the average atomic displacement is almost linearly proportional to the reciprocal thickness, and the nonlinear relation will be promoted for smaller amplitude of δ (Figure 3.48). The negative surface free energy ($\delta < 0$) could lower the system's free energy and be the driving force for melting. The surface contribution will go to zero as $\delta \rightarrow \infty$. When the coupling at the surfaces is large enough, two-step melting is induced for large thickness, which is driven by very low surface free energy (Figure 3.49). The size dependency of the melting temperature is no longer a simple linear or nonlinear relations in terms of the reciprocal thickness any more. And there is a critical thickness for surface-induced melting, and it will become the homogeneous melting once below that size at the fixed extrapolation length. Experiments and theory have proved the reduction in the total interfacial energy, $\Delta\gamma < 0$, is necessary to observe the surface melting for the flat surface (a review in [184]). From our results, it shows a certain thickness is also needed to obtain surface melting (Figure 3.49).

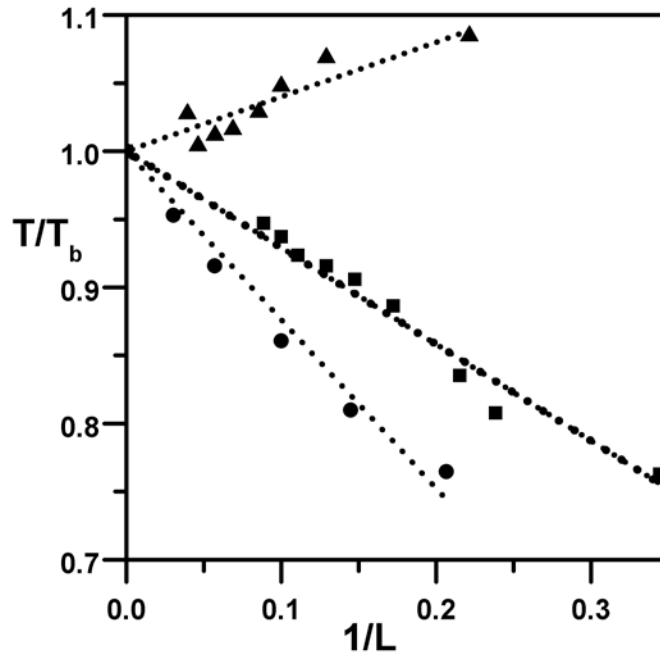


Figure 3.47 The size-dependence of the melting temperature enhancement of In nanosolids in the Al matrix (triangles from [170]) and depression of In nanosolids supported by the amorphous C substrate (squares from [171] and circles from [172]). The red solid lines are the corresponding linear fitting lines that across the limit bulk melting point.

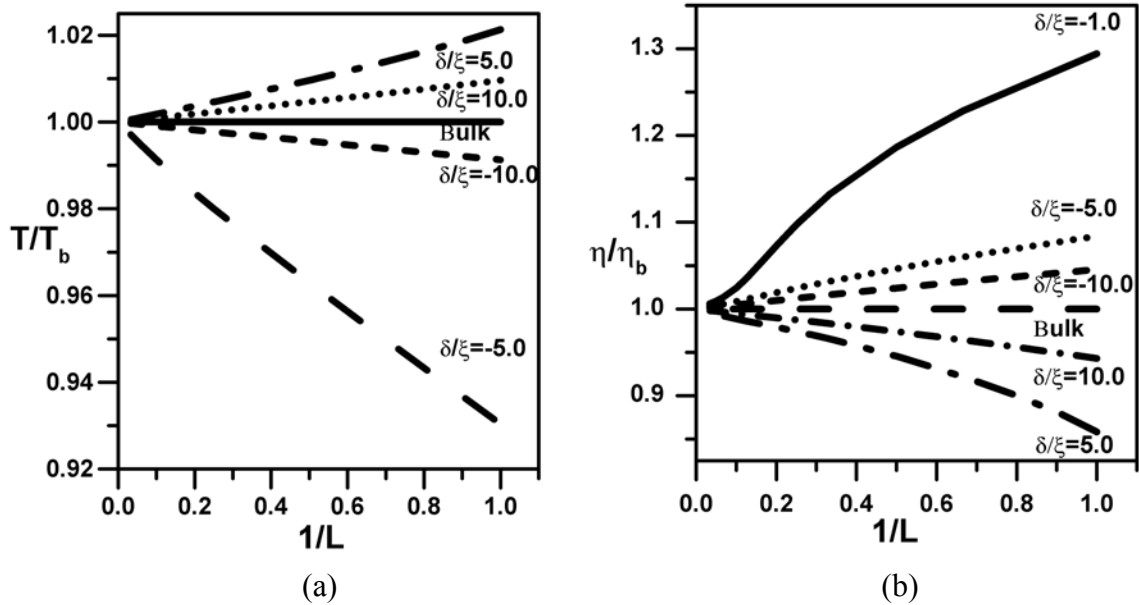


Figure 3.48 (a) The size-dependence of the melting temperature as a function the reciprocal rescaled thickness for different δ/ξ values. (b) The size-dependence of the average order parameters as a function the reciprocal rescaled thickness for different δ/ξ values.

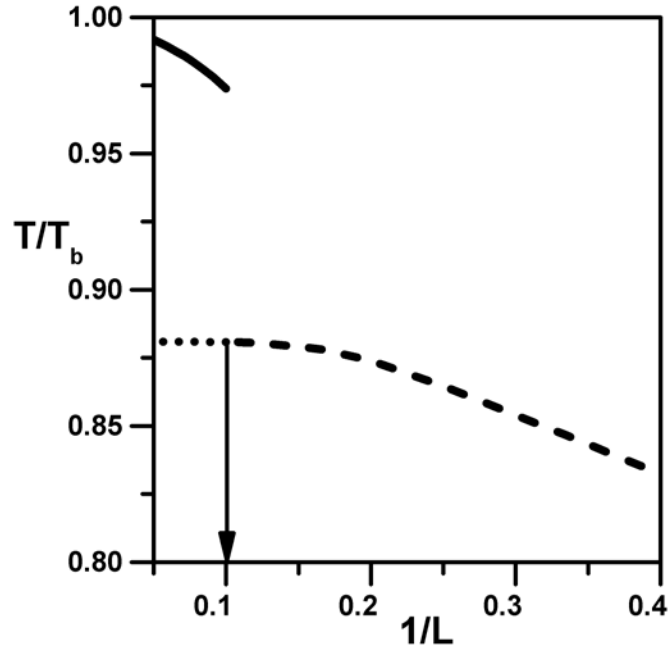


Figure 3.49 The size-dependence of the melting temperature as a function the reciprocal rescaled thickness for $\delta/\xi=-0.100$.

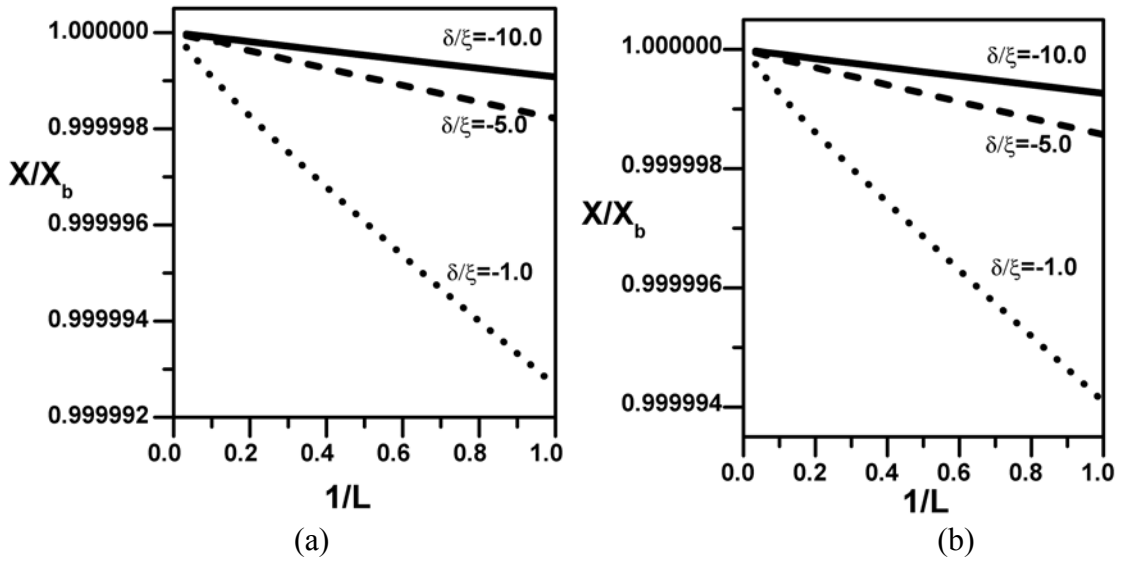


Figure 3.50 (a) $T=1.100$, $X_b=0.772$. The melting points as a function of the reciprocal rescaled thickness for a binary alloy nanosolids with different δ/ξ values (parameters in Table 1). (b) $T=0.509$, $X_b=0.750$. The amorphization points as a function of the reciprocal rescaled thickness for a binary alloy nanosolid with different δ/ξ values (parameters in Table 2).

Structure and thermodynamic stability of binary alloy nanoparticles have also draw some attention, and the composition does play an important role beside the size effect and surface effect. Melting depression and superheating are also observed in some alloys. Experiments explicitly show the formation of a liquid layer at surfaces where the melting initiates and the remaining crystalline interior will transform into the liquid state suddenly [185] (Figure 3.51). The melting point of alloy nanoparticles could be depressed below the corresponding bulk glass temperature, and amorphouslike phase is obtained [186]. For depression, the smaller size could make more reduction of melting temperature with the same composition [185], and our model show that case clearly with the constant surface condition for small composition values. For superheating, smaller size particles showed a larger melting point in Figure 3.54. For two-step melting process, the predicted surface melting line of nanosolids with $L=10$ is lower than the second transition line and bulk melting line, and the difference between them is decreasing with the increasing composition (Figure 3.56). From the experiment [185], the corresponding pure element nanoparticles don't show the liquid layer, which is different with our numerical results that the surface melting is induced for the pure element nanoparticles at constant extrapolation length. Also the experiment data shows the constant surface transition temperature for the interval of large composition. Though there is no interpretation for this so far, initially the surface coupling is increasing with increasing composition. Our numerical results show that surface coupling is relatively small with composition change for the low temperature melting at fixed size. Since the static displacement plays a dominant role for low temperature melting and a certain degree of composition disorder is necessary, the influence of the surfaces is lowered relatively in binary alloy nanosolids.

Enhancement, depression and two-step melting process could also happen for low temperature melting in binary alloy nanosolids.

3.8.4 Discussion

For small systems, such as atomic and molecular clusters and nanosolids with high surface-to-volume ratio, thermodynamics is still developing which is different with classic thermodynamics for macroscopic systems [187, 188] materials, a phase is defined as a portion or the whole of the system with distinguished uniform physical properties such as density, index of refraction and chemical composition and first order phase transition is characterized by the discontinuities of thermodynamic quantities. Phase transitions theory in small systems has attracted lots of attention (a simple review [189]). Unlike the behavior in bulk counterpart as the limit of an infinite system, in general, there is no sharp change in the corresponding thermodynamics functions for first order phase transition in small systems. Also, the definition of ‘phase’ is not appropriate in small systems with high surface inhomogeneity. But, there is still some possible connection in certain cases with the bulk counterpart and the term ‘phase’ still has some sense. One of the cases is melting and freezing of clusters investigated by Berry et al [190, 191]. Based on experiments and computer simulation of phase transitions on clusters, e.g. Ar, solidlike and liquidlike clusters are defined on the difference of rigidity. A solidlike cluster is considered as nearly rigid, conventional atomics or molecular with small-amplitude vibrations and a liquid-like cluster with nonrigidity. The coexistence of solidlike and liquidlike clusters is explored through the simulation and analytical work (reviews in [190, 191]) as long as the time scales are long enough to distinguish them, and

so the free energy has the character that describes metastable states in terms of temperature, order parameter or some other parameters for bulk materials. Simulation results do show Clusters could undergo a first order phase transition indicated by a sharp change on the internal energy [84, 192, 193].

3.9 *Summary*

In this chapter, we propose a microscopic mechanism of the heterophase fluctuations for polymorphic melting in binary alloys, which are inhomogeneous systems characterized with nonlinearity and disorder. Nonlinear energy localization is dominant by the nonlinearity at high temperature. Nonlinear nonthermal energy localization is related to a two-stage process, composition modulation and structure fluctuations, in binary alloys with necessary long-range interactions at low temperature. We use Landau-Ginzburg approach to study the critical nuclei, the growth rate and dissolution in one-dimensional systems. Based on the nonlinear dynamics of the evolution equation, homophase fluctuations and heterophase fluctuations are discussed, which are related to phonons and nonlinear excitations.

We use thin film model to study the surface effect and size dependence of melting for nanosolids with Landau-Ginzburg approach. The equilibrium configurations are obtained defined as absolute minimum of the free energy of inhomogeneous systems. The depression and superheating could be predicted from the appropriate surface condition. The model shows a two-stage first-order phase transitions, i.e. a surface transition first and a subsequent complete transformation, and a homogeneous first-order phase transition for melting in nanosolids.

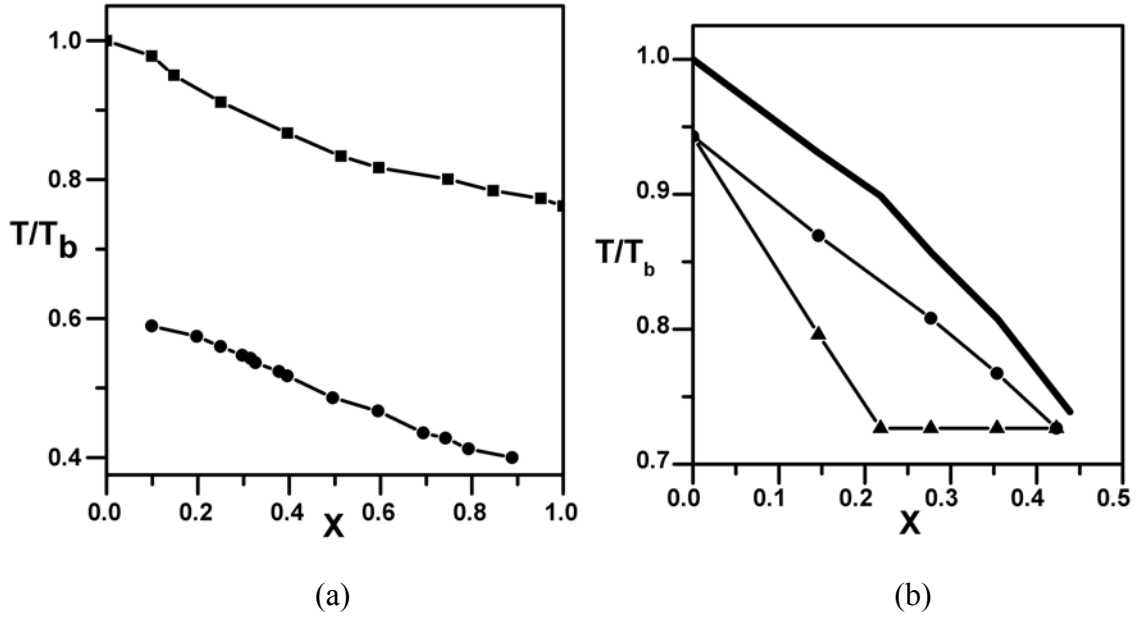


Figure 3.51 (a) Simulated phase diagrams for bulk Pd-Cu alloys and Pd-Cu alloy nanoclusters with the diameter 2.260nm [192]. (b) The experimental binary phase diagram for Bi-Pb nanoparticles with the diameter $D=10$ nm. The dashed lines are from the bulk phase diagram. The triangles are the experimental data for the surface transition lines and the circles for the second transition lines [185].

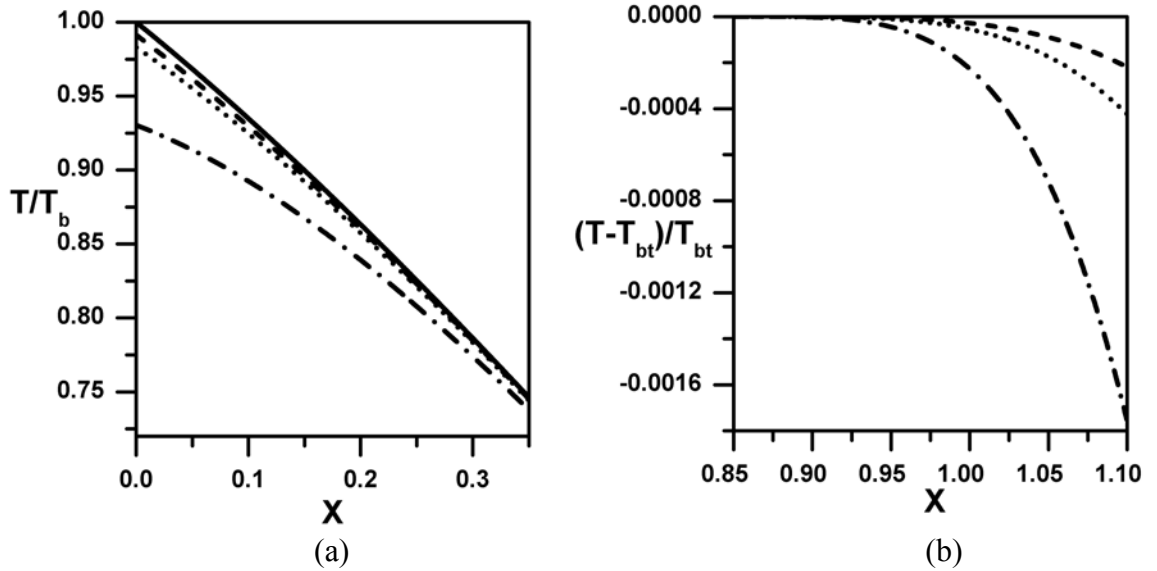


Figure 3.52 (a) Phase diagram for a binary alloy nanosolid with $L=1$ for $\delta/\xi=-1$ (dash dot line), -5 (dot line), -10 (dash line). The blue solid line is the bulk melting line. (b) Phase diagram for low temperature melting for a binary alloy nanosolid with $L=1$ for $\delta/\xi=-1$ (dash dot line), -5 (dot line), -10 (dash line). The temperature is renormalized by the temperature value at the triple point $T_{bt}=0.900$ (see parameters in Table 1).

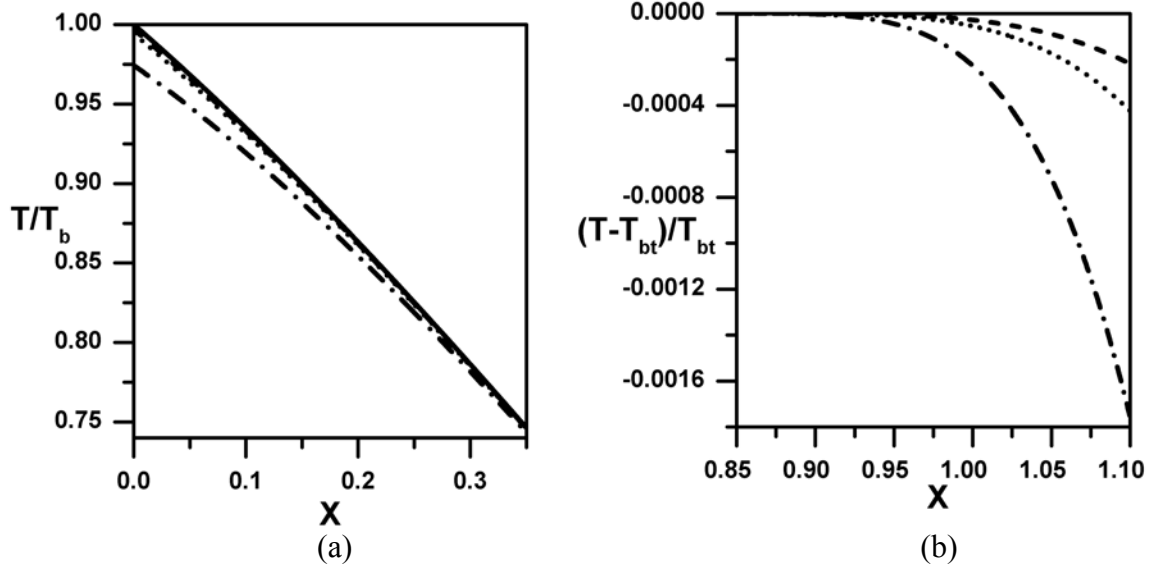


Figure 3.53 (a) Phase diagram for a binary alloy nanosolid with $L=3$ for $\delta/\xi=-1$ (dash dot line), -5 (dot line), -10 (dash line). The blue solid line is the bulk melting line. (b) Phase diagram for low temperature melting for a binary alloy nanosolid with $L=3$ for $\delta/\xi=-1$ (dash dot line), -5 (dot line), -10 (dash line). The temperature is renormalized by the temperature value at the triple point $T_{bt}=0.900$ (see parameters in Table 1).

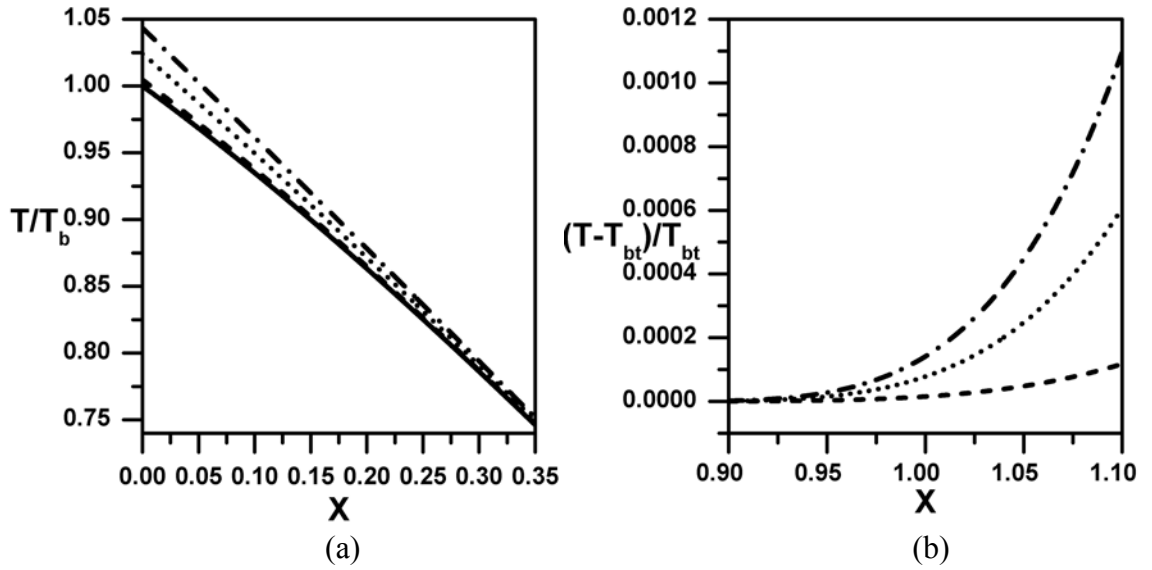


Figure 3.54 (a) Phase diagram for a binary alloy nanosolid with $L=4$ for $\delta/\xi=0.500$ (dash dot line), 1 (dot line), 5 (dash line). The blue solid line is the bulk melting line. (b) Phase diagram for low temperature melting for a binary alloy nanosolid with $L=4$ for $\delta/\xi=0.500$ (dash dot line), 1 (dot line), 5 (dash line). The temperature is renormalized by the temperature value at the triple point $T_{bt}=0.900$ (see parameters in Table 1).

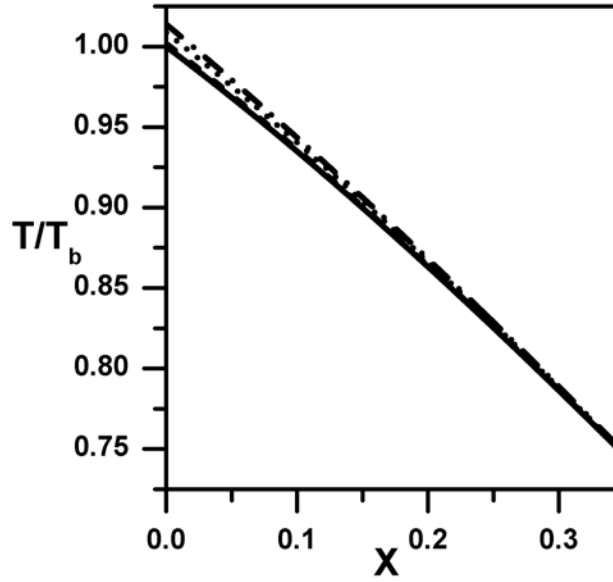


Figure 3.55 Phase diagram for a binary alloy nanosolid with $L=10$ for $\delta/\xi=0.500$ (dash dot line), 1 (dot line), 5 (dash line). The blue solid line is the bulk melting line (see parameters in Table 1).

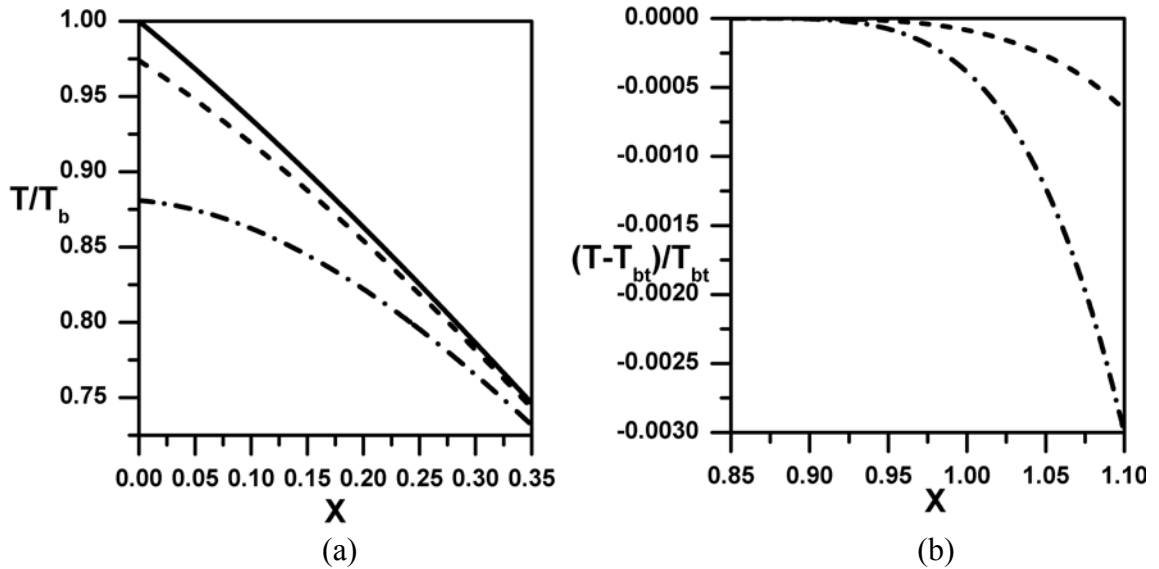


Figure 3.56 (a) Phase diagram for a binary alloy nanosolid with $L=10$ for $\delta/\xi=-0.100$: surface transition line (dash dot line), and second transition line (dash line). The blue line is the bulk melting line. (b) Phase diagram at low temperature melting for a binary alloy nanosolid with $L=10$ for $\delta/\xi=-0.100$: surface transition line (dash dot line), and second transition line (dash line). The temperature is renormalized by the temperature value at the triple point $T_{bt}=0.900$ (see parameters in Table 1).

CHAPTER IV

MULTI-COMPONENT ORDER PARAMETERS AND MODELS IN TWO DIMENSIONS AND THREE DIMENSIONS

4.1 Phase Transitions in Solid Solutions

Various mechanical, chemical, irradiational techniques are developed to study solid-state-amorphization. We will pay more attention to the investigation results by the mechanical methods. Polymorphism phase transitions in solid solutions are one of the observed phenomena during the non-equilibrium processes. Beside amorphization, structural phase transition is obtained, *e.g.* bcc to fcc. Also, nanocrystalline crystals could be made with the variation of the composition.

People also use molecular dynamics simulation to study the amorphization mechanism. In two-dimensional systems, the dislocations are considered to play the major role for the formation of amorphous phase and the nanocrystalline crystals.

To build a multiple-component order parameters model, we have to take care of crystal symmetry. The question to be asked is that: How does the amorphization process related to the crystal symmetry? Or, how does the crystal symmetry breaking during amorphization?

(i) Generalized Lindemann's criterion

In the isotropic approximation, the threshold value exists for the breaking of the crystalline state. But what happens when the displacement parameters are anisotropic?

(ii) Soft modes frustration

One or several soft modes may induce the displacive phase transitions. From that idea, we say the soft modes are extent to the whole crystals. During the amorphization process, more impurities are added in, and soft modes could be localized around the impurities, frustrated. Lots of soft modes are activated and localized and finally the crystal state will transfer into the amorphous state. The possible source of the localization is the random stress field induced by the atomic size differences in solid solutions.

(iii) Replica symmetry breaking (spin-glass like)

Edward-Anderson order parameter is used to characterize the ergodicity breaking.

Based on Imry-Ma's argument, the random fields would break the long-range translational order [194]. Long-range orientational order is more robust than the translational order. An orientationally ordered hexatic phase could be observed during the melting in 2D crystal solids. Also, Shi. *et. al.* studied the grain formation with the strong randomness induced by the defects in 2D crystals [195].

4.2 Structural Phase Transition: Cubic to Tetragonal phase

We use the local atomic displacements as the vector order parameter, which relates to the relative position change between the atoms. We consider a two-component order parameter model with C_{4v} symmetry in two-dimensional space [196].

$$F_0 = \int \left(f(u_x, u_y) + f_g(\nabla u_x, \nabla u_y) + f_c(u_x, u_y, \varepsilon_{ij}) + f_e(\varepsilon_{ij}) \right) d\vec{r} \quad (4.1)$$

$$f(u_x, u_y) = a_1 I_1 + a_2 I_1^2 + a_3 I_1^3 + b_1 I_2 + c_{12} I_1 I_2 \quad (4.1a)$$

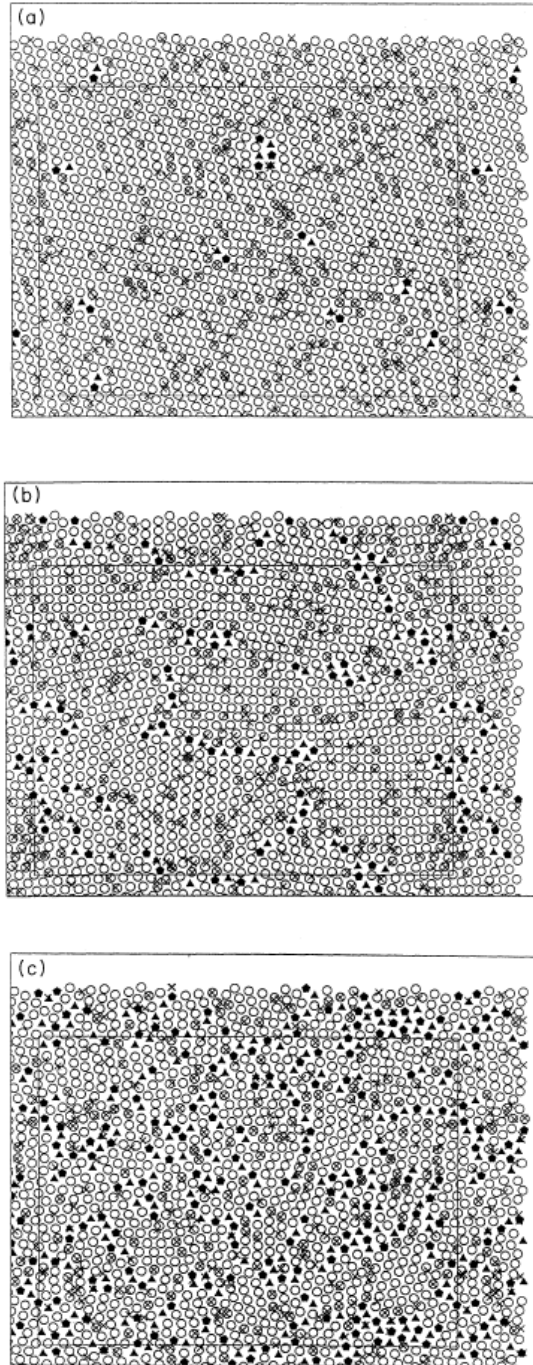


Figure 4.1 Configuration with different randomness in 2D from [195].

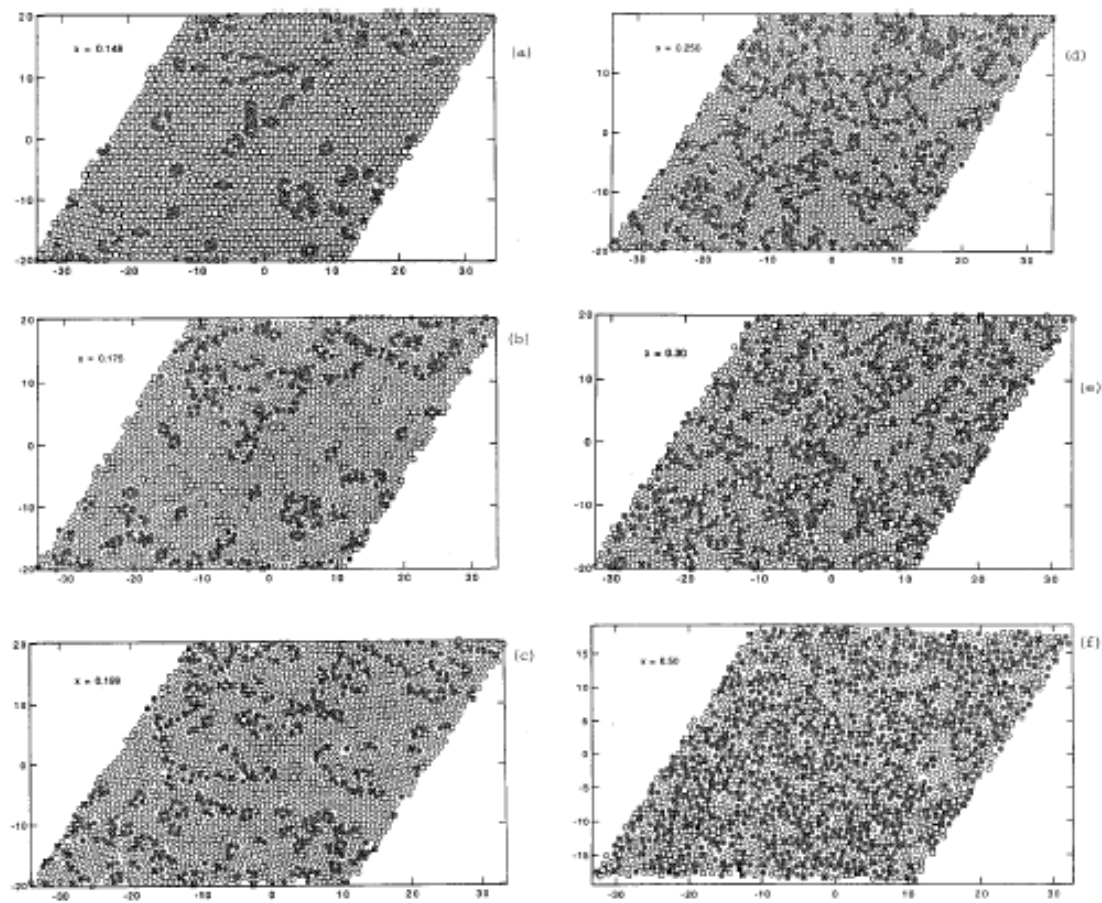


Figure 4.2 The atomic configurations of defects in the binary arrays [23].

$$I_1 = u_x^2 + u_y^2, I_2 = u_x^2 u_y^2 \quad (4.1b)$$

$$f_g(\nabla u_x, \nabla u_y) = \frac{d_1}{2} (\nabla u_x)^2 + \frac{d_2}{2} (\nabla u_y)^2 \quad (4.1c)$$

$$f_e = C_{ijkl} \varepsilon_{ij} \varepsilon_{kl} \quad (4.1d)$$

$$f_c = g u_i u_j \varepsilon_{ij} \quad (4.1e)$$

Under mechanical equilibrium condition, we have:

$$\frac{\delta F}{\delta \varepsilon_{ij}} = 0 \quad (4.2)$$

The renormalized homogeneous free energy part is:

$$\begin{aligned} f_{eff}(u_x, u_y) &= \tilde{a}_1 I_1 + \tilde{a}_2 I_1^2 + \tilde{a}_3 I_1^3 + \tilde{b}_1 I_2 + \tilde{c}_{12} I_1 I_2 \\ &= \tilde{a}_1 (u_x^2 + u_y^2) + B_1 (u_x^4 + u_y^4) + B_2 u_x^2 u_y^2 + C_1 (u_x^6 + u_y^6) + C_2 (u_x^4 u_y^2 + u_x^2 u_y^4) \end{aligned} \quad (4.3)$$

The uniform states are obtained under the stability conditions:

$$\frac{\partial f_{eff}}{\partial u_x} = 0, \frac{\partial f_{eff}}{\partial u_y} = 0 \quad (4.4)$$

$$\frac{\partial^2 f_{eff}}{\partial u_x^2} \geq 0, \frac{\partial^2 f_{eff}}{\partial u_x^2} \frac{\partial^2 f_{eff}}{\partial u_y^2} - \left(\frac{\partial^2 f_{eff}}{\partial u_x \partial u_y} \right)^2 \geq 0 \quad (4.5)$$

We have three different phases:

$$(i) (u_x, u_y) = (0, 0) \quad (4.6)$$

$$(ii) (u_x, u_y) = \left(0, \pm \left(\frac{\tilde{a}_1}{2B_1} \right)^{1/2} \right), (u_x, u_y) = \left(\pm \left(\frac{\tilde{a}_1}{2B_1} \right)^{1/2}, 0 \right) \quad (4.7)$$

$$(iii) (u_x, u_y) = \left(\pm \left(\frac{\tilde{a}_1}{2B_1 + B_2} \right)^{1/2}, \pm \left(\frac{\tilde{a}_1}{2B_1 + B_2} \right)^{1/2} \right), \quad (4.8a)$$

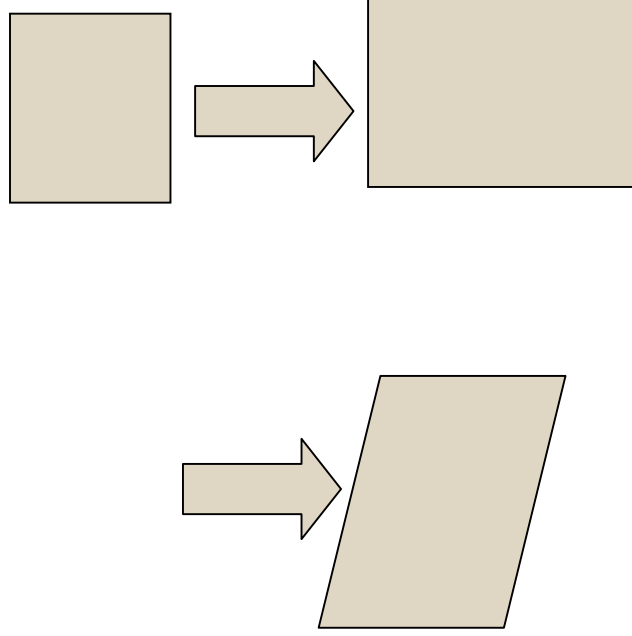


Figure 4.3 Phase (i)----phase (ii) is the transformation from square to rectangle. Phase (i)---- phase (iii) is the transformation from square to parallelogram.

$$(u_x, u_y) = \left(\pm \left(\frac{\tilde{a}_1}{2B_1 + B_2} \right)^{1/2}, \mp \left(\frac{\tilde{a}_1}{2B_1 + B_2} \right)^{1/2} \right) \quad (4.8b)$$

4.3 *Orientational Order Broken and Domain Walls*

Local orientational field is $\Theta(\vec{r})$. The free energy from the orientation disorder is added to Eq. (4.1):

$$F_1 = F_0 + \int (f(\nabla\Theta) + f_c(\nabla u_x, \nabla u_y, \nabla\Theta)) d\vec{r} \quad (4.9)$$

$$f(\nabla\Theta) = O_1 \cdot |\nabla\Theta| + O_2 \cdot |\nabla\Theta|^2 \quad (4.10)$$

$$f_c(\nabla u_x, \nabla u_y, \nabla\Theta) = e_1 \cdot \nabla u_x \bullet \nabla\Theta + e_2 \cdot \nabla u_y \bullet \nabla\Theta \quad (4.11)$$

For mechanical equilibrium condition, the renormalized free energy density is:

$$f_t = f_{eff}(u_x, u_y) + f_g(\nabla u_x, \nabla u_y) + f(\Theta) + f_c(\nabla u_x, \nabla u_y, \nabla\Theta). \quad (4.12)$$

4.3.1 Correlation Functions

Considering the total free energy from Eq. (4.12) up to second order terms, we have:

$$F_t = \int \left(\tilde{a}_1 (u_x^2 + u_y^2) + \frac{d_1}{2} |\nabla u_x|^2 + \frac{d_2}{2} |\nabla u_y|^2 + O_2 |\nabla \Theta|^2 + e_1 \nabla u_x \bullet \nabla \Theta + e_2 \nabla u_y \bullet \nabla \Theta \right) d\vec{r} \quad (4.13)$$

with $O_1 = 0$.

In Fourier space, we get:

$$F_t = \int d\vec{k} \left(\left(\tilde{a}_1 + \frac{d_1}{2} k^2 \right) u_x(\vec{k}) u_x(-\vec{k}) + \left(\tilde{a}_1 + \frac{d_2}{2} k^2 \right) u_y(\vec{k}) u_y(-\vec{k}) + \frac{O_2}{2} k^2 \Theta(\vec{k}) \Theta(-\vec{k}) \right) + \int d\vec{k} \left(e_1 k^2 u_x(\vec{k}) \Theta(-\vec{k}) + e_2 k^2 u_y(\vec{k}) \Theta(-\vec{k}) \right) \quad (4.14)$$

The corresponding coefficients matrix is:

$$\hat{A} = \begin{bmatrix} \tilde{a}_1 + \frac{d_1}{2} k^2 & 0 & \frac{e_1 k^2}{2} \\ 0 & \tilde{a}_1 + \frac{d_2}{2} k^2 & \frac{e_2 k^2}{2} \\ \frac{e_1 k^2}{2} & \frac{e_2 k^2}{2} & O_2 k^2 \end{bmatrix}. \quad (4.15)$$

The correlation function could be obtained from the inverse of the matrix \hat{A} . In particular,

we have (Figure 4.4):

$$\langle u_x(\vec{k}) u_x(-\vec{k}) \rangle = \frac{(-4O_2 d_2 + 2e_2^2) k^2 - 8O_2 a_1}{\xi(k)} \quad (4.16)$$

$$\langle u_y(\vec{k}) u_y(-\vec{k}) \rangle = \frac{(-4O_2 d_1 + 2e_1^2) k^2 - 8O_2 a_1}{\xi(k)} \quad (4.17)$$

$$\langle \Theta(\vec{k}) \Theta(-\vec{k}) \rangle = \frac{-2d_2 d_1 k^4 + (-4a_1 d_2 - 4d_1 a_1) k^2 - 8a_1^2}{\xi(k) \cdot k^2} \quad (4.18)$$

with

$$\xi(k) = \left(-2O_2d_1d_2 + d_1e_2^2 + e_1^2d_2 \right) k^4 + \left(-4O_2a_1(d_2 + d_1) + 2a_1(e_2^2 + e_1^2) \right) k^2 - 8O_2a_1^2$$

4.3.2 Orientational Order and Amorphization in Nanocrystals

For 2D case, we use one component order parameter u to study phase evolution between the crystal and amorphous state. The local orientation field Θ is the angle relative to the reference frame.

$$F = \int f_0(u, \Theta, \varepsilon) d\vec{r} \quad (4.19)$$

$$f_0(u, \Theta, \varepsilon) = \frac{\alpha^2}{2} |\nabla u|^2 + \frac{\gamma(u)}{2} \beta(u) |\nabla \Theta|^2 + f(u) + f_c(u, \varepsilon) + f_e(\varepsilon, \tau) \quad (4.20)$$

$$f(u) = \frac{a}{2} u^2 + \frac{b}{4} u^4 + \frac{c}{6} u^6 \quad (4.21a)$$

$$f_c(u, \varepsilon) = e \cdot u \cdot \varepsilon \quad (4.21b)$$

$$f_e(\varepsilon) = \frac{\mu_0}{2} \cdot \varepsilon^2 \quad (4.21c)$$

The coefficient $\beta(u)$ is some monotonic function of u , and we keep $\beta(u) = 0$ at the transition point to eliminate the meaningless definition for amorphous state. $f(u)$ is the homogeneous free energy. $f_e(\varepsilon)$ is the elastic free energy.

Under mechanical equilibrium condition (stress free), the system has the minimum free energy:

$$\frac{\delta F}{\delta \varepsilon} = 0. \quad (4.22)$$

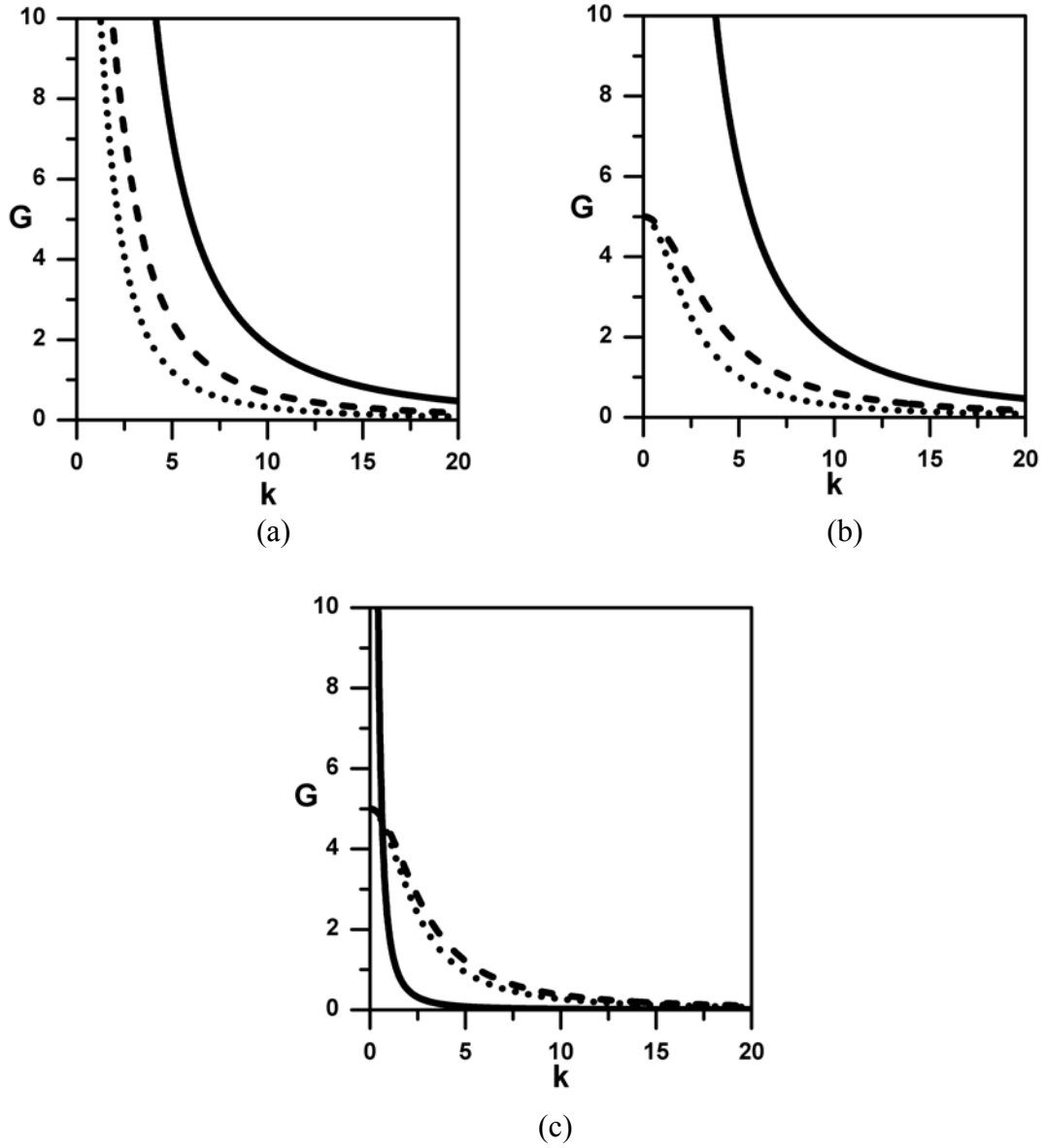


Figure 4.4 Correlation functions in Fourier space with (a) $a_1=0.050$, $d_1=0.050$, $d_2=0.070$, $e_1=0.020$, $e_2=0.010$, $O_2=0.010$, (b) $a_1=0.200$, $d_1=0.050$, $d_2=0.070$, $e_1=0.020$, $e_2=0.010$, $O_2=0.010$ and (c) $a_1=0.200$, $d_1=0.050$, $d_2=0.070$, $e_1=0.020$, $e_2=0.010$, $O_2=0.500$. The solid line is $\langle \Theta(\vec{k})\Theta(-\vec{k}) \rangle$, the long dash line $\langle u_x(\vec{k})u_x(-\vec{k}) \rangle$, and the space dot line is $\langle u_y(\vec{k})u_y(-\vec{k}) \rangle$.

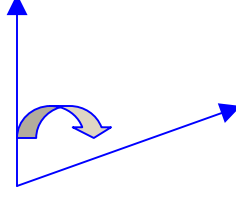


Figure 4.5 Representation of orientation field at one location.

We obtain the relation:

$$e \cdot u + \mu_0 \varepsilon = 0 \quad (4.23)$$

$$\varepsilon = -\frac{e \cdot u}{\mu_0} \quad (4.24)$$

The effective free energy density is:

$$f_{\text{eff}}(u) = \frac{A}{2} \cdot u^2 + \frac{b}{4} u^4 + \frac{c}{6} u^6 \quad (4.25)$$

$$\tilde{f}_0(u, \Theta, \varepsilon) = \frac{\alpha^2}{2} |\nabla u|^2 + \frac{\gamma(u)}{2} \beta(u) |\nabla \Theta|^2 + f_{\text{eff}}(u) \quad (4.26)$$

$$A = a - \frac{e^2}{\mu_0} \quad (4.27)$$

For a simple case, we choose $\beta(u) = 1 - u^2$ and α as some constant. We also choose $\gamma(u) = \gamma$ as a constant. We do the transformation into the Fourier space and keep the term up to second order:

$$F = \int d\vec{k} \left(\frac{\alpha^2}{2} k^2 u(\vec{k}) u(-\vec{k}) + \frac{\gamma}{2} \Theta(\vec{k}) \Theta(-\vec{k}) + \frac{A}{2} u(\vec{k}) u(-\vec{k}) \right) \quad (4.28)$$

$$F = \int d\vec{k} \left(\frac{1}{2} (A + \alpha^2 k^2) u(\vec{k}) u(-\vec{k}) + \frac{\gamma}{2} \Theta(\vec{k}) \Theta(-\vec{k}) \right) \quad (4.29)$$

We could directly write out the correlation function in Fourier space:

$$G_{\Theta\Theta} = \frac{2}{\gamma k^2} \quad (4.30a)$$

$$G_{uu} = \frac{2}{A + \alpha^2 k^2} \quad (4.30b)$$

The corresponding correlation functions in real space are:

$$G_{\Theta\Theta}(r) \sim 2(-2 * EulerGamma - 2 \log(r)) \quad (4.31a)$$

$$G_{uu}(r) \sim \frac{2}{\alpha^2} K_0\left(\frac{A}{\alpha^2} r^2\right) \quad (4.31b)$$

where K_0 is the modified Bessel function of the second kind.

We use *quaternions*, $\vec{\eta} = (\eta_0, \eta_1, \eta_2, \eta_3)$, to describe the local crystallographic orientation

in three dimension. We have

$$\eta_0 = \cos\left(\frac{\theta}{2}\right), \eta_1 = n_1 \sin\left(\frac{\theta}{2}\right), \eta_2 = n_2 \sin\left(\frac{\theta}{2}\right), \eta_3 = n_3 \sin\left(\frac{\theta}{2}\right),$$

and $\sum_i \eta_i^2 = 1$. \vec{n} is the unit vector of the rotation axis.

$$F = \int \left(\frac{\alpha^2}{2} |\nabla u|^2 + \frac{\gamma(u)\beta(u)}{2} \sum_i |\nabla \eta_i|^2 + f(u) \right) d \quad (4.32)$$

In Fourier space, we keep those terms up to the second order:

$$F = \int d\vec{k} \left(\frac{1}{2} (A + \alpha^2 k^2) \mu(\vec{k}) \mu(-\vec{k}) + \frac{\gamma}{2} \sum_i \eta_i(\vec{k}) \eta_i(-\vec{k}) \right) \quad (4.33)$$

The correlation functions in Fourier space are:

$$G_{u\eta_i} = 0 \quad (4.34a)$$

$$G_{\eta\eta} = \frac{1}{\frac{\gamma}{2} k^2} \quad (4.34b)$$

$$G_{uu} = \frac{1}{\frac{A}{2} + \frac{\alpha^2}{2}k^2} \quad (4.34c)$$

In the real space, the corresponding correlation functions are:

$$G_{u\eta_i}(r) = 0 \quad (4.35a)$$

$$G_{\eta_i\eta_i}(r) \sim \frac{2}{\gamma r} \quad (4.35b)$$

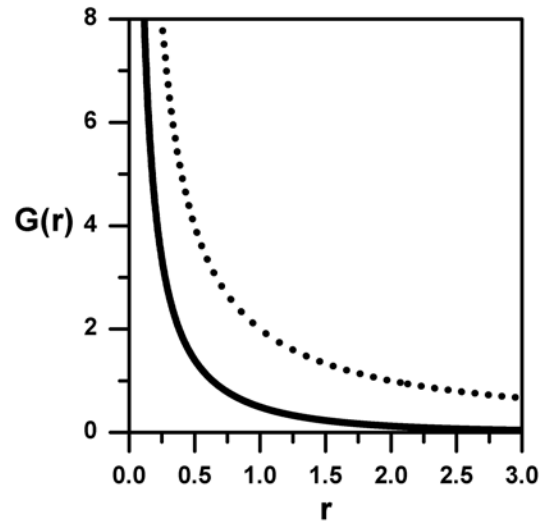
$$G_{uu}(r) \sim \frac{2 \exp\left(-r/\xi\right)}{Ar} \quad \xi^2 = \frac{\alpha^2}{A} \quad (4.35c)$$

The following examples are the disorder parameter correlation function (with solid line) and the orientation field correlation function (with space dash) in Figure 4.6.

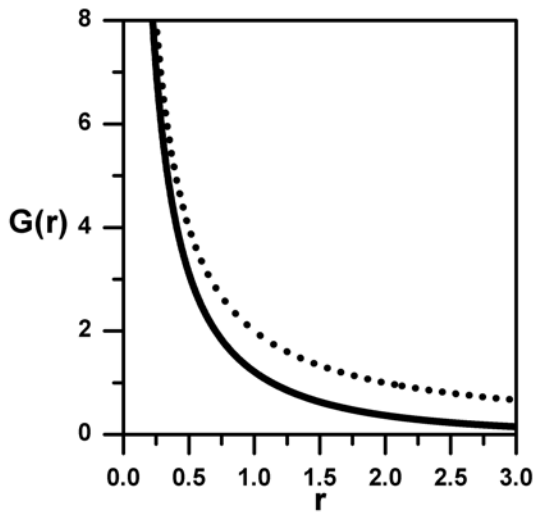
4.4 Summary

By tuning the degree of disorder with the addition of solvent atoms, the initial solute lattice could be destabilized and transformed into another low symmetry crystalline lattice before the formation of amorphous phase. This route could be related to the different single crystalline lattices between solvent and solute atoms. The accompanying softening of elastic constants is observed. A unified model is not impossible to describe the route.

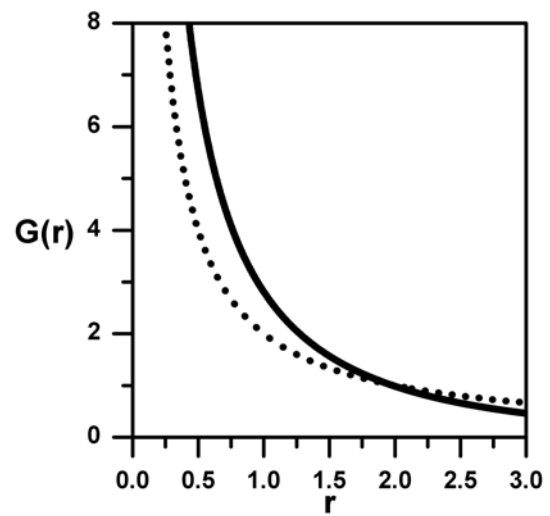
Orientational degree of freedom does play an important role in melting and solid-state amorphization in two-dimensional systems [23, 46]. A hexatic phase characterized by quasi-long-ranged orientational symmetry is obtained. In nanocrystalline materials, orientational order of the grains has been studied by discontinuity at the grain boundaries in one-dimensional model [183].



(a)



(b)



(c)

Figure 4.6 Disorder parameter correlation function (solid line) and orientation field correlation function (dot line) at (a) $\gamma=1$, $A=2$ and $\alpha=2$; (b) $\gamma=1$, $A=1$ and $\alpha=2$; (c) $\gamma=1$, $A=0.500$ and $\alpha=2$.

CHAPTER V

CONCLUSION AND FUTURE WORKS

In this thesis, we report on the modeling, analysis, and simulation of heat-induced polymorphic melting and solid-state polymorphic amorphization in binary solid solutions. As first order phase transition, we developed phenomenological theory to study bulk thermodynamic properties in macroscopic systems, fluctuations and nucleation in mesoscopic inhomogeneous systems. We focus on the position disorder and composition disorder on the characterization of the underlying transition processes in the framework of Landau theory.

For the bulk systems, binary phase diagrams and thermodynamic quantities are obtained for two cases, i.e. endothermic melting and exothermic melting at low temperature, based on different mathematical forms of Landau free energy. At high temperature, they both are endothermic and dominant by thermal disorder. When reaching low temperature, static disorder and composition disorder govern the processes. For exothermic case, the typical chemical short-range order developed in the amorphous state is responsible for the reduced entropy change.

On the mesoscopic scale, we use Landau-Ginzburg approach to investigate homophase and heterophase fluctuations in binary systems. We generalize the nonlinear energy localization as a microscopic mechanism of heterophase fluctuations based on two-step process, i.e. modulation instability induced by composition modulation and the subsequent structure fluctuations. In one-dimensional systems, analytical results and numerical simulation are used to study the growth and dissolution of critical nuclei and the growth rate of domain width is linear. For two-dimensional model with periodic

boundary condition, the numerical results show a growing an-isotropic nucleus initiated from small amplitude thermal fluctuations and a stable nucleus initiated from soliton-like isotropic perturbation. The stable nucleus has a fixed domain width and does not change with the system's size. In finite systems, we propose two basic models on solid-state polymorphic amorphization and investigate the polymorphic transitions with thin film model by Landau-Ginzburg approach including surface contribution. Our model does predict the melting depression and superheating of nanosolids and the linear relations between the melting point and the reciprocal size for depression. The surface melting shows a first order phase transition character that consistent with the experiments in binary alloys.

To summarize, this thesis models the polymorphic melting and polymorphic amorphization in the framework of Landau phenomenological theory as a first order phase transition. There are several remarks for future works. (1) The rigorous results on phase transition in one-dimensional inhomogeneous systems need to draw some attention. The energy localization mechanism in inhomogeneous systems could be investigated by molecular dynamics simulation. (2) Dynamics of the fraction of transformed regions in systems could be studied by numerical simulation although the rigorous studying is still missing. Landau-Ginzburg approach could be used to study nucleation and growth phenomena in two dimensions and three dimensions. The definition of critical nuclei is still not clear for high dimensions. (3) In finite systems, surface stress caused by lattice mismatch could play an important role on the nanosolids properties and geometry factor should be also included.

APPENDIX A

$$\tilde{A}_2(X) \cdot (T_1 - \tilde{T}_0)^2 + \tilde{A}_1(X) \cdot (T_1 - \tilde{T}_0) + \tilde{A}_0(X) = \frac{C^2(X)}{3E}$$

$$\tilde{A}_2(X) \cdot (T_m - \tilde{T}_0)^2 + \tilde{A}_1(X) \cdot (T_m - \tilde{T}_0) + \tilde{A}_0(X) = \frac{C^2(X)}{4E}$$

$$\tilde{A}_2(X) \cdot (T_0 - \tilde{T}_0)^2 + \tilde{A}_1(X) \cdot (T_0 - \tilde{T}_0) + \tilde{A}_0(X) = 0$$

We rewrite the equations:

$$\tilde{A}_2(X) \cdot (T_1 - \tilde{T}_0)^2 + \tilde{A}_1(X) \cdot (T_1 - \tilde{T}_0) + \tilde{A}_0(X) - \frac{C^2(X)}{3E} = 0$$

$$\tilde{A}_2(X) \cdot (T_m - \tilde{T}_0)^2 + \tilde{A}_1(X) \cdot (T_m - \tilde{T}_0) + \tilde{A}_0(X) - \frac{C^2(X)}{4E} = 0$$

$$\tilde{A}_2(X) \cdot (T_0 - \tilde{T}_0)^2 + \tilde{A}_1(X) \cdot (T_0 - \tilde{T}_0) + \tilde{A}_0(X) = 0$$

The solutions for the parabolic equations:

$$T_1^1 = \tilde{T}_0 + \frac{-\tilde{A}_1(X) - \sqrt{\tilde{A}_1(X)^2 - 4\tilde{A}_2(X)\left(\tilde{A}_0(X) - \frac{C^2(X)}{3E}\right)}}{2\tilde{A}_2(X)}$$

$$T_1^2 = \tilde{T}_0 + \frac{-\tilde{A}_1(X) + \sqrt{\tilde{A}_1(X)^2 - 4\tilde{A}_2(X)\left(\tilde{A}_0(X) - \frac{C^2(X)}{3E}\right)}}{2\tilde{A}_2(X)}$$

$$T_m^1 = \tilde{T}_0 + \frac{-\tilde{A}_1(X) - \sqrt{\tilde{A}_1(X)^2 - 4\tilde{A}_2(X)\left(\tilde{A}_0(X) - \frac{C^2(X)}{4E}\right)}}{2\tilde{A}_2(X)}$$

$$T_m^2 = \tilde{T}_0 + \frac{-\tilde{A}_1(X) + \sqrt{\tilde{A}_1(X)^2 - 4\tilde{A}_2(X)\left(\tilde{A}_0(X) - \frac{C^2(X)}{4E}\right)}}{2\tilde{A}_2(X)}$$

$$T_0^1 = \tilde{T}_0 + \frac{-\tilde{A}_1(X) - \sqrt{\tilde{A}_1(X)^2 - 4\tilde{A}_2(X)\tilde{A}_0(X)}}{2\tilde{A}_2(X)}$$

$$T_0^2 = \tilde{T}_0 + \frac{-\tilde{A}_1(X) + \sqrt{\tilde{A}_1(X)^2 - 4\tilde{A}_2(X)\tilde{A}_0(X)}}{2\tilde{A}_2(X)}$$

For the low branches, we should have $\tilde{T}_0 > T_1^2 > T_m^2 > T_0^2$; For the up braches we should have $\tilde{T}_0 < T_1^1 < T_m^1 < T_0^1$. Since $C^2(X)/E > 0$, $\tilde{A}_2(X) < 0$, $\tilde{A}_1(X) < 0$ and $\tilde{A}_0(X) > 0$, we need $\tilde{A}_0(X) > C^2(X)/3E$.

APPENDIX B

For a second order autonomous ordinary differential equation, the standard form is:

$$\frac{d^2 X}{dt^2} = f(X). \quad (1)$$

We rewrite it as two first order ODE:

$$\begin{aligned} \frac{dX}{dt} &= Y \\ \frac{dY}{dt} &= f(X) \end{aligned} \quad (2)$$

The critical point (\tilde{X}, \tilde{Y}) of the system (1) satisfies:

$$\tilde{Y} = 0, \quad f(\tilde{X}) = 0 \quad (3)$$

Near the critical point, we consider small perturbation:

$$\delta X = X - \tilde{X}, \delta Y = Y - \tilde{Y} \quad (4)$$

The corresponding Jacobian matrix at critical point (\tilde{X}, \tilde{Y}) is:

$$A = J(\tilde{X}, \tilde{Y}) = \begin{bmatrix} 0 & 1 \\ f'(\tilde{X}) & 0 \end{bmatrix} \quad (5)$$

The linearized equation is

$$\frac{dV}{dt} = AV$$

$$\text{with } V = \begin{pmatrix} \delta X \\ \delta Y \end{pmatrix}.$$

The corresponding eigenvalues and eigenfunctions satisfy:

$$|A - \lambda I| = 0$$

$$(A - \lambda_j I)e_j = 0 \quad e_j \neq 0$$

REFERENCES

- [1]. R.C. Ewing, *Nucl. Instr. Meth. B* **91**, 22 (1994); L.M. Wang and R.C. Ewing, *Mater. Res. Soc. Bull.* **5**, 38 (1992).
- [2]. W. Buckel, R. Hilsch, *Z. phys.* **138**, 109 (1954); W. Buckel, *Z. Phys.* **138**, 136 (1954).
- [3]. W. Klement Jr., R. H. willens, P. Duwez, *Nature* **187**, 869 (1960).
- [4]. Bloch J., *J. Nucl. Mater.* **6**, 203 (1962).
- [5]. H. J. Fecht, W. L. Johnson, *Nature* **334**, 50 (1988); W. L. Johnson, H. J. Fecht, *J. Less-Common Met.* **145**, 63 (1988).
- [6]. C. Ettl, K. Samwer, *Mater. Sci. Eng. A* **178**, 245 (1994).
- [7]. C. E. Krill III, J. Li, C. M. Garland, C. Ettl, K. Samwer, W. B. Yelon, and W. L. Johnson, *J. Mater. Res.* **10**, 280 (1995).
- [8]. H. W. Sheng, Y. H. Zhao, Q. Hu, K. Lu, *Phys. Rev. B* **56**, 2302 (1997).
- [9]. H. W. Sheng, K. Lu, E. Ma, *J. App. Phys.* **85**, 6400 (1999); G. Veltl, B. Scholz, and H.D. Kunze, *Mater. Sci. Eng. A* **134**, 1410 (1991).
- [10]. K. S. Huang, *Statistical Mechanics*, (John Wiley & Sons, 1987), 2nd.
- [11]. R. W. Cahn, W. L. Johnson, *J. Mater. Res.* **1**, 724 (1986); W. L. Johnson, *Prog. Mater. Sci.* **30**, 81 (1986); W. L. Johnson, H. J. Fecht, *J. Less-Common Met.* **145**, 63 (1988)..
- [12]. P. Richet, *Nature* **331**, 56 (1988).
- [13]. P. R. Okamoto, L. E. Rehn, J. Pearson, R. Bhadra, and M. Grimsditch, *J. Less-Common Met.* **140**, 231 (1988).
- [14]. D. Wolf, P. R. Okamoto, S. Yip, J. F. Lutsko, and M. Kluge, *J. Mater. Res.* **5**, 286 (1990).
- [15]. Z. H. Jin, P. Gumbsch, K. Lu, E. Ma, *Phys. Rev. Lett.* **87**, 055703 (2001).
- [16]. Q. S. Mei, K. Lu, *Prog. Mater. Sci.* **52**, 1175 (2007).
- [17]. T. Egami, Y. Waseda, *J. Non-Cryst. Solids* **64**, 113 (1984).
- [18]. P. R. Okamoto, N. Q. Lam, L. E. Rehn, *Solid State Phys.* **52**, 1 (1999).
- [19]. K. Binder, W. Kob, *Glassy Materials and Disordered solids* (World Scientific, 2005).
- [20]. A. I. Larkin, S. A. Pikin, *Zh. Eksp. Teor. Fiz.* **56**, 1664 (1969) [*Sov. Phys.-JETP* **29**, 891 (1969)]; A. Aharony, *Phys. Rev. B* **8**, 4324 (1973); Y. Imry, *Phys. Rev. Lett.* **33**, 1304 (1974); D. R. Nelson, B. I. Halperin, *Phys. Rev. B* **19**, 2457 (1979).
- [21]. K. Binder, A. P. Young, *Rev. Mod. Phys.* **58**, 801 (1986).
- [22]. C. W. Garland, J. O. Fossum, A. Wells, *Phys. Rev. B* **38**, 5640 (1988); K. Knorr, *Phys. Rev. Lett.* **66**, 3016 (1991).
- [23]. M. Li, W. L. Johnson, *Phys. Rev. Lett.* **70**, 1120 (1993); M. Li, W. L. Johnson, and W. A. Goddard, *Mater. Sci. For.* **179-181**, 855 (1995); M. Li, *Phys. Rev. B* **62**, 13979 (2000); G. P. Zheng, M. Li, *Acta Mater.* **53**, 3893 (2006);
- [24]. P. G. Debenedetti, *Metastable Liquids* (Princeton University press, Princeton, New Jersey, 1996).

- [25]. J.-C. Tolédano, P. Tolédano, *The Landau Theory of Phase Transitions*, (World Scientific, 1987); R. A. Cowley, *Adv. Phys.* **29**, 1 (1980); H. Löwen, R. Lipowsky, *Phys. Rev. B* **43**, 3507 (1991); *Phys. Rev. Lett.* **49**, 1575 (1982).
- [26]. W. Schweika, In *Statics and Dynamics of Alloy Phase Transformations*, Eds. P. E. Turchi, A. Gonis, (Plenum Press, New York, 1994).
- [27]. D. Kivelson, H. Reiss, *J. Phys. Chem. B* **103**, 8337 (1999).
- [28]. N. Q. Lam, P. R. Okamoto, and M. Li, *J. Nucl. Mater.* **251**, 89 (1997).
- [29]. M. A. Krivoglaz, *X-ray and neutron Diffraction in Nonideal Crystals* (Springer, Berlin, 1996).
- [30]. R. Bormann, *Mater. Sci. Eng. A* **179/180**, 31 (1994).
- [31]. C. Michaelsen, W. Sinkler, Th. Pfullmann, and R. Bormann, *J. Appl. Phys.* **80**, 2156 (1996).
- [32]. H. J. Fecht, *Nature*, **356**, 133 (1992).
- [33]. A. L. Greer, *J. Less-Common Met.* **140**, 327 (1988).
- [34]. V. L. Gurevich, D. A. Parshin, H. R. Schober, *Phys. Rev. B* **67**, 094203 (2003).
- [35]. W. Schirmacher, G. Diezemann, C. Ganter, *Phys. Rev. Lett.* **81**, 136 (1998).
- [36]. N. P. Kulish, P. V. Petrenko, *Phys. Status Solidi A* **120**, 325 (1990).
- [37]. T. Fukunaga, N. Hayashi, K. Kai, N. Watanabe, and K. Suzuki, *Physica B* **120**, 352 (1983).
- [38]. M. Goda, *J. Phys. C: Solid State Phys.* **6**, 3047 (1973).
- [39]. J. M. López, J. A. Alonso, and L. J. Gallego, *Phys. Rev. B* **36**, 3716 (1987).
- [40]. Y. Waseda, et. al. *Sci. Technol. Adv. Mater.* **9**, 023003 (2008).
- [41]. M. A. Krivoglaz, *X-ray and neutron Diffraction in Nonideal Crystals* (Springer, Berlin, 1996).
- [42]. A. G. Khachaturyan, *Theory of Structural Transformations in Solids* (Wiley, New York, 1983).
- [43]. Luca Leuzzi, Th. M. Nieuwehuizen, *Thermodynamics of the Glassy State* (Taylor & Francis, 2007).
- [44]. V. L. Berezinskii, *Sov. Phys.-JETP* **32**, 493 (1970).
- [45]. J. M. Kosterlitz, D. J. Thouless, *J. Phys. C: Solid State Phys.* **5**, L124 (1972).
- [46]. B. I. Halperin D. R. Nelson, *Phys. Rev. Lett.* **41**, 121 (1978).
- [47]. A. P. Young, *Phys. Rev. B* **19**, 1855 (1979).
- [48]. Y. Q. Wang, X. F. Duan, L. M. Cao, W. K. Wang, *Chem. Phys. Lett.* **359**, 273 (2002).
- [49]. Y. Q. Wang, X. F. Duan, *Chem. Phys. Lett.* **367**, 495 (2003).
- [50]. H. Li, C. G. Wang, Q. F. Zhao, H. X. Li, *Appl. Surf. Sci.* **254**, 7516 (2008).
- [51]. B. Fultz, J. M. Howe, *Transmission Electron Microscopy and Diffractometry of Materials*, (Berlin: Springer, 2008), P491.
- [52]. N. E. Cusack, *Rep. Prog. Phys.* **26**, 361 (1963).
- [53]. R. Landauer, J. C. Helland, *J. Chem. Phys.* **22**, 1655 (1954).
- [54]. P. Dean, *Proc. Phys. Soc.* **84**, 727 (1964).
- [55]. B. Y. Tong, *Phys. Rev. A* **1**, 52 (1970).
- [56]. B. Y. Tong, *J. Non-Cryst. Solids* **4**, 455 (1970).
- [57]. R. J. Bell, *J. Phys. C: Solid State Phys.* **5**, L315 (1972).
- [58]. R. J. Elliott, J. A. Krumhansl, P. L. Leath, *Rev. Mod. Phys.* **46**, 465 (1974).
- [59]. V. A. Singh, L. M. Roth, *Phys. Rev. B* **15**, 3694 (1977).

- [60]. R. Rey-Gonzalez, P. A. Schulz, *Phys. Rev. B* **54**, 7103 (1996).
- [61]. P. Bak, *Rep. Prog. Phys.* **45**, 587 (1982).
- [62]. P. Reichert, R. Schilling, *Phys. Rev. B* **30**, 917 (1984).
- [63]. P. Reichert, R. Schilling, *Phys. Rev. B* **32**, 5731 (1985).
- [64]. S. Martin, W. Martienssen, *Z. Phys. B* **68**, 299 (1987).
- [65]. S. H. Strogatz, *Nonlinear Dynamics and Chaos*, (Addison-Wesley Pub., 2000).
- [66]. L. van Hove, *Physica* **16**, 137 (1950).
- [67]. L. D. Landau, E. M. Lifshitz, *Statistical Physics*, Part1, (Pergamon, New York, 1980).
- [68]. E. H. Lieb, D. C. Mattis, *Mathematical Physics in One-dimension*, (Academi Press, New York, 1966), Chapter 1.
- [69]. M. Kac, G. Uhlenbeck, P. Hemmer, *J. Math. Phys.* **4**, 216 (1964).
- [70]. F. J. Dyson, *Commun. Math. Phys.* **12**, 212 (1969); **21**, 269 (1971); P. W. Anderson, G. Yuval, *J. Phys. C: Solid St. Phys.* **4**, 607 (1971); J. Bhattacharjee, S. Chakravarty, J. L. Richardson, D. J. Scalapino, *Phys. Rev. B* **24**, 3862 (1981).
- [71]. N. Saito, M. Oonuki, *J. Phys. Soc. Jpn.* **29**, 69 (1970).
- [72]. M. E. Fisher, G. W. Milton, *Physica A* **138**, 22 (1986).
- [73]. V. F. Morozov, A. V. Badasyan, E. Sh. Mamasakhlov, A. V. Grigoryan, *Phys. At. Nucl.* **68**, 1922 (2005).
- [74]. S. Ares, A. Sánchez, A. R Bishop, *Europhys. Lett.* **66**, 552 (2004).
- [75]. S. Ares, A. Sánchez, *Eur. Phys. J. B* **56**, 253 (2007).
- [76]. M. E. Fisher, B. Widom, *J. Chem. Phys.* **50**, 3756 (1969).
- [77]. M. E. Fisher, G. Milton, *Physica A* **138**, 22 (1986).
- [78]. P. A. Monson, *Mol. Phys.* **70**, 401 (1990).
- [79]. C. Grodon, M. Dijkstra, R. Evans, R. Roth, *Mol. Phys.* **103**, 3009 (2005).
- [80]. L. Hui, B. L. Wang, J. L. Wang, G. H. Wang, *J. Chem. Phys.* **121**, 8990 (2004).
- [81]. J. L. Wang, X. S. Chen, G. G. Wang, B. L. Wang, W. Lu, J. J. Zhao, *Phys. Rev. B* **66**, 085408 (2002).
- [82]. G. Bilalbegović, *Vacuum* **71**, 165 (2003).
- [83]. B. L. Wang, G. G. Wang, X. S. Chen, J. J. Zhao, *Phys. Rev. B* **67**, 193403 (2003).
- [84]. L. Miao, V. R. Bhethanabotla, B. Joseph, *Phys. Rev. B* **72**, 134109 (2005).
- [85]. S. K. R. S. Sankaranarayanan, V. R. bhethanabotla, B. Joseph, *J. Phys. Chem. C* **111**, 2430 (2007).
- [86]. G. Abudukelimu, G. Guisbiers, M. Wautelet, *J. Mater. Res.* **21**, 2829 (2006).
- [87]. A. Ibenskas, Ch. E. Iekka, G. A. Evangwlakis, *Physica E* **37**, 189 (2007).
- [88]. Z. M. Ao, W. t. Zheng, Q. Jiang, *Nanotechnology* **18**, 255706 (2007).
- [89]. H. Ikeda, Y. Qi, T. Cagin, K. Samwer, W. L. Johnson, W. A. Goddard III, *Phys. Rev. Lett.* **82**, 2900 (1999).
- [90]. P. S. Branício, José-Pedro Rino, *Phys. Rev. B* **62**, 16950 (2000).
- [91]. G. L. Wilson, G. M. Bell, *J. Phys. A: Math. Gen.* **10**, L43 (1977).
- [92]. A. Fuliński, *Acta Phys. Pol. A* **53**, 869 (1978).
- [93]. M. Uwaha, P. Nozières, *J. Physique* **46**, 109 (1985).
- [94]. K. Ikeda, *J. Phys. Soc. Jpn.* **54**, 3277 (1985).
- [95]. K. Ikeda, *J. Phys. Soc. Jpn.* **57**, 2293 (1988).
- [96]. A. P. Vieira, I. L. Goncalves, *Condens. Matter. Phys.* **5**, 210 (1995).
- [97]. A. P. Vieira, I. L. Goncalves, *J. Chem. Phys.* **110**, 1235 (1999).

- [98]. D. C. Hong, *Phys. Rev. E* **63**, 051506 (2001).
- [99]. J. W. Gibbs, *The Scientific Papers, Vol 1: Thermodynamics*, (Dover Publications, New York, 1961).
- [100]. M. Volmer, A. Weber, *Z. Phys. Chem.* **119**, 277 (1926).
- [101]. H. E. Cook, *Acta Metall.* **23**, 1027 (1975).
- [102]. I. M. Lifshitz, *J. Phys. U.S.S.R.* **7**, 215 (1943); **7**, 249 (1943); **8**, 89 (1944).
- [103]. G. Schaefer, *J. Phys. Chem. Solids* **12**, 233 (1960).
- [104]. A. A. Maradudin, E.W. Montroll, G.H. Weiss, and I.P. Ipatova, *Theory of Lattice Dynamics in the Harmonic Approximation* (Academic, New York, 1971).
- [105]. P. H. Dederichs, R. Zeller, *Point Defects in Metals II*, Springer Tracts in Modern Physics, Vol. 87 (Berlin: Springer, 1980).
- [106]. P. H. Dederichs, C. Lehmann, and A. Scholz, *Phys. Rev. Lett.* **21**, 1130 (1973).
- [107]. R. Urban, P. Ehrart, W. Schilling, H.R. Schober, and H. Iauter, *Phys. Status Solidi(B)* **144**, 287 (1987).
- [108]. A. J. Sievers, S. Takeno, *Phys. Rev. Lett.* **61**, 970 (1988).
- [109]. S. Takeno, K. Kisoda, A.J. Sievers, *Prog. Theor. Phys. Suppl.* **94**, 242 (1988).
- [110]. S. Takeno, K. Hori, *J. Phys. Soc. Jpn.* **59**, 3037 (1990).
- [111]. S. Takeno, *J. Phys. Soc. Jpn.* **61**, 2821 (1992).
- [112]. S. Takeno, A. J. Sievers, *Solid State Commun.* **67**, 1023 (1988).
- [113]. Yu. S. Kivshar, *Phys. Lett. A* **161**, 80 (1991).
- [114]. W. Ebeling, M. Jessen, *Physica D* **32**, 183 (1988).
- [115]. K. Forinash, M. Peyrard, B. Malomed, *Phys. Rev. E* **49**, 3400 (1994).
- [116]. F. Abdullaev, A. R. Bishop, S. Pnevmatikos, *Nonlinearity with disorder*, proceeding of the Tashkent Conference, Tashkent, Uzbekistan, october 1990, (Springer-Verlag, Berlin, 1992).
- [117]. Yu. A. Kosevich, S. Lepri, *Phys. Rev. B* **61**, 299 (2000).
- [118]. A. L. Shumway, J. P. Sethna, *Phys. Rev. Lett.* **67**, 995 (2001).
- [119]. V. G. Karpov, M. I. Klinger, and F. N. Ignatiev, *Sov. Phys. JETP* **57**, 439 (1983).
- [120]. B. Rufflé, D. A. Parshin, E. Courtens, R. Vacher, *Phys. Rev. Lett.* **100**, 015501 (2008).
- [121]. W. Ebeling, V. Yu. Podlipchuk, M. G. Sapeshtinsky, *Int. J. Bifurcation and Chaos* **10**, 1075 (2000).
- [122]. T. Dauxois, M. Peyrard, A. R. Bishop, *Phys. Rev. E* **47**, 648 (1993).
- [123]. S. Takeno, T. Suzuki, in *Nonlinear Waves: Classical and Quantum Aspects*, Eds. F. Kh. Abdullaev, V. V. Konotop, (Kluwer Academic Publishers, 2004).
- [124]. M. Peyrard, *Acta Phys. Polo. B* **25**, 955 (1994).
- [125]. M. Peyrard, in *Nonlinearity with disorder*, proceeding of the Tashkent Conference, Tashkent, Uzbekistan, October 1990, Eds. F. Abdullaev, A. R. Bishop, S. Pnevmatikos, (Springer-Verlag, Berlin, 1992).
- [126]. M. Peyrard, S. C. López, D. Angelov, *Eur. Phys. J. Special Topics* **147**, 173 (2007).
- [127]. M. Peyrard, *Nonlinearity* **17**, R1 (2004).
- [128]. W. Ebeling, V. Y. Podlipchuk, A. A. Valuev, *Physica A* **217**, 22 (1995).
- [129]. M. Jenssen, W. Ebeling, *Physica D* **141**, 117 (2000).
- [130]. S. Y. Huang, X. W. Zou, Z. J. Tan, Z. Z. Jin, *Physica A* **296**, 426 (2001).
- [131]. V. I. Yukalov, *Phys. Rev. B* **64**, 113 (1984).

- [132]. K. J. Strandburg, *Rev. Mod. Phys.* **60**, 161 (1988).
- [133]. W. Ebeling, M. Jessen, *Physica D* **32**, 183 (1988).
- [134]. D. R. Nelson, in *Phase transitions and critical phenomena*, Eds. C. Domb and J. L. Lebowitz, (Academic press, New York, 1983).####
- [135]. F. F. Abraham, *Homogeneous Nucleation Theory*, (Academic Press, New York and London, 1974).
- [136]. L. D. Landau and I. M. Khalatnikov, *Doklady Akademii Nauk SSSR*. **96**, 469 (1954).
- [137]. J. W. Cahn, J. E. Hilliard, *J. Chem. Phys.* **31**, 688 (1959).
- [138]. J. W. Cahn, *Acta Metall.* **8**, 554 (1960).
- [139]. K. Lu, Y. Li, *Phys. Rev. Lett.* **80**, 4474 (1998).
- [140]. M. Iwamatsu, K. Horii, *J. Phys. Soc. Japan* **65**, 2311 (1996); Iwamatsu M. *J. Phys.: Condens. Matter* **11**, L1 (1999).
- [141]. A. N. Kolmogorov, *Izv. Akad. Nauk SSSR, Ser. Mat.* **3**, 355 (1937).
- [142]. W. A. Johnson, R. F. Mehl, *Trans. AIME* **135**, 416 (1939).
- [143]. M. Avrami, *J. Chem. Phys.* **7**, 1103 (1939).
- [144]. M. Avrami, *J. Chem. Phys.* **8**, 212 (1940).
- [145]. M. Avrami, *J. Chem. Phys.* **9**, 177 (1941).
- [146]. S. K. Chan, *J. Chem. Phys.* **67**, 5755 (1977).
- [147]. J. Frenkel, *J. Phys.* **1**, 315 (1939).
- [148]. D. E. Luzzi, H. Mori, H. Fujita, M. Meshii, *Acta Metall.* **34**, 629 (1986).
- [149]. J. M. Ziman, *Models of Disorder: The Theoretical Physics of Homogeneously Disordered Systems*, (Cambridge Univ. Press, Cambridge and New York, 1979).
- [150]. Y. Imry, D. J. Scalapino, *Phys. Rev. A* **9**, 1672 (1974).
- [151]. R. Bartussek, Ch. Zülicke, L. Schimansky-Geier, *Chaos Soli. Fract.* **5**, 1927 (1995).
- [152]. V. I. Yukalov, *Phys. Rep.* **208**, 1991 (395).
- [153]. V. I. Yukalov, *Phys. Lett. A* **81**, 433 (1981).
- [154]. V. I. Yukalov, *Chem. Phys. Lett.* **229**, 239 (1994).
- [155]. V. I. Yukalov, *Int. J. Mod. Phys. B* **17**, 2333 (2003).
- [156]. H. E. Cook, *Phys. Rev. B* **15**, 1477 (1977).
- [157]. L. Bakaleynikov, J. Felsteiner, A. Gordon, *Physica B* **369**, 104 (2005).
- [158]. Yu. E. Kuzovlev, T. K. Soboleva, A. E. Philippov, *J. Exp. Theor. Phys.* **76**, 858 (1993).
- [159]. A. Safaei, M. A. Shandiz, S. Sanjabi, Z. H. Barber, *J. Phys.: Condens. Matter* **19**, 216216 (2007).
- [160]. B. S. Murty, M. K. Datta, S. K. Pabi, *Sadhana* **28**, 23 (2003).
- [161]. Q. S. Mei, K. Lu, *Prog. Mater. Sci.* **52**, 1175 (2007).
- [162]. M. P. Henaff, C. Colinet, A. Pasturel, K. H. Bushow, *J. Appl. Phys.* **56**, 307 (1984).
- [163]. J. Weissmüller, W. Krauss, T. Haubold, R. Birringer, H. Gleiter, *Nanostructured Mater.* **1**, 439 (1992).
- [164]. H. J. Fecht, *Nanostructured Mater.* **6**, 33 (1995).
- [165]. U. Herr, M. Geigl, K. Samwer, *Phil. Mag. A* **77**, 641 (1998).
- [166]. Y. H. Zhao, Z. H. Jin, K. Lu, *Phil. Mag. Lett.* **79**, 747 (1999).
- [167]. J. W. Cahn, *J. Phys. Colloq.* **43-C6**, 199 (1982).

- [168]. P. J. Desre, *Nanostructured Mater.* **4**, 957 (1994).
- [169]. J. F. Scott, M. S. Zheng, R. Bruce Godfrey, C. Araujo, L. Mcmillan, *Phys. Rev. B* **35**, 4044 (1987); K. Ishikawa, K. Yoshikawa, N. Okada, *Phys. Rev. B* **37**, 5852 (1988).
- [170]. H. Saka, Y. Nishikawa, T. Imura, *Philos. Mag. A* **57**, 895 (1988).
- [171]. V. P. Skripov, V. P. Koverda, V. N. Skokov, *Phys. Status Solidi A* **66**, 109 (1981).
- [172]. J. F. Pócza, A. Barna, P. B. Barna, *J. Vac. Sci. Technol.* **6**, 472 (1969).
- [173]. K. F. Peters, J. B. Cohen, Y. W. Chung, *Phys. Rev. B* **57**, 13430 (1998).
- [174]. P. Pavlow, *Z. Phys. Chem.* **65**, 1 (1909).
- [175]. M. Takagi, *J. Phys. Soc. Jpn.* **9**, 359 (1954).
- [176]. F. G. Shi, *J. Mater. Res.* **9**, 1307 (1994).
- [177]. R. Lipowsky, W. Speth, *Phys. Rev. B* **28**, 3983 (1983).
- [178]. B. Plauis, D. Frenkel, J. F. Van der. Veen, *Surf. Sci.* **239**, 282 (1990).
- [179]. H. Sakai, *Surf. Sci.* **348**, 387 (1996).
- [180]. A. P. Chernyshev, *Mater. Chem. Phys.* **112**, 226 (1008).
- [181]. A. Zangwill, *Physics at surfaces*, (Cambridge University Press, New York, 1988.)
- [182]. P. J. Desre, *Nanostructured Mater.* **8**, 687 (1997).
- [183]. M. Tang, W. C. Carter, R. M. Cannon, *J. Mater. Sci.* **41**, 7691 (2006); *Phys. Rev. Lett.* **97**, 075502 (2006).
- [184]. K. F. Peters, J. B. Cohen, Y. W. Chung, *Phys. Rev. B* **57**, 13430 (1998).
- [185]. W. A. Jesser, R. Z. Shneck, W. W. Gile, *Phys. Rev. B* **69**, 144121 (2004).
- [186]. H. Yashuda, K. Mitsuishi, H. Mori, *Phys. Rev. B* **64**, 094101 (2001).
- [187]. T. L. Hill, *Thermodynamics of Small Systems*, vols. I, II, (Benjamin, New York 1963).
- [188]. T. L. Hill, *Nano Lett.* **1**, 159; **1**, 273 (2001).
- [189]. J. Dunkel, S. Hilbert, *Physica A*, **370**, 390 (2006).
- [190]. R. S. Berry, *Microscale Thermophys. Eng.* **1**, 1 (1997).
- [191]. R. S. Berry, *J. Phys. B: At. Mol. Opt. Phys.* **39**, R167 (2006).
- [192]. S. K. R. S. Sankaranarayanan, V. R. Bhethanabotla, B. Joseph, *J. Phys. Chem. C* **111**, 2430 (2007).
- [193]. N. Quirke, P. Sheng, *Chem. Phys. Lett.* **110**, 63 (1984); R. D. Etters, J. B. Kaelberer, *J. Chem. Phys.* **66**, 5112 (1977); J. B. Kaelberer, R. D. Etters, *J. Chem. Phys.* **66**, 3233 (1977).
- [194]. Y. Imry, S. K. Ma, *Phys. Rev. Lett.* **35**, 1399 (1975).
- [195]. A. Shi, A. J. Berlinsky, *Phys. Rev. B* **47**, 652 (1993).
- [196]. Pierre Tol e' dano, Vladimir Dmitriev, *Reconstructive phase transition*, (World Scientific, 1996).